Politecnico di Torino

Doctorate School

Ph.D. in Materials Science And Technology

Doctoral Thesis

Study of an innovative joining solution for the wheel system

Author:
Giorgio Gallio

Supervisors:
Prof.ssa Laura Montanaro
Prof. Paolo Fino

December 2013

find a job you love and
you will never have to work
a day in your life

Abstract

The objective of this thesis research is to develop an adhesive bonding solution in order to remove the classic welding technology exploited nowadays in the automotive steel wheel system.

The examined solution is an hybrid joint, based on adhesive boding combined with the presence of an interference fit. This hybrid joining technology consists in coupling two cylindrical components together by force-fitting one into the other after having placed an adhesive on the mating surfaces. This technique would allow the joining of dissimilar material to enable the design of hybrid lightweight wheels. Moreover, it would provide a better stress distribution in the joint area that could induce fatigue life improvement.

The contributions of the adhesive and the interference on the performance of the final hybrid joint is still not completely clear. In particular, the effect of the adhesive nature and of its mechanical and adhesive responses on the performance of the hybrid joint is under concern in this research. A study of the phenomena acting at the interference level is conducted at the laboratory level before industrial case application. An experimental method is set up in order to test the adhesives in a press fit joint. Static and dynamic tests are carried out examining the behavior of different adhesives, including rigid epoxies and flexible polyurethanes, and fractographic analysis are then performed.

The second part of the study is focused on the feasibility of the hybrid technology on the wheel system. Exploiting the outcomes of the laboratory analysis, bonded wheel prototypes are assembled and tested statically and dynamically, according to component validation in MW.

From the laboratory scale analyses it is found that the adhesive type mainly affects the static resistance of the hybrid joint. In particular the curing technology affects the decoupling behavior and the rheology influences the quantity of adhesive that remains inside the joint despite the interference levels. On the other hand, the interference rules the stiffness of the assembly and strongly

vi

affects the fatigue behavior of the cylindrical joint. The study conducted on the wheel component confirms the laboratory scale outcomes. For what concern the feasibility study, the bonded wheel shows similar performances compared to the welded wheel without design modifications of the components. However, the joint geometry has to be redesigned to exploit all the advantages of the adhesive bonding.

Acknowledgments

I would like to thank my supervisors: prof. Laura Montanaro for giving me the opportunity to take up this PhD path and for the discussions that helped strengthen both my research and my work attitude; prof. Paolo Fino for the useful ideas and the confidence he inspired in me; Mariangela for all the daily discussions, debates, agreements and understandings. The folks of the Alessandria lab, who with open minds have helped me to become familiar with the instruments that have accompanied my work.

I would like to thank the MW Company which made this PhD journey possible. In particular, my supervisor Davide Rovarino for understanding the research work and adjusting it to the company needs; Fabrizio for his patience; Luca for the help and support beneath the kidding around; Silvio for not being annoyed by my nitpicking measuring approach.

Many thanks are due to all my collegues who have crossed my path and whit whom I've shared the lab-life of poor phd students and assistant researchers for three long years or just for few months. We had good and bad times together, mostly spent complaining a lot, but also sharing good ideas and supporting each other in every workday activity: from partacking the expectation of attempting a new solution to comforting each other when, as usual, it didn't work; from sharing ideas for improving the research to revealing the receipe for improving the packed lunch; from joking around to the deep talks during the long afternoons working in the lab.

Last but not least I'm grateful to those people who, with love, helped me get through the thesis writing process.

Contents

List of Figures

xiv

List of Tables

Introduction

Research background

The thesis research was carried out at the Department of Applied Science and Technology (DISAT) of the Politecnico di Torino in the framework of the partnership with the company MW Italia SpA. MW Italia SpA is a division of the CLN group, that is one of the leading international players on the world market of processing, stamping and assembly of metal components. The business of MW division concerns the steel wheel market for passenger cars, light and heavy commercial vehicles and motorcycles.

Nowadays steel wheels begin to regain market share against the aluminum alloy wheels [1,2]. After the big break through of the aluminum alloy wheel, the two metals now own about 50% of the market share [1,3]. New high-strength steels, such as dual-phase steel, allow the reduction of the wheel weight and the implementation of large ventilation openings. In this way, it should be possible to exploit new designs for the steel wheel in an attempt to approach the thin-spoke appearance of some aluminum alloy wheels [1,3]. In a field dominated by the constant request of weight and consumption reduction, the automakers opt for steel wheels to trim the weight of their products as they are lighter and much more cost effective than their aluminum equivalent [1–3]. The exploitation of new materials and new metal alloys is a key solution for obtaining lightweight structures and more innovative and attractive products [3].

The current steel wheel is composed of two components, the disc and the rim, joined together by force fitting one into the other and then welding, as schematized in figure 1. A general technical drawing of a steel wheel with the relative terminology of the wheel's parts is reported in Appendix A. Welding is a classic method to join steel components together, but often it is not possible to weld two different metals or joining metals to ceramic, composite or polymeric

materials. In order to employ new types of materials for the wheel components a revision of the joining technology is then necessary.

Interference fit + 4 CO_2 welding

Steel Disc   Steel Rim

Figure 1: Schematic representation of the present joining technology of the wheel system.

Adhesive bonding is a suitable technology to join dissimilar materials together and recently its usage has greatly increased in industry for bonding new hybrid lightweight structures [4–6]. In this technology two substrates, namely *adherends*, are held together by an adhesive generating an adhesive joint. Adhesives may provide an advantageous alternative to the classic welding procedure. Adhesives provide a weight-saving joint solution and often they can guarantee an uniform stress distribution in the joint area, that can be reflected in an improvement of the fatigue life of the components [4–8].

The main drawback about adhesive bonded joints is related to their durability, especially in outdoor environments as they are susceptible to water and humidity [6–8]. In order to overcome this problem, adhesives are often employed in combination with other traditional joining methods, such as mechanical fastening techniques (e.g. rivets or bolts) or welding techniques, generating a hybrid joint [9]. Hybrid adhesive joints are designed with the aim of combining the advantages of the different techniques, trying to overcome their drawbacks [9].

The presence of the interference fit in the wheel system is necessary for structural purposes and it seems to have a relevant role in governing the stress distribution and the fatigue life of the wheel [3]. The introduction of an adhesive in the present interference fit system can lead to an adhesive bonded-interference fitted hybrid joint.

The hybrid adhesive/interference-fit joint is realized by force-fitting two cylindrical components, after having placed an adhesive on the mating surfaces. This hybrid joint method, generally realized by exploiting acrylic anaerobic systems [10–12], has been studied by several authors [10, 12–20]. It is widely accepted that introducing an adhesive into an interference fit can lead to a

considerably strength enhancement. Moreover the adhesives fill the roughness of the mating surfaces bringing the real contact area between the two fitted components to 100%, thus improving the stress distribution in the joint area. Notwithstanding this, some aspects of this hybrid joint had to be clarified before its application in the wheel system.

Research questions

The anaerobic acrylics are the adhesives more extensively employed in joining interference fitted cylindrical components. This choice is probably due to their particular curing technology, in which the hardening of the adhesive on metal substrate occurs in absence of oxygen, as it happens in a tightly closed joint. In more complex joint geometries like in the wheel system, the anaerobic acrylics could be not the proper choice, considering that their hardening is blocked by oxygen in clearance conditions. The effect of the adhesive nature, its curing technology and its mechanical and adhesive responses on the performances of the hybrid joint is still unclear.

- *What is the effect of different adhesive types in terms of nature, curing technology and mechanical properties in presence of the interference fit? What will be the proper adhesive choice for the application in the interference fitted wheel system?*

Different theories have been developed to understand the interaction between the resistance contribution guaranteed by the interference-fit and that provided by the adhesive in a hybrid joint. A detailed description of the hybrid joint and a literature review of its state of the art are presented in Chapter 2. As many parameters could influence the performance of this hybrid joint, the developed methods could not be exhaustive in explaining all the possible interactions. For instance, in press-fitted samples the coupling pressure, the spewing of the adhesive outside the joint and the friction phenomena could affect the final joint systems, involving parameters related to rheology and tribology. Further studies of the phenomena acting at the interference level will be useful for the design of particular components that involve this hybrid joint technique.

- *Once selected the adhesive, what will be its static and dynamic mechanical response in presence of different interference levels?*

Bonded wheel prototypes should be created in order to evaluate the feasibility of the hybrid interference fitted/adhesive bonded technique in the joining

of the automotive wheels. Quality control and validation tests must be carried out to evaluate the structural safety of the bonded wheels and to define which parameters are critical for this joining solution. The performances of the new bonding solution will be compared to the ones of the welded wheels employed in the normal production.

- *Is the hybrid solution applicable to the wheel system? Which are the key parameters that govern the resistance of this joining method in the wheel application? In a steel/steel configuration, how the bonded wheel would perform in comparison with the welded one ?*

Thesys structure

- Chapter 1 Theories and mechanisms of adhesive bonding

  Basic theoretical concepts of adhesion are proposed going from the microscopic aspects related to how adhesion is created to the macroscopic ones that influence the resistance of a bonded joint.

- Chapter 2 The hybrid bonded-interference fitted joint

  The hybrid adhesive/interference-fit joining technique is deeply described and a literature review of its state of the art is reported.

- Chapter 3 Methodology

  A brief description of the testing methods available in general for adhesive joints and in particular for the hybrid joints is presented. The chosen methodology for testing the hybrid joints is then described with some considerations on its set-up.

- Chapter 4 The behavior of different adhesives in the hybrid joint

  The work presented in this chapter was related to the behaviour of different adhesives, including rigid epoxies and flexible polyurethanes, in the presence of an interference-fit.

- Chapter 5 Interference contribution on the performance of the hybrid joint

  The work presented in this chapter aimed to study the role played by the tensile field produced by the interference in the hybrid joints and the influence of the friction effects acting during press-fit.

- Chapter 6 Application of the hybrid joint to the automotive wheel

  The chapter describes the technology transfer from the laboratory scale to the wheel system. Bonded wheel prototypes were submitted to standard tests adopted for components validation in MW. The obtained results were compared to the trend observed at laboratory level.

- Chapter 6.3 Conclusions

  The main outcomes of the work are summarized

Limitations

- The study evaluated the feasibility of the hybrid adhesive/interference fit joining technology in the wheel system from a structural point of view. Static and dynamic mechanical behavior of the adhesive in the interference fit was studied. The aging of the adhesive under combined environmental condition was not taken into consideration.

- Only one typical type of adhesive for each main structural adhesive families was taken into consideration for the application on the wheel system. This general approach was intended to study adhesives with strong different properties in order to select the best adhesive typology. A more refined adhesive selection should be conducted in a more advanced stage of the bonded wheel project.

- Only three interference levels were examined in pull-out tests. Moreover fatigue tests compared the behavior of the chosen adhesive in an interference condition to its behavior in clearance condition. The behavior of the adhesive at higher interference conditions was not studied. At higher interference levels it was difficult to obtain repeatable joints as the samples were characterized by more frequent assembly problems related to the misalignments of the components.

Chapter 1

Theories and mechanisms of adhesive bonding

Abstract

An adhesive bonded joint is a complex system as it involves different materials (adhesive and substrates) and interfaces. Chemistry, surface physics and mechanical engineering are the subjects involved in the study of this system. In this chapter some basic theoretical concepts are first proposed to understand the general factors influencing the resistance of a bonded joint. Then the adhesion theories are discussed, taking into account those phenomena that can influence the adhesion. Besides the adhesion, also the cohesion of the adhesive material and the substrates are involved in the joint system. Those aspects and their relationship are discussed according to a fracture mechanics approach applied to adhesive joints. Going from the microscopic aspects to the macroscopic ones, the influence of the joint geometry and the type of applied load is investigated. The mechanisms of degradation (mechanical and environmental) of an adhesive joint during its service life are analyzed in the last part of the chapter.

7

1.1 Basic theoretical concept of adhesive bonding

1.1.1 Adhesion and cohesion

The most important parameter in adhesion is the surface free energy (or surface tension) γ [8]. This parameter is defined as the reversible work required to create a unit surface area, as shown in equation 1.1.

$$\gamma = \left(\frac{\delta W}{\delta A} \right) \tag{1.1}$$

where δW is the infinitesimal work required to increase the surface by an infinitesimal area δA.

The surface tension is a direct measurement of the intermolecular forces acting in a material. Indeed the reversible work, necessary to break a material acting against the intermolecular forces that provide its cohesion, is a function of the surface free energy. In an ideal system in vacuum, splitting a material creating two identical surfaces, requires a work. This work is called the work of cohesion (W_c) and it is defined by equation 1.2 where γ_1 is the surface tension of a material [21].

$$W_c = 2\gamma_1 \tag{1.2}$$

$$W_a = \gamma_1 + \gamma_2 - \gamma_{12} \tag{1.3}$$

Based on the work of cohesion, Duprè defined the work of adhesion, as the reversible work required to detach two different materials in contact. The system is schematized in figure 1.1 and the work of adhesion (W_a) is defined by the Duprè equation (eqn. 1.3) where γ_1 and γ_2 are the surface free energies of the material 1 and 2, respectively, and γ_{12} is the interfacial tension at the interface between the two materials.

1.1.2 The strength of an adhesive joint

To better understand the factors that influence the final resistance of an adhesive joint it is necessary to apply the concepts of adhesion and cohesion. Indeed the failure of an adhesive joint depends on both the adhesive and cohesive forces proper of the materials involved. A generic adhesive joint could fail adhesively
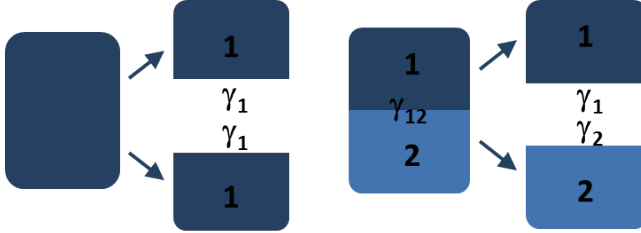
Figure 1.1: Schematic representation of the work of cohesion and the work of adhesion.

or cohesively or by some combination of these two mechanisms. The general typologies of failure are illustrated in figure 1.2 [8, 22].

Cohesion is determined by the inner strength of a material, and the cohesive failure could exist within either the adhesive material or the adherent itself. Adhesive failure is an interfacial bond failure between the adherent and the adhesive, so it mainly depends on the work of adhesion.

Kinloch [8] proposed a useful geometry-independent model to describe the adhesion strength of a generic joint. He defines the adhesive fracture energy (G_c) by using the equation 1.4.

$$G_c = G_0 + \Psi \tag{1.4}$$

where G_0 represents the intrinsic fracture energy, e.g. the energy required to propagate a crack through a unit area of interface in absence of energy dissipation. The term Ψ represents the contribution of the energy viscoelastically dissipated within the adhesive at the tip of the propagating crack, equally referred to the unit area. The energy dissipated viscoelastically is usually the major contribution to the measured adhesive fracture energy (G_c).

Considering the different failure modes described in figure 1.2, the intrinsic adhesive fracture energy (G_0) may be expressed as a weighted average of the various possible fracture planes as shown in eqn. 1.5.

$$G_0 = iG_{0(adhesive)} + bG_{0(cohesive-in-adhesive)} + sG_{0(cohesive-in-substrate)} \tag{1.5}$$

where $G_{0(adhesive)}$, $G_{0(cohesive-in-adhesive)}$, $G_{0(cohesive-in-substrate)}$ are the intrinsic fracture energies for the three different failure modes, and i, b and s are the respective area fractions of the different fracture surfaces: *i.e.* $i + b + s = 1$.

Failure modes of an adhesive joint:

Cohesive fracture in the adhesive material

Adhesive fracture

Cohesive fracture in the adherend
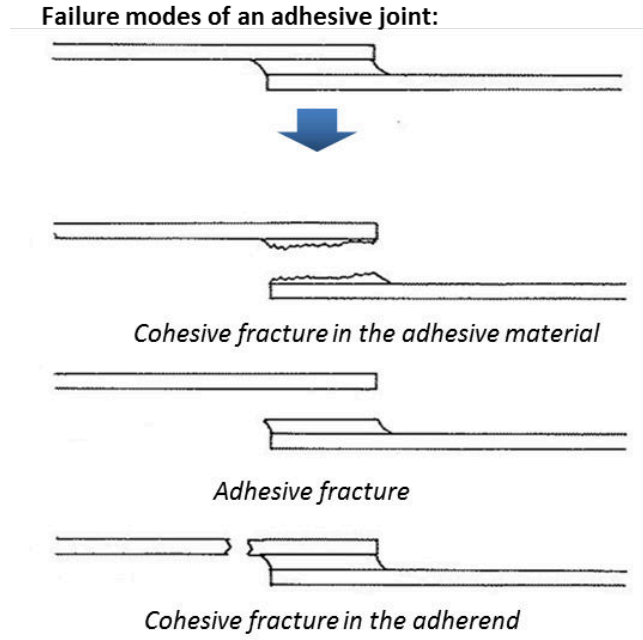
Figure 1.2: Schematic representation of the different failure modes of an adhesive joint. [22]

For those joints that exhibit a solely interfacial locus of failure, $i = 1$ and $G_0 = G_{0(adhesive)}$, therefore, the measured value of G_0 should be equal to the thermodynamic work of adhesion W_a.

In the following paragraph the forces and the phenomena the govern the work of adhesion are discussed.

1.2   Theories of adhesion

Adhesion is a complex and multi-disciplinary topic and there is not a unique theory that can simply explain the whole phenomenon. A lot of mechanisms have been proposed and analyzed by different points of view, and it is difficult to follow the evolving understanding of the subject. Many scientists [6, 7, 23, 24]

agree that certain theories have been developed to explain and rationalize only certain particular observations of the phenomenon, and therefore they represent valuable tools in that particular experimental conditions. A brief overview on what are commonly considered the main mechanisms of adhesion is reported in this paragraphs.

1.2.1 Mechanical interlocking theory

The mechanical interlocking mechanism is based essentially on the idea that an adhesive is mechanically anchored to the irregularity of the substrate surface. According with this theory, the adhesion occurs when the liquid adhesive flows and fills the pores, crevices and micro-voids of the surface. Thus, the adhesive hardens and the substrates are held together mechanically.

Surface topography of copper foil		Peel energy	
Description	Diagrammatic representation	kJ/m^2	lbf/in
Flat		0.66	3.8
Flat + 0.3 μm dendrites		0.67	3.8
Flat + 0.3 μm dendrites + oxidation		0.77	4.4
3 μm high-angle pyramids		1.0	5.9
2 μm low-angle pyramids + 0.3 μm dendrites		1.3	7.4
2 μm low-angle pyramids + 0.3 μm dendrites + oxidation		1.5	8.8
3 μm high-angle pyramids + 0.3 μm dendrites + oxidation		2.4	13.5
Nickel foil with club-headed nodular structures		2.3	13.1

Figure 1.3: Effect of surface topography on the peel strength of electroformed copper (or nickel) foils bonded with an epoxy adhesive [25].

It is widely accepted that some sort of surface roughening will increase the measured adhesion strength. Indeed the mechanical abrasion is a common surface pre-treatment for enhancing adhesion on certain surfaces. According to this theory, the mechanical interlocking provides an adhesion improvement. The experiments carried out by Arrowsmith [25] the adhesion of electroformed copper or nickel foils to epoxy laminates can be taken as an example for supporting

this theory. He altered the electroforming conditions for the copper substrates in order to give different surface topographies and he measured the adhesion strength of the different joints. The results are summarized in figure 1.3. The higher adhesion strength is supplied by surface structures like pyramids and dendrites that can give rise to effective mechanical interlocking.

The main criticism about the applicability of this mechanism concerns the fact that good adhesion can be obtained even on a smooth surface [8]. The debate on this theory focuses on the idea that the improvement in adhesion, by roughening the surface, could be simply referred to an increasing in the surface area that lead to more molecular bonding interactions [24]. In addition an increase in wettability by the adhesive due to the hysteresis of the contact angle [8] (see section 1.3.4) could contribute to the observed adhesion improvement.

1.2.2   Adsorption theory of adhesion

The adsorption theory of adhesion is certainly the most widely used approach in the adhesion science [26]. The basic principle of the adsorption theory is that the adhesion is due to intermolecular forces between the adhesive and the substrate. If an intimate molecular contact is achieved at the interface, the adhesive and the substrate will adhere because of the forces established between their molecules and atoms. These forces are commonly referred as primary and secondary forces. The secondary forces are the most common and include the long-range attractive interactions such as the Lifshitz-van der Waals dispersion and polarization forces. Kinloch [8] reported that in many different adhesive joints the adhesion involves only interfacial secondary forces. On the other side, the primary forces involve chemical bonds, such as covalent bonds, being established at the interface. This phenomena are also named chemisorption and induce higher bond strengths. Donor-acceptor interactions are also considered one of the major type of intrinsic adhesion forces that operate across the interface. This kind of forces arises by the acid-base interactions between the adhesive and the substrate where the acid and the base are a Lewis-Bronsted electron acceptor and electron donor, respectively. This classification usually includes hydrogen bonds which are considered a subset of acid-base interactions. The adsorption theory may be fully based on a thermodynamic basis and various approaches have been developed over the years to model this theory, some of them will be discussed in the section 1.3.

1.2.3 Other theories of adhesion

Other theories have been developed to explain the adhesion in particular applications or conditions. For example, the diffusion theory, developed by Voyuskii [27] and by Vasenin [28] is restrictively applicable to polymeric materials. According to this approach, the intrinsic adhesion between two polymers is due to the mutual diffusion of the polymer macromolecules across the interface. An application in which this theory plays an important role is the plastics welding [8]. Two polymers could be joined together by heating the portion to be bonded or by applying a suitable solvent, in order to enhance the chains mobility, favouring the interdiffusion mechanism. Otherwise, for instance in presence of high crosslinked polymers, interdiffusion is an unlikely mechanism of adhesion. Another theory which has a restricted application field is the Electronic theory, developed by Deryaguin [29].This approach is based on the electrostatic forces that cause the attraction between two charged materials. These electrostatic forces can act over a distance of the order of centimeters which is much greater than the range of the other mechanisms of adhesion (that require an intimate contact). More recent literature [8, 30] reports that for typical adhesive/substrate interfaces, the electrostatic force contribution to adhesion is significantly less important compared to other mechanisms of adhesion, such Wan der Waals forces. The common conclusion is that electrostatic forces play a significant role only in certain particular situations.

1.3 Thermodynamic of adhesion

The thermodynamic approach is certainly the most widely used approach to explain the adhesion phenomena according to the adsorption theory [26]. Many important phenomena that influences the adhesion process have been revealed by researchers during the investigation of the thermodynamic mechanisms. In this paragraph the main models of the adhesion are proposed in order to underline the necessary conditions to obtain a good adhesion.

1.3.1 The importance of wetting

The first step in the formation of an adhesive bond is the establishment of an interfacial molecular contact [8]. This can be expected if the adhesive (as a liquid or dispersed in a liquid medium) wets the adherent. The wetting phenomena has been described by Young in an ideal system made of a liquid drop in contact with an ideally smooth and planar solid surface, as schematized in figure 1.4.

When the system is at an equilibrium condition, the liquid drop exhibits a certain contact angle on the surface. This angle is the equilibrium contact angle Θ and it is related to the interfacial tensions of the liquid, solid and vapor phases by the Young equation (eqn. 1.6), where φ_{lv} is the surface tension of the liquid in equilibrium with its saturated vapor, φ_{sv} the surface tension of the solid in equilibrium with the saturated vapor of the liquid, and φ_{sl} the interfacial tension between the solid and the liquid.
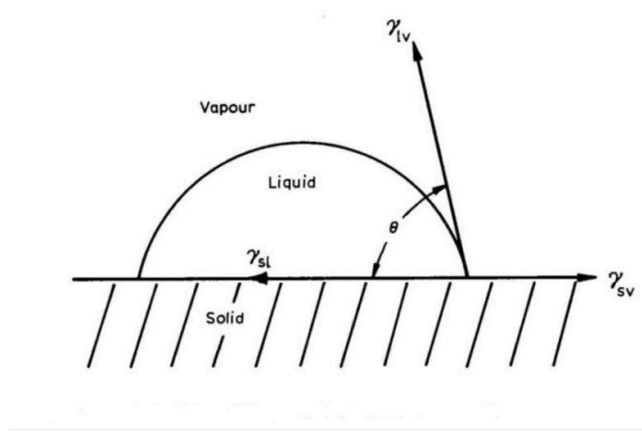
Figure 1.4: Equilibrium condition of a three-phase system: a liquid drop on a solid surface, exposed to a saturated vapor of the liquid [8].

$$\varphi_{sv} = \varphi_{sl} + \varphi_{lv} \cos \Theta \tag{1.6}$$

The liquid adhesive wets the surface when $\Theta < 90°$ and reaches the maximum theoretical wettability for $\Theta = 0°$. In this particular condition the liquid spontaneously spreads freely over the surface. When $\Theta > 0°$, it is also possible to completely wet the solid surface, but this requires the application of a pressure [8]. Thus the spontaneous liquid spreading takes place when

$$\varphi_{sv} \geq \varphi_{sl} + \varphi_{lv} \tag{1.7}$$

The adsorption of a vapor on a solid changes the surface tension of the substrate. The equilibrium spreading pressure of the vapor on the substrate is defined as in equation 1.8

$$\Pi_e = \varphi_s - \varphi_{sv} \tag{1.8}$$

where Π_e is the equilibrium spreading pressure, φ_s the surface tension of the substrate (solid or liquid) under vacuum, and φ_{sv} the surface tension of the substrate in equilibrium with the saturated vapor of the wetting liquid. Π_e is therefore the decrease of the surface tension due to the vapor adsorption. If the vapor pressure of the liquid drop is very low, as generally occurs with most polymer adhesives, the equilibrium adsorption of the vapor on the solid cannot take place, and eqn. 1.7 can be simplified as in the following.

$$\varphi_s \geq \varphi_{sl} + \varphi_{lv} \tag{1.9}$$

Equation 1.9 evidences that the wettability is enhanced on high energy surfaces. Sharpe and Schonhorn [31] emphasized the importance of the wetting on adhesion. The ability of the adhesive to spontaneously spread on the substrate when the joint is initially formed is one of the most important parameters able to influence the adhesive joint strength. They observed that an high joint strength should not result when polyethylene substrates are bonded using an epoxy adhesive. In this case the free energy of the polyethylene surface is lower than the surface tension of the epoxy adhesive and hence the wetting results limited. On the other hand, an hot-melt polyethylene adhesive strongly adheres to cured epoxy solid surfaces. Indeed the free energy of the cured epoxy substrate is higher than that of the polyethylene adhesive. Thus the Sharpe and Schonhorn's criterion essentially proposes that the adhesive should have a lower surface tension than the substrates to achieve true interfacial contact by wetting.

1.3.2 The Young-Duprè equation

Considering the Duprè equation for the work of adhesion (Eqn. 1.3) applied to the ideal Young system, where the phase 1 corresponds to the solid substrate and the phase 2 to the liquid adhesive, the Eqn. 1.10 is obtained:

$$W_a = \varphi_{sv} + \varphi_{lv} - \varphi_{sl} \tag{1.10}$$

It is important to underline that only the surface tension of the liquid phase can be measured with confidence by using various experimental methods (such as the Pendent Drop Method, the Sessile Drop Method and the DuNouy Ring Method), while the surface free energy of a solid substrate is not directly measurable experimentally [8]. The latter can be instead calculated by analizing

the wettability of the solid surface against a series of liquids with known surface tension by exploiting a series of models that are presented in the following paragraphs [8]. Exploiting the equilibrium contact angle described by the Young equation (eqn 1.6), the equation 1.10 leads to eqn. 1.11.

$$W_a = \varphi_{lv}(1 + \cos \Theta) \tag{1.11}$$

This formula simply relates W_a to the measurable contact angle and the known surface tension of the adhesive. Equations 1.10 and 1.11 are often referred to as the Young-Duprè equations [24]. Equation 1.11 suggests that the work of adhesion depends on the surface tension of the adhesive and the maximum adhesion is reached when the adhesive spontaneously spreads on the surface at a contact angle equal to 0°.

1.3.3   Fowkes theory and the geometric mean model

The theory proposed by Fowkes [32], widely discussed in literature [8, 21, 33] is aimed to describe the adhesion forces at the interface between a solid and a liquid phase. The model of the geometric mean, developed from this theory, can be used to calculate the surface tension of the solids from the measured contact angle of two liquids. Fowkes proposed that the surface free energy of a phase φ_i could be divided in two parts: the dispersion force component φ_i^d, and the polar force component φ_i^p, as defined in eqn. 1.12.

$$\varphi_i = \varphi_i^d + \varphi_i^p \tag{1.12}$$

The dispersive component φ_i^d contains the Van der Waals forces contribution such as permanent dipoles and London forces. The polar component φ_i^p refers to all the non-dispersion forces such hydrogen bonding and acid/base interactions. As Fowkes considered only the dispersion force interactions at the solid/liquid interface, he proposed that the geometric mean of these components would be a reliable prediction of the interaction energies at the interface, as reported in eqn. 1.13.

$$\varphi_{sl} = \varphi_s + \varphi_l - 2\sqrt{\varphi_s^d + \varphi_l^d} \tag{1.13}$$

where φ_{sl} is the tension at the liquid/solid interface, φ_l and φ_s are the surface tensions of the liquid and the solid, respectively. Starting from the work of Fowkes, Owens and Wendt proposed an equation that takes into account also the non-dispersion force components [24]. This theory, known as the geometric

mean theory, combines the polar and dispersive components to describe the interfacial tension at the solid/liquid interface as detailed in eqn. 1.14.

$$\varphi_{sl} = \varphi_s + \varphi_l - 2\sqrt{\varphi_s^d + \varphi_l^d} - 2\sqrt{\varphi_s^p + \varphi_l^p} \tag{1.14}$$

Equation 1.14 can be also included in the Young-Duprè equation to obtain eqn. 1.15:

$$1 + \cos\Theta = \frac{2\sqrt{\varphi_s^d + \varphi_l^d}}{\varphi_l} + \frac{2\sqrt{\varphi_s^p + \varphi_l^p}}{\varphi_l} \tag{1.15}$$

Equation 1.15 could be applied to calculate the surface free energy of a solid surface, resulting in the sum of its two components ($\varphi_s^d + \varphi_s^p$), by measuring the contact angle of at least two liquids having a known surface tension. Combining the geometric mean equation (eqn.1.14) to the Young-Duprè equation (eqn.1.10), the work of adhesion could be extrapolated and related to an adhesive/substrate system, being φ_a^d and φ_a^p the dispersion and polar components of the surface tension of the adhesive, respectively, and obtaining the eqn. 1.16.

$$W_a = 2\sqrt{\varphi_a^d + \varphi_s^d} + 2\sqrt{\varphi_a^p + \varphi_s^p} \tag{1.16}$$

According to equation 1.16, to maximize the thermodynamic work of adhesion W_a the values of the surface free energy components of both adhesive and substrate should be as larger as possible. But, in order to obtain true interfacial contact by wetting, the surface free energy of the adhesive must be lower than that of the substrate (cf. paragraph 1.3.1).

1.3.4 Surface free energy of solids and the effect of roughness

The solid materials can be distinguished between low-energy and high-energy surface materials [8, 21]. Polymers belong to the first group having surface free energies usually lower than 100 mJ/m^2. Metals and ceramics belong to the second group with surface tensions typically greater than 500 mJ/m^2. In figure 1.5(a) and 1.5(b) the surface free energy of some solids are listed: the values are obtained exploiting the above-mentioned methods (Fowkes equation and Geometric mean model).

Generally, low-energy surface materials are more difficult to be bonded than high-energy surface materials. On the other hand, too high energy surfaces

Solid surface	γ_s^D from Fowkes Equation (mJ/m²)	Values from *Geometric* mean Equation (mJ/m²)		
		γ_s^D	γ_s^P	γ_s
Polyhexafluoropropylene	18.0	11.7	0.7	12.4
Polytetrafluoroethylene	19.5	18.6	0.5	19.1
Poly(vinylidene fluoride)	—	23.2	7.1	30.3
Poly(vinyl fluoride)	—	31.3	5.4	36.7
Poly(chlorotrifluoroethylene)	30.8	31.4	2.1	33.5
Polyethylene	35.0	31.3	1.1	32.4
Polypropylene	30.2	—	—	—
Polystyrene	44.0	38.4	2.2	40.6
Poly(vinyl chloride)	—	40.0	1.5	41.5
Poly(methyl methacrylate)	—	35.9	4.3	40.2
Poly(vinylidene chloride)	—	42.0	3.0	45.0
Nylon-6,6	—	33.6	7.8	41.4
Poly(ethylene terephthalate)	—	41.8	3.3	45.1
Typical amine-cured epoxy	—	41.2	5.0	46.2
Rubber-toughened epoxy	—	37.2	8.3	45.5
Phenol–resorcinol resin	—	—	—	—
Urea–formaldehyde resin	—	—	—	—
Styrene–butadiene rubber	—	27.8	1.3	29.1
Acrylonitrile–butadiene rubber	—	26.5	9.5	36.0
Carbon fibre reinforced plastic (abraded)	—	27.4	30.6	58.0

(a)

Material	γ_s (theoretical) (mJ/m²)	Surface free energy (mJ/m²)		
		γ_s^D	γ_s^P	γ_s
Lead	442	99		
Copper	1360	60		
Nickel	1770			
Platinum	1915			
Mercury	319	200		
Graphite	1250	128		
Silver	890	74		
Gold		120 to 464		
Fe₂O₃	1357	107		
TiO₂ (anatase)		100		
Silica		78	209	287
Al₂O₃ (sapphire)	577–690	100		
Al₂O₃ (anodized)		125	44	169
BeO	1107			
Mica		30	90	120

(b)

Figure 1.5: Values of surface free energy for some low-energy polymer materials (a) and some high-energy ceramics and metals (b) [8]

are more reactive not only to adhesives but also to contaminants and particulate matter present in the atmosphere. In these cases, a physisorbed layer of contaminants could settle on the substrate surface and acts as a weak boundary layer between the adhesive and the adherend [8]. However, the principle of maximizing surface free energy in order to enhance adhesion, underlined in equation 1.16, is often exploited in many surface pretreatment technologies. For example, the acid etching is a typical way to treat low-energy polymers in order to improve adhesion by increasing the solid surface tension. The data reported in figure 1.6 support this argument: by increasing the surface free energy of the polyethylene through an acid etch pre-treatment, an enhancement of the adhesion strength is reached [21].

θ_{H_2O}	Shear strength, σ_f, psi	γ_s^d, dyne/cm	γ_s^p, dyne/cm	γ_s, dyne/cm
89 (Untreated)	10	36.0	5.31	41.3
55	175	36.0	20.9	56.3
51	187	36.0	23.5	59.5
50	240	36.0	23.5	59.5
46	290	36.0	25.7	61.7
42	440	36.0	28.0	64.0
38	575	36.0	29.9	65.9
38	600	36.0	29.9	65.9
36	700	36.0	31.2	67.2
35	675	36.0	31.2	67.2

Note: θ_{H_2O} is the contact angle of water on the untreated or chromic acid-treated polyethylene (treatment time up to 15 min).

Figure 1.6: Correlation between wettability, adhesion strength (measured through the *single lap shear test*) and surface free energy of the substrate, for an epoxy adhesive on polyethylene after different times of chromic acid etching [21]

In real systems, the surfaces are not smooth and planar, but rough or heterogeneous. A rough surface material has a bigger surface area affected by molecular bonding interactions [24] and this has an influence also on wettability. Indeed, in real rough surfaces the contact angle is subjected to an hysteresis, which makes it different from the equilibrium contact angle (Θ). The hysteresis is due to the fact that the real contact angle results from the existence of several closely spaced microscopic metastable states according to the roughness of the surface [21]. This resulting angle is the Wenzel angle (Θ_w) and is related to the equilibrium contact angle (Θ) by the Wenzel's equation (eqn.1.17):

$$\cos \Theta_w = r \cos \Theta \tag{1.17}$$

where r is the Wenzel's roughness factor defined by equation 1.18, as the ratio of the true surface area A (taking into account the peaks and valleys on the surface) to the apparent surface area A'.

$$r = \frac{A}{A'} \tag{1.18}$$

According to the Wenzel model, if on a smooth surface Θ is $< 90°$, an increase in the surface roughness will result in a smaller Θ_w, so an increase in the wettability of the substrate is reached. However, for a smooth surface where Θ is $> 90°$, the roughening of the surface will further decrease the wettability of the substrate.

1.3.5   Other thermodymamical models of adhesion

Starting from the geometric mean theory other models were developed to reliably predict the surface tension of solid materials and the work of adhesion. Wu [21] asserts that, despite the geometric mean model is a useful tool in systems involving high-energy surfaces, it is inadequate to predict the polar forces interactions of polymers and low-energy materials. Wu developed a model that was proven to be useful for the above-mentioned materials. Wu's model is based on the same parameters of the geometric mean model but it exploit the harmonic mean to predict the interaction energies at the interface.

Moreover Fowkes considered the problem of predicting the contribution of acid-base interaction with the geometric mean [34]. He argued that the acid-base interactions between the adhesive and the substrate could represent one of the major type of intrinsic adhesion forces that operate at the interfaces. He exploited Drago's works on the enthalpy of an acid-base interaction for implementing his theory. He supposed that the enthalpy of an acid-base reaction could be suitable for predicting the polar and hydrogen bond interactions that guarantee the maximum adhesion at the interface. In Drago's approach the enthalpy of an acid-base reaction, ΔH^{AB}, is defined as shown in eqn. 1.19.

$$-\Delta H^{AB} = C_A C_B + E_A E_B \tag{1.19}$$

where C_A and E_A are two constants able to characterize the acid in terms of tendency to electrostatic interactions and covalent bond formations, and similarly, C_B and E_B referred to the base. In this way, by replacing the polar component of the work of adhesion in equation 1.16, he obtained eqn 1.20

$$W_a = 2\sqrt{\varphi_a^d + \varphi_s^d} - (C_A C_B + E_A E_B) f n \tag{1.20}$$

where f is the factor for converting enthalpy values into free-energy values (close to the unit), and n is the number of acid-base pairs at the interface per unit area. The most mentioned limit of this approach [33] is the lack of sufficient data on C and E for potential substrates and adhesives. For these reasons other approaches, like the geometric mean, are more frequently employed. However, this model shows the advantage to relate more closely the surface tension components to the chemical nature of the materials involved. This approach also underlines the importance of the formation of primary interactions at the interface, such as covalent bonds, to reach the maximum levels of adhesion.

Recently different equations of state have been proposed to model the phenomenon. Those models have their origin from Young's equation, and have been proposed in different forms. The equation of state recently defined in the works of Neumann and co-workers is reported as an example in equation 1.21 [24, 35]

$$\varphi_{sl} = \varphi_s + \varphi_l - 2\sqrt{\varphi_s \varphi_l} e^{\beta(\varphi_s - \varphi_l)^2} \tag{1.21}$$

The term β in the equation of state (eqn. 1.21) is a constant that could be derived experimentally [35]. Neumann's equation of state can be combined with the Young's equation, to obtain the eqn. 1.22

$$\varphi_l(1 + \cos\Theta) = 2\sqrt{\varphi_s \varphi_l} e^{\beta(\varphi_s - \varphi_l)^2} \tag{1.22}$$

Using this method, the surface energy of a solid surface may be calculated using only a single contact angle measurement. The equation of state model provides also a better fit of the experimental data compared to the other thermodynamical methods.

1.4 Fracture mechanics of adhesive joints

In the previous paragraphs the theoretical concepts necessary to understand the adhesion phenomena were synthetically reported. But, as stated in paragraph 1.1.2 of this chapter, the adhesion is not the only parameter to take into account in the analysis of an adhesive bonded joint. A generic bonded joint is made of two substrates to be bonded, an adhesive between them and also two interfaces between the adhesive and the substrates in which the adhesion forces are acting. Furthermore, in the cases of real joints defects and imperfections reside in all the materials and the interfaces.

1.4.1   The hardening of the adhesive

As described in previous chapters, adhesive bonding requires the adhesive to be able to wet the adherends, creating an intimate molecular contact. Thus, the adhesive must be spread on the surface as a liquid and, once assembled the joint, it will have to withstand the mechanical stresses of its operating condition. The adhesive must possess those physical-mechanical properties necessary to transfer mechanical loads between the two adherends, properties that can be reached with the transition to the solid state. The hardening of the adhesive is a critical step that affects its final mechanical properties. The hardening may be accomplished by different strategies, which depend on the chemical nature of the adhesive itself. At least three main types of hardening strategies can be identify [6, 8]:

- Hardening by chemical reaction

- Hardening by cooling

- hardening by solvent evaporation

The majority of the adhesives used for structural applications, where high bond strength and excellent mechanical performances are required, harden by chemical reaction. This mechanism of hardening consists in depositing the adhesive on the surface to be joined in the form of a pre-polymer (monomers or oligomers). When the chemical reaction is activated, the short molecular chains bond to each other forming a solid crosslinked network in a process called polymerization or curing. The hardening technology is typical for thermosetting resins, the most common structural adhesives (e.g., epoxies, acrylics and polyurethanes resins) [6, 8, 22]. The way to initiate the polymerization governs the way the adhesive is applied.

- Two-component adhesives: the polymerization is triggered by an activator, which mixed with the pre-polymer right before the application, initiates the hardening reaction.

- One-component adhesives: the polymerization reaction is activated by external factors such as temperature, humidity and UV rays.

During the curing, the thermosetting resin changes from a liquid state to a highly crosslinked solid. The hardening process determines the physical and mechanical properties of the adhesive. The degree of crosslinking defines the number of bonds and interactions that are formed between the polymer chains.

The time and temperature of the curing reaction influence the degree and the way the crosslinked network is formed. A high crosslinked adhesive presents usually an high Modulus, a fragile behaviour and an high *glass transition temperature* T_g [6, 8, 36]. The T_g is the temperature at which a polymer changes its phase from a rubber-like soft material to a glass-like amorphous consistency.

The curing process can also be assisted by heating with the purpose of catalyzing the reaction. Heating usually helps to increase the degree of crosslinking, but the following cooling down can also introduce residual stress in the adhesive layer due to shrinkage [6, 8, 36].

1.4.2 Adhesive and cohesive fracture

According to the fracture mechanics approach, the real strength of a material is usually much lower than its theoretical strength for the presence of defects or cracks, that cause the amplification of the stress at the local level, sometime exceeding the fracture strength. Furthermore, materials can dissipate stresses by means of the plastic deformation. The theory of fracture mechanics developed by Griffith and Irwin could also be applied to the adhesive technology [21].

In terms of energy concept, adhesive fracture and cohesive fracture (see paragraph 1.1.2) are similar. In cohesive fracture two similar surfaces are created, whereas in adhesive fracture the two new surfaces are dissimilar [21]. The adhesive fracture energy G_c could be expressed as the sum of two components: the intrinsic adhesive fracture energy G_0, and the irreversible work due to plastic deformations, Ψ (eqn. 1.4). The intrinsic fracture energy G_0 depends on the work of adhesion W_a or cohesion W_c on the basis of the type of fracture raised in the joint. In the case of a completely cohesive fracture in the adhesive layer, equation 1.4 becomes

$$G_c = W_c + \Psi \tag{1.23}$$

whereas in the case of a completely adhesive fracture the equation 1.24 is obtained

$$G_a = W_a + \Psi \tag{1.24}$$

where G_a and G_c are the adhesive (or interfacial) and cohesive fracture energy, respectively.

To better understand, it is necessary to consider a linear elastic material containing a central elliptical crack, under a state of plane stress normal to the crack propagation, as schematically reported in figure 1.7.
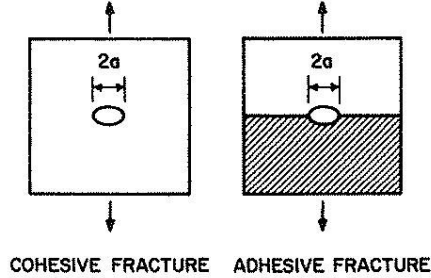
Figure 1.7: Comparison between cohesive and adhesive fracture [21].

According to the Griffith criterion, in the case of the cohesive fracture, the tensile stress necessary to break the material, namely the fracture stress f, is related to the fracture energy by equation 1.25:

$$f = \left(\frac{EG_c}{\pi a} \right)^{1/2} \tag{1.25}$$

where E is the elastic modulus and a the half-length of the initial crack. This relation is equally applicable to adhesive (interfacial) fracture, where two dissimilar crack surfaces are created, as resumed in equation 1.26.

$$f = \left(\frac{E_{12}G_a}{\pi a} \right)^{1/2} \tag{1.26}$$

In this case G_a is the adhesive fracture energy and E_{12} is a composite elastic modulus, calculated according to equation 1.27.

$$E_{12} = \frac{E_1 E_2}{\Phi_1 E_2 + \Phi_2 E_1} \tag{1.27}$$

where Φ_1 and Φ_2 are the fractional length of the two phases, and E_1 and E_2 are the Young moduli of phase 1 and phase 2, respectively.

Thus the adhesive strength is determined by the flaw size, fracture energy and viscoelastic properties of adhesive and substrate . The fracture energies G_c and G_a depend on the work of cohesion and the work of adhesion, respectively, as pointed out by equation 1.23 and 1.24. The locus of the propagating crack will therefore depend on the energy required to break the attraction forces at

the interface, rather than the cohesive forces of the two phases [21]. A true interfacial separation (adhesive fracture) will occur when the interfacial strength is weaker than the bulk strength. In terms of the Griffith criterion, this relation can be expressed as stated in equation 1.28

$$\left(\frac{E_{12}G_a}{a_{12}}\right)^{1/2} \leq \left(\frac{E_2 G_2}{a_2}\right)^{1/2} \leq \left(\frac{E_1 G_1}{a_1}\right)^{1/2} \tag{1.28}$$

considering in this case, the phase 2 is weaker than the phase 1. For example, the phase 2 could represent the adhesive material and the phase 1 the substrate material. In many cases involving metal joints, the adhesive is weaker than the substrates and so the failure could occur cohesively in the adhesive layer, interfacial, or in a mixed mode [8]. In complex joints the phases in which the crack could propagate are multiple. For instance when dissimilar material are joined with an adhesive, the phases could be: the first material, the interface between the adhesive and the first material, the adhesive, the interface between the adhesive and the second material, the second material [6].

The correct identification of the locus of failure has a great importance for adhesion problems. If the failure is cohesive in adhesive layer, efforts should be directed toward strengthening the adhesive material, for example through toughening strategies, or modifying the adhesive in order to withstand some particular stress or environmental conditions. On the other hand, if failure occurs at the interface, the solution would be to increase the interfacial attraction between adhesive and substrate, for instance by applying a primer or by changing the surface tension of the substrate exploiting a proper pre-treatment [6].

1.4.3   Micro-mechanism of failure

The real fracture is an irreversible process, because it involves largely plastic work and energy dissipation during the crack growing. The possible micro-mechanisms of crack growth in rigid structural adhesives influence the measured values of the fracture energy Gc and thus they are the bases of the strategies for toughening an adhesive.

A crack that propagates cohesively in the adhesive layer involves the rupture of intrinsic bonds of the adhesive material. However this mechanism is not the only energy dissipative process that occurs in the proximity of the crack tip. Indeed, the micro-mechanisms reported in the following, usually represent the main source of energy absorption in the adhesive material, and their extent influences the values of the observed fracture energy [8].
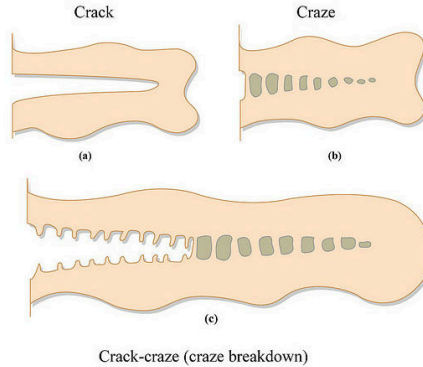
Figure 1.8: Schematic representation of crack and craze in glassy polymers [37].

Shear yielding. This micro-mechanism consists in an inhomogeneous plastic deformation of the material in proximity of the crack tip. In highly crosslinked polymers, the shear yielding could involve little energy dissipation highly localized about the crack tip, and hence results in a brittle fracture. If the extent of the shear deformation around the crack tip increases, the propagation of the crack will become increasingly ductile in nature and the toughness of the material generally rises [8].

Crazing. This mechanism involves cavitations of the material with a consequent volume increase, hence the energy is dissipated through plastic deformations, like the shear yielding mechanism. A craze is formed when an applied tensile stress causes micro-voids to nucleate in an area of stress concentration. The resulting localized yielded region consists of an interpenetrating network of voids and fibrils of plastically deformed polymeric material. The crazing is usually a precursor of a brittle fracture, typically in thermoplastic glassy adhesives. A schematic representation of crazing is shown in figure 1.8 [8,37].

Multiple deformation. Both shear yielding and crazing are energy absorbing processes but frequently lead to brittle fracture due to the fact that they are confined in a small volume compared to the size of the specimen. In the perspective of toughening the adhesive material, the total amount of plastic energy absorbed needs to be increased. The multiple-deformation mechanism consists in promoting localized mechanisms, such crazing and shear yielding, in many sites inside the specimen. For instance this is the case of the rubber-

toughened epoxy and acrylic systems, where the rubbery particles absorbs the energy through deformation processes [8].

Crack pinning. This mechanism involves the crack propagation being impeded by the rigid, impenetrable, well-bonded particles. When a crack meets an array of such obstacles it becomes pinned and tends to bow out between the particles forming secondary cracks. Thus a new fracture surface is formed and the length of the crack front is increased. Energy is required to form a new fracture surface and in the propagation of a non-linear crack front. In adhesives, the rigid toughening phase usually consists in alumina or silica particles [8].

1.5 The influence of joint geometry

The geometry of the junction and the related type of stress induced in the adhesive layer strongly influence the strength of the adhesive joint. The stress distribution inside the adhesive layer is dependent on the geometry and the type of loads which act on it. Unfavorable joint geometry presents stress concentrations that could locally exceed the fracture strength of the adhesive and bring the joint to the rupture [7, 8].

1.5.1 Types of stress in adhesive joints

Considering adhesive bonded joints, there are four types of stress which are commonly involved [8]. As pointed out in figure 1.9, these stresses could be classified as: (a) normal stresses, that are normal to the plane on which they act and may be tensile or compressive; (b) shear stresses, that are parallel to the plane on which they act; (c) cleavage stresses, which typically result from an offset tensile force or bending moment; (d) peel stresses, which arise if one or both of the substrates are flexible.

Generally, the total stress of a system could be represented by the two principal components of normal and shear stresses, but in the adhesive technology it is important to identify also the other two types of stress. Indeed the load capability of a joint is strongly influenced by the types of stress acting on it. Usually adhesives withstand better compression or shear stresses and are susceptible to tension, cleavage or peel stresses. For instance, a joint subjected to a peeling load, is affected by a very high stress and strain concentration on the boundary line, so the fracture will occur relatively easily [7, 8].

Therefore the joint must be designed to keep stress concentration at a minimum but also to try to distribute the imposed loads within the adhesive layer
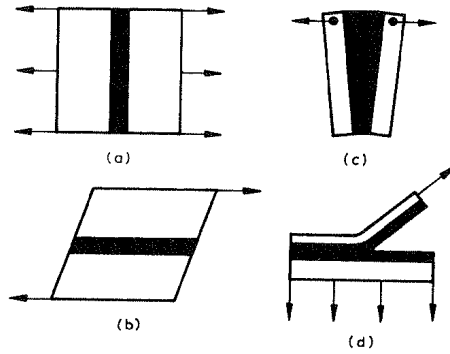
Figure 1.9: Types of stress: (a) normal (or direct) stress, (b) shear stress, (c) cleavage stress, (d) peel stress [8].

as a combination of compressive and shear stresses, avoiding tensile, cleavage and peel stresses as much as possible. Figure 1.10 illustrates how a joint could be differently designed by taking into account the above general comments in view of a favourable stress distribution at the interface.
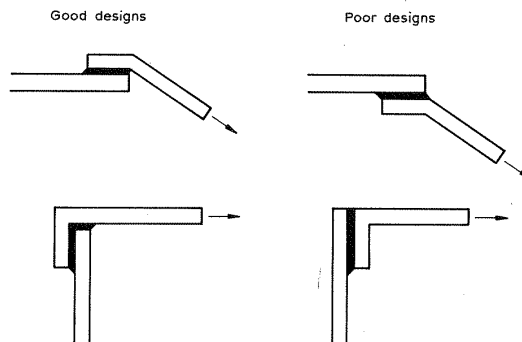
Figure 1.10: Schematic diagram of some *good* and *poor* joint design [8].

A mathematical analysis of the joint geometry is then necessary to understand the stress distribution in an adhesive bonded joint. The stress distribution provides useful information in order to avoid stress concentration that could

bring the joint to a premature rupture [7].

1.5.2 Stress analysis of an adhesive joint

The first approach in stress analysis was the analytical approach, which consists in defining closed-form equations which characterize the stresses and strains in the joint. The first analyses were made up by Volkersen [38] on the model of the single lap joint. The single lap joint (see Chapter 3) loaded in tension received considerable attention from the stress analysts, because it is a simple and convenient test geometry for evaluating different adhesive formulations. Furthermore, it is the most common joint design employed in industry: indeed it consists in two sheets joined by a simple overlay. Volkersen assumed the adhesive and the adherend to be linear elastic solids, and considered the adhesive layer stressed only in shear, while the adherends stressed only in tension. An example of Volkersen analysis is schematically reported in figure 1.11, where d_1 e d_2, are the thickness values of the two substrates, l_a is the overlap length, h_a is the thickness of the adhesive layer, τ_{12} is the shear stress in the adhesive and τ_0 is the applied shear stress. From Volkersen analysis emerged that in the single lap
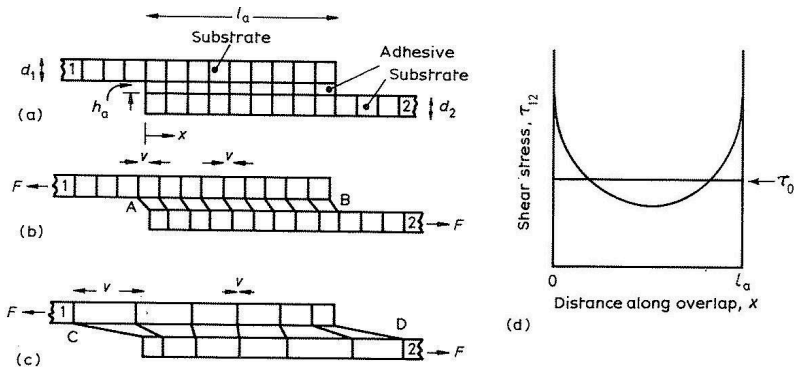
Figure 1.11: Schematic representation of single lap joint: (a) unloaded, (b) loaded in tension with inextensible substrates, (c) loaded in tension with elastic substrates, and (d) distribution of elastic shear stress in the adhesive layer [8].

joint an important stress concentration is present at the edges of the adhesive layer. This evidence is a primary issue to take into account in designing similar joint geometries.

For what concern more complex joint geometry the analytical approach is unlikely applicable. It would be difficult to obtain an overall system of analytical equations for predicting the mechanical behavior of more complex adhesive joints. In addition, plastic deformations of the materials are difficult to incorporate in analytical models. To overcome these problems, the finite element analysis (FEA) was frequently exploited since 1970s [39].

The FEA method is a numerical method in which the joint is divided into discrete parts, each of which has to be compatible in the force and displacement continuum with adjacent elements. Then the equations of state need to be solved numerically by a computer for each change in values of any parameter. The great advantage of FEA is the possibility to determine the mechanical properties of an adhesively bonded joint of almost any geometrical shape under various load conditions. Both linear and non-linear elastic and elastic-plastic finite element analysis may be performed. The application of FEA to adhesively bonded joints has increased significantly in recent years, and a considerable amount of work has been carried out on different types of adhesively bonded joints by various researchers [7, 39–41].

1.6   Service life of adhesive joints

An adhesive joint must guarantee the needed adhesive performance during all the service life of the joint. Continuous exposure to service conditions which include dynamically and statically applied loads and exposure to hostile environments such as water, chemicals, etc., could compromise the durability of an adhesive joint [6–8]. The service life of a joint could be estimated through laboratory testing in which trial joints are exposed to definite environment conditions under a precisely known applied load.

1.6.1   Creep and fatigue of adhesive joints

Creep rupture is the phenomenon of fracture which occurs after a certain time from the application of a constant load. Adams and others [7] reported that in normal design under static loading, a continuous extension in the direction of the principal load is not expected whilst the adhesive is maintained below its glass transition temperature T_g. Thus, overloading is far more likely to lead to stress rupture than to creep. However, at high temperatures, which maintain the adhesive close to its T_g, some creep phenomena might occur. Indeed, experiments of static loading are usually carried out in presence of hostile environments.

Kinloch [8] used a fracture mechanics approach to study the creep behaviour of double cantilever beam joints (for adhesive joints tests see Chapter 3) which was pre-cracked whit a sharp crack. He found a linear relationship between the applied adhesive fracture energy G_{Ic} and the log of the time-to-failure. The failure time decreases as the value of the applied G_{Ic} increases. He suggested that these results could be modelled by postulating a fracture criterion based on the requirement of a critical crack-opening displacement, δ_{tc}. Hence crack propagation does not occur whilst δ_t does not reach the critical value δ_{tc} defined by the equation 1.29

$$\delta_{tc} = \frac{1}{\varepsilon_{ay}} \frac{G_{Ic}}{E_a} \tag{1.29}$$

where E_a is the modulus of the adhesive, and ε_{ay} is the yield strength.

An interesting parameter for short term operation is the time-to-failure under static loading [7]. This parameter is usually used in rocketry where certain materials must remain efficient at high stresses for a limited working life. In adhesive joint it is important to know the rate at which the strength of the joint declines. This rate determines the time at which the joint is insufficiently strength to be considered safe under the applied loads.

Rather more information exists on fatigue behavior. The fatigue is the phenomenon of failure or fracture of a joint under repeated or oscillatory loading. For a given stress amplitude, joints will fail in much shorter time than the creep, where a constant stress of the same amplitude is applied. Most of the interest in the subject is focused on the crack growth of a pre-existent crack, rather than the crack initiation process, which is difficult to model. Furthermore materials are not perfect, and thus the propagation of a pre-existing crack is the mechanism which usually controls the fatigue life [7].

A fracture mechanics approach to describe the fatigue crack growth in adhesive joints is reported by Mostovoy e Ripling [42]. They study the crack growth rate employing the double cantilever bean test geometry (for adhesive joints tests see Chapter 3) with aluminum alloy substrates bonded with different adhesives. They found a relation between the crack growth rate per number of cycles da/dN and the range of adhesive fracture energy ΔG_I, as shown in equation 1.30. The range ΔG_I is defined as the difference between the maximum and the minimum adhesive fracture energy G_I, which the double cantilever beam test develops in fracture mode I (opening fracture mode).

$$\frac{da}{dN} = A_f \Delta G_I^q \tag{1.30}$$

The parameters A_f and q are constants and their values typically depend upon material variables, temperature, frequency, stress ratio and environment. The value of A_f varies between about 10^{-14} and 10^{-16}, whereas that of q between 2 and 5. The studies reveal that the relation between da/dN and ΔG_I is sigmoidal in shape. Crack growth rate decreases to very low values as ΔG_I approaches some limiting threshold value. On the other hand, the value da/dN increases to very high values as ΔG_I approaches the typical G_{Ic}.

These evidences introduce an important concept in fatigue, the endurance limit. This consist in the peak cyclical load which a material can sustain indefinitely. If this limit does exist really or not for adhesive joints is not yet demonstrated. From literature [7, 8] it seems difficult to apply this concept to an adhesive bonded joint. There are no strong evidence of a threshold value of ΔG below which dynamic fatigue crack growth would not occur, although some indication has been reported. For instance, Matting and Draugelates [43] studied the sinusoidal stressing of a single overlap shear test piece, using aluminum substrates. The Wöhler line extrapolated was analogue to the typical Wöhler line in metal testing. The curve seems to be characterized by a loading below which no test piece fail. This may be referred to the presence of an endurance limit. In that case the failure detected below that particular stress level was likely to be initiated by an adherend (metal) failure.
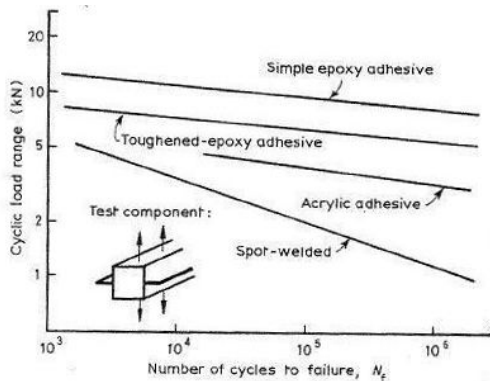

Figure 1.12: Fatigue properties of steel double-box hat structures either adhesively bonded or spot welded [44].

Usually a general adhesive bonded joint is considered to present a greater performance under fatigue loading compared to other classic joining techniques

[5–8]. This can be essentially due to the fact that adhesives are able to give a more even stress distribution in the joint compared to other joining techniques such as spot weld or mechanical fasteners, as shown in figure 1.12.

1.6.2 Effect of the environment

One of the most important requirements of an adhesive joint is its durability to the operating environment. An adhesive must retain a significant proportion of its load-bearing capability under every environmental condition that could encounter during all its service life. Particularly, water and heat are the most common and dangerous degrading agent. The effect of simultaneous exposure to both mechanical stress and hard environmental conditions is often more severe than each factor taken separately [6–8, 22].

Moisture gives the greatest problems in terms of environmental stability for many adhesive joints. Two possible effects can take place: the degradation of the bulk adhesive material and the degradation of the adhesion bonds at the interface [6].

Bulk material. Both the physical and chemical characteristics of the adhesive bulk material will be modified by the water absorption. The physical changes arise mainly from the plasticization effect of the absorbed water. Water permeation causes an increase in the mobility of the polymeric chains that results in the plasticization of the adhesive material with a consequent decrease in the yield strength. The glass transition temperature T_g generally decreases due to the reduced forces between molecules. The plasticization effect could initially bring to an increase of the plastic deformation at the tip of the crack growth, resulting in an apparent increase in toughness (cf. paragraph 1.4.3). Nevertheless since the T_g and the yield strength of the adhesive become appreciably lower, the general performance of the adhesive generally decreases. The adhesive could be also subjected to an increase in volume or swelling. These physical changes are usually reversible, since the adhesive generally recovers these properties after drying. On the other hand, the chemical changes that arise by water uptake are irreversible and more damaging. Because of its polarity water could induce chain scission and hydrolysis of chemical bonds bringing to an effective deterioration of the bulk material, as schematically represented in figure 1.13. The hydrolytic instability depends mainly on the chemical structure of the base adhesive [6–8, 45].

Interface. Water can also permeate the adhesive and preferentially migrate to the interface region displacing the adhesive at the bond interface. A classic effect of this deterioration is the increase in the percentage of adhesive failure.
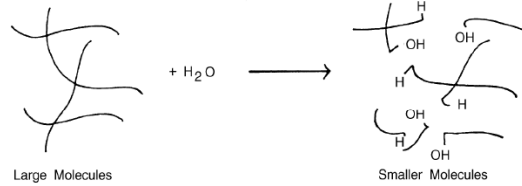
Figure 1.13: The degradation of polymer chains by reaction with water through hydrolysis [45].

This mechanism consists in the competition between the adhesive and other chemicals for surface sites leading to a displacement of the adhesive from the surface. Adhesive adsorbed at the surface sites would be displaced by the water molecules. This effect is greatly dependent on the type of adhesive and the adherend material. It is particularly present on high energy substrates, like metals. Corrosive environments such as salt water and salt spray are also a serious problem on metal joints. In these conditions the corrosion of the metal interface can take place, resulting in a weak boundary layer. Surface preparation methods are commonly employed to retard the degradation of adhesive joints in these kind of environments [6–8].

1.6.3   Operating temperature range

The adhesive must guarantee its mechanical properties at the maximum and minimum operative temperature. Generally an adhesive should have a glass transition temperature above the normal operating temperature [6–8]. High temperature adhesives are usually characterized by a rigid polymeric structure, high softening temperature, and stable chemical groups. Low temperature adhesives must be able to absorb stresses and have a high fracture energy at low temperatures [6].

All polymeric materials are degraded to some extent by exposure to elevated temperatures. In this conditions, not only short-term physical properties are lowered, but these properties will also likely degrade with prolonged thermal aging. Prolonged exposure to elevated temperatures of a structural crosslinked adhesive may cause chain scission of polymer molecules and oxidation (if oxygen or a metal oxide interface is present) resulting in lower cohesive strength and weak boundary layers. The effects of thermal cycling and the resulting internal stresses on the joint interface must be also taken into account. This aspect must

be considered mainly in the bonding of dissimilar materials, when the thermal expansion coefficients of the adhesive and the substrates are different. Most of all, the temperature has a synergic effect with moisture degradation. Indeed, usually, high temperatures are commonly employed for accelerating ageing in laboratory testing [6–8].

Chapter 2

The hybrid bonded-interference fitted joint

Abstract

    The main drawback of adhesives concerns their durability in harsh conditions due to their polymeric nature. Nevertheless, adhesive bonding can be used in combination with other traditional joining methods generating a hybrid joint with the aim of combining the advantages of the different techniques. A brief overview of hybrid joints is provided in the first section. Then, a detailed description of the interference fit joining technique is given. This mechanical fastening technique, combined with adhesive bonding, provides the hybrid joint that is the object of this research. Indeed, the hybrid interference fitted/adhesive bonded joining technique is realized by forcedly fitting together two cylindrical components after having placed an adhesive between them. The clamping pressure given by the interference and the resistance of the adhesive act simultaneously on the mating surfaces. The description of this hybrid joining technique and a literature review of its state of the art are presented in the third section of this chapter.

2.1   Hybrid adhesive joints

Adhesive bonding is a suitable technology to bond dissimilar materials and often to obtain a good uniform stress distribution in the joint area [6]. However, as adhesives have a polymeric nature, they are subjected to durability issues, especially in harsh working conditions (more details in paragraph 1.6.2). In order to overcome these problems, adhesive bonding can be used in combination with other traditional joining methods, such as mechanical fastening techniques (e.g. rivets or bolts) or welding techniques, generating a hybrid joint. Hybrid adhesive joints are designed with the aim to exploit the advantages of the different techniques and, if possible, to overcome their drawbacks [9]. The most common hybrid joints are weld-adhesive, rivet-adhesive, clinch-adhesive, interference fit-adhesive bolt-adhesive and adhesive-adhesive (more than one adhesive along the overlap). In figure 2.1 an example of clinch-adhesive joint is reported.
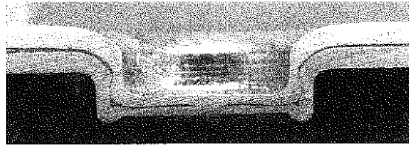
Figure 2.1: A section of a clinch-adhesive joint [46].

2.2   Interference fit joint

This paragraph focuses on the interference fitted/adhesive bonded joining method. The interference fit is a common technique to joint cylindrical part together. The most common joint geometry consists in a shaft fitted into a hub. In order to guarantee the coupling, the hub must be mounted on the shaft through forcing. In this case an *interference* (δ) exists among the hub and the shaft, being the diameter of the shaft little greater than that of the hole present in the hub.

The degree of interference between two components is linked to machining errors and tolerances. The nominal dimensions of a component given by the designer are referred to ideal geometric surfaces, which are impossible to obtain even by using precise and accurate manufacturing. Due to dimensional errors, a machined component displays real dimensions that differ from the ideal ones. For this purpose it is mandatory to specify the limits in which the errors are
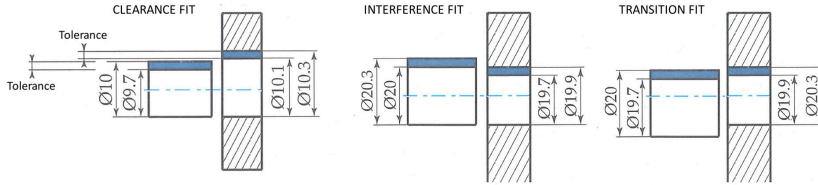
Figure 2.2: Example of a clearance, an interference and a transition fit [47].

admissible. Fixing in this way the *tolerance*, that represents the absolute value of the difference between the maximum and the minimum possible dimensions.

Considering sizes and tolerances of a generic hub and shaft, three types of fit can be distinguished:

Clearance fit. The shaft should be free to move inside the hole, so that the lower tolerance limit of the hole should be greater or at least equal to the upper limit size of the shaft.

Interference fit. In order to ensure a forcing between the hub and the shaft, the upper tolerance limit of the hole should be smaller or at least equal to the lower limit size of the shaft.

Transition fit. A third possible coupling exists when the tolerance zones of the hub and shaft are partly or completely superimposed. In this case both clearance and interference may occur.

A schematic representation of the three possible fitting is reported in figure 2.2.

The ISO system of tolerance standardizes the possible couplings between hubs and shafts. The system classifies the possible couplings between hubs and shafts by exploiting two parameters: the *grade of tolerance* and the *basic deviation*. The *grade of tolerance* defines the amplitude of the tolerance and so the quality and the precision of the manufacturing. Due to the fact that the permissible error is grater in the case of high component dimensions and it is lower for smaller component dimensions, the *grade of tolerance* is normalized iwith respect to the component dimensions. The system provides 20 grades of tolerance marked "IT" with attached the grade of accuracy (for instance IT01, IT0, IT1 ... IT18). The *basic deviation* defines the position of the tolerance zone related to the nominal size of the component. The system provides 27 positions identified by the capital letters for the hubs (A, B, C, ... ZC) and lowercase letters for the shafts. By convention on the basis of constructional, technological and economic reasons, the ISO system is organized in two reference systems:

the former have as reference the h6 shaft, the latter the H7 hub. The H (or h) position is setted as the lower limit of its basic deviation coincide with the nominal size of the material. A schematic representation of a basic coupling between two shafts (A & B, coupled with clearance and interference, respectively) and a hub characterized by the same nominal diameter but different grades of tolerance and basic deviation is reported as an example in figure 2.3.
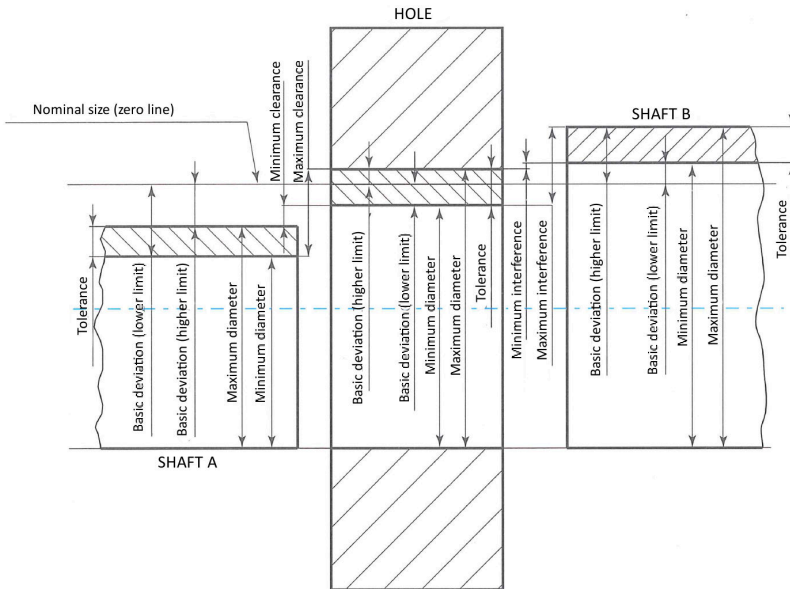
Figure 2.3: Schematic representation of a hole coupled with clearance to a shaft A and with interference to a shaft B. Every components have the same nominal diameter, but different basic deviation and tolerances [47].

Even with the limitation of the two systems based on shaft or on hole, the possible pairs would still be too many. The field in which the designer must choose the tolerance is influenced also by economic and technical needs of the mechanic workshops. Therefore, a selection of tolerance zones whose coupling leads to the recommended fits is usually exploited with the purpose of decreasing the number of tools and gauges needed [47]. The two cylindrical components could be assembled through two principal methods: *shrink-fit* and *press-fit*. In

the *shrink-fit*, the coupling is realised by a thermal expansion, whereas in the *press-fit* the coupling is realised by means of a standing press.

In the following, the push out force needed to decouple a generic interference fit joint will be described from an analytical point of view. It is reported [12, 15, 48] that the strength of a solely interference fit joint depends on the hub pressure, the coefficient of friction and the contact area, as resumed in the equation 2.1:

$$F_{int} = \mu P A \tag{2.1}$$

where A is the coupling surface, μ the static friction coefficient between the shaft and the hub and P the mean coupling pressure. This last parameter is strictly related to the nominal interference and the geometry of the components by the Lamè's thick walled cylindrical theory.

According to the Lamè's theory, when press or shrink fit is used between 2 cylinders of the same material, an interface pressure P is expected between them. The system on which the lamè's theory is based is showed in figure 2.4. In this system the external diameter of the inner cilinder b_{inner} is considered
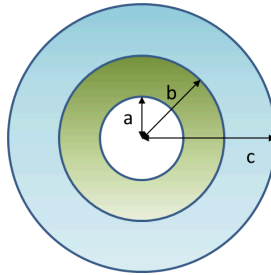
Figure 2.4: Schematic representation of the Lamè's theory system based on two thick walled cylinders.

equal to the inner diameter of the outer cylinder b_{outer}, thus indicated with the same value b. This equivalence leads to the boundary condition that the interference between the two cylinders $\delta = b_{inner} - b_{outer}$ should be very small in value compared to the radius b. According to Lamè's theory, if the axial stresses are neglected, the radial contact pressure P developed between the hub and the shaft can be estimated through the equation 2.2.

$$P = \frac{E\delta}{b} \left[\frac{(c^2 - b^2)(b^2 - a^2)}{2b^2(c^2 - a^2)} \right] \qquad\qquad (2.2)$$

where E is the Young modulus, δ the radial interference between the two cylinders, a the inner radius of the inner cylinder, b the outer radius of the inner cylinder as well as the inner radius of the outer cylinder and c the outer radius of the outer cylinder.

2.3   Hybrid adhesive and interference fit joint

The implementation of an adhesive into an existing interference fit design can lead to a considerable strength enhancement. The hybrid adhesive-bonded/interference-fitted joint is realized by coupling together two cylinders, after having placed an adhesive between them. Thus in this hybrid joint both the pressure between the components and the resistance of the adhesive act on the same coupling area. Both the *shrink-fit* technique and the *press-fit* technique could be exploited to assembly the joint.

2.3.1   Assembly techniques

In the case of the *shrink-fit*, the preferred approach is to apply the adhesive to the male component and to heat the female to obtain the needed fitting clearance. In order to insert the shaft at least a gap of 0.1 % of the nominal diameter (0.01 mm minimum) should be achieved [12]. The maximum temperature must be set in relation to the curing protocol and the thermal properties of the adhesive employed. On the other hand, it is possible to freeze the male component and apply the adhesive to the female one. This technique is not generally recommended because the condensation (frost) on the cold component can affect the adhesive curing and thus the bond strength. An experiment, carried on during the thesis work, concerning the effect of bonding a frozen steel substrate is reported in figure 2.5. In this experiment one of the two steel sheets of a lap shear joint is dipped in liquid nitrogen prior to bonding. Then, immediately after removing the sheet from liquid nitrogen, the lap shear joint is assembled. The experiment is repeated with both an acrylic anaerobic and an epoxy adhesive. The adhesion strength of lap shear joints bonded in standard conditions and bonded after the freezing of a substrate are compared. A lowering of the performance of the joint in the case of the frozen substrate is observed with both the employed adhesives. Regarding the epoxy adhesive, the decrease is

relevant because the frozen moisture deposited on the cold substrate can affect the curing mechanism of the resin, resulting in an incomplete polymerization of the adhesive. On the other hand, in acrylic samples the little drop of resistance is probably attributable to the thermal expansion of the substrate that is defrosting during the adhesive curing. Croccolo et al. [48] studied the effect of the assembly technique on the final performance of the hybrid interference fit joint bonded with acrylic anaerobic adhesive. They found that cryogenic fitting determines an appreciable decay of the adhesive shear strength, while the negative effect of using a heated hub is less severe.
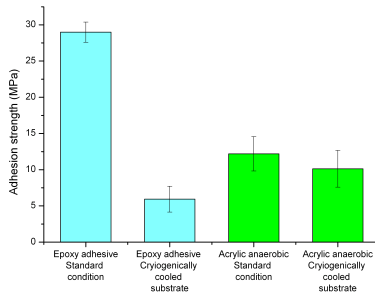
Figure 2.5: Shear strength of epoxy and anaerobic acrylic adhesive lap shear joints, bonded in standard condition and bonded with a frozen substrate.

In the case of the *press-fit* assembling technique, the adhesive is generally applied as a film to one or both substrates and the parts are pressed together. Even if the thermal shrinkage of the substrates and the adhesive is avoided, the press-fit technique introduces the important parameter of the friction between the parts during coupling. The wiping or pushing away of the adhesive during the assembly is a circumstance impossible to avoid and difficult to control. Moreover the alignment of the assembled samples must be guaranteed. The insertion of the shaft into the hub with misalignments can easily occur, implying a great increase of the pressing forces. The study of Croccolo at al. on the effect of the assembly technique [48] revealed that press-fitted joints showed a slightly lower shear strength than joints assembled with clearance between the components (*slip-fit*) at room temperature with acrylic anaerobic adhesives. The Authors attributed the poor results of the *press-fit* technique to the stripping away of the adhesive from the mating surfaces during the assembling.

A summary of the assembling techniques and their connected most limiting

factors is presented in table 2.1.

Table 2.1: Liming factors of the hybrid-joint assembly techniques

Shrink-fit		Press-fit
Heat affects the curing reaction and could degrade the pre-polymers	Condensation (frost) on the cold component could affect the adhesive cure	Wiping or pushing away of the adhesive during the pressing operation
Difficult to reach the needed gap with small diameters where the thermal expansion is too small		Axiality of the assembly need to be controlled

The acrylic anaerobic adhesives, commercially named *retaining compounds* [49], are usually exploited in the interference fitted / adhesive bonded hybrid joints, being possible in this configuration to exploit their curing technology based on a one component adhesive. In this system, in fact, the presence of the interference contributes to guarantee the anaerobic polymerization, protecting the curing layer of adhesive from the oxygen (for further information on anaerobic polymerization see section 4.1).

2.3.2 Technical literature review on interference fit-adhesive bonded hybrid joint technique

The studies on interference fit-adhesive bonded hybrid joint technique began in the late 90's together with the increase of the use of anaerobic adhesives, especially in the automotive industry [50, 51]. Anaerobic adhesives have been effectively used to improve the performance of mechanical tightening joints, for example bolted joints, flanged couplings or interference fits. Considering that this hybrid joint is a combination of the adhesive bonding and the mechanical tightening based on friction, the first main object of research was the comprehension of the interaction of these two techniques. The first method that was developed was based on the concept of the superposition of the effects [12, 13]. According to this idea, the resistance of the hybrid joint is provided by the sum of the contributions due to the friction forces and the adhesive along the joint area, as two variables computed independently. This approach has been developed by adhesive suppliers companies as a simple method to predict the total strength of this joint in industrial components. The superposition of the effects can be summarized by the equation 2.3 for what concern the relation for

a static axial push out of force [12]:

$$F = \frac{\pi d l \left[(\tau_a f_c) + (P\mu) \right]}{1000} \tag{2.3}$$

and the equation 2.4 for a static torque [12]:

$$T = \frac{\pi d^2 l \left[(\tau_a f_c) + (P\mu) \right]}{2000} \tag{2.4}$$

where F is the static axial push-out force, T the torque capacity, d the nominal joint diameter, l the bond length, τ_a the static shear strength of adhesive according with ISO10123, P the radial contact pressure due to the interference fit calculated using the *thick walled cylinder theory* (eqn.2.2), μ the coefficient of friction, f_c a product of different correction factor ($f_1 \cdot f_2 \cdot f_3 \cdot f_4 ....$).

The correction factors have been created to adjust the adhesive strength value to the actual physical and operating conditions and are based on empirical testing and practical experiences. Three examples of possible correction factors are reported in the following [12]:

- f_1: type of material. For acrylic anaerobic adhesive the correction factor takes into account the affinity of the adherend with the curing technology of these adhesives (Steel = 1.0; Aluminum = 0.5; Stainless steel = 0.8).

- f_2: type of assembly. In this case the correction factor takes into account the assembly technique of hub and shaft (Press fit = 0.5; Shrink fit = 1.2).

- f_3: geometry. The shear stress of the hub shaft sample is not evenly distributed across the overlap length, and maximum stresses are concentrated at the edge of the components. The correction factor value depends on the bond length diameter ratio (l/d ratio).

Dragoni and Mauri [13] stated that this simple approach was not always confirmed at the experimental level. For instance, on the basis of the experiments conducted by Sawa, Yoneno et al. on shrink fitted cylindrical joints [16, 17, 52], it emerges that while the strength of only shrink-fitted joints increases with an increase of shrink-fit interference, the joint strength of bonded shrink-fitted joints is independent on the shrink-fit interference. The data related to the numerical and experimental results of the static pull-out of hub-shaft samples [16] are presented in figure 2.6. It can be seen that the bonded shrink-fitted samples had not the same dependence on the parameter δ_s/b_1 (the interference divided
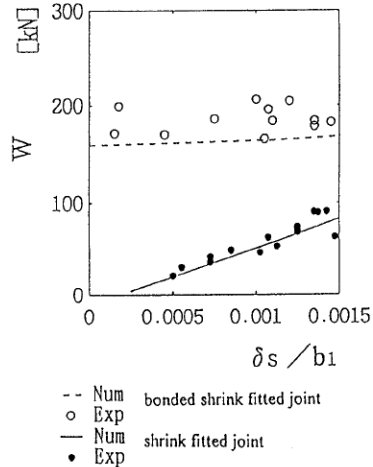
Figure 2.6: Comparison between experimental and numerical results of push-off force of shrink fitted joint and bonded shrink fitted joint [16].

by the outer radius of the shaft) with respect to the non bonded samples. In this case seems that the two contributions can not be considered independently.

Dragoni and Mauri conducted various experiments on tightened joints bonded with anaerobic adhesives [10, 13, 53]. On the basis of the results of these experiments, they develop a micro-mechanical model to describe the friction and the adhesive contributions to the overall strength of the friction bonded interfaces. The model mainly explains the different mechanical behavior obtained by using two different anaerobic adhesives in a friction interface. While the total strength of the joints bonded with a strong anaerobic adhesive could be predicted with the theory of the superposition of the effects, it was found that the same theory fails to predict the cumulative strength of the joints bonded with a weak anaerobic adhesive. The proposed model is illustrated in figure 2.7.

Real substrates are not perfect smooth, but characterized by a certain degree of roughness. The model assumed that in the presence of a contact pressure between the two real substrates, only a small portion of the nominal contact area is in a real contact condition due to the peaks and valleys of the surface at microscopic level. The adhesive is able to fills the surface valleys due to the roughness, where it receives no pressure. At the same time, the adhesive
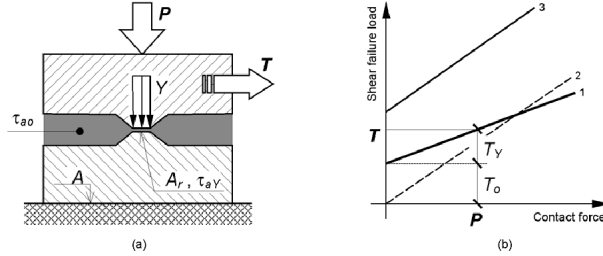
Figure 2.7: (a) Micromechanical model of the hybrid interface and (b) typical predictions for its macroscopic shear strength (curve 1 is related to the weaker anaerobic adhesive hybrid condition, curve 2 to the unbonded condition, curve 3 to the stronger anaerobic adhesive hybrid condition) [53].

forms a thin layer between the crests of the roughness, where it is subjected to a yield pressure, Y. According to the model τ_{a0} is the unit shear strength of the adhesive at zero pressure meanwhile τ_{aY} is the shear strength of the adhesive when subjected to the pressure Y. This two conditions coexist along the coupling area, A, and their influence varies on the basis of the real contact profile. The Authors assumed that regardless the roughness of the two surfaces, the real contact area that originates between the surface crests, A_r is a function of the pressure between the component P and the yield pressure Y of the softest adherend. In this condition the total resistance of the hybrid joint T could be predicted by the equation 2.5 [53]:

$$T = \tau_{a0}A + (\tau_{aY} - \tau_{a0})P/Y \qquad (2.5)$$

In the case of not bonded joint, τ_{a0} is equal to 0 as no adhesive is employed, and τ_{aY} correspond to τ_Y, the shear strength of the metal junctions due to friction forces. Thus, for only interference contribution, the equation 2.5 became $T = (\tau_Y)P/Y$. Therefore the equation 2.5 is composed by two elements: the first $\tau_{a0}A$ is a constant term dependent only on the employed adhesive, the second $(\tau_{aY} - \tau_{a0})P/Y$ is a variable term proportional to the contact force. The attainable strength of the adhesive film τ_{aY} under the high local pressure Y varies with respect to the adhesive used. Accordingly, the lower the strength of the adhesive employed τ_{a0}, the lower would be its strength under the yield pressure τ_{aY} and the lower would also be the slope $(\tau_{aY} - \tau_{a0})/Y$ of the hybrid joint resistance in response to the pressure between the substrates. In figure

2.7b the curve of the weaker adhesive (curve 1) has a lower slope with respect to the curve of the stronger adhesive (curve 3). The latter, on the other hand, seems to avail the theory of the superposition of the effects because it shows the same slope of the curve of the unbonded samples (curve 2).

Recently Castagnetti developed a FEM model on the basis of the Dragoni and Mauri analytical model [14], and asses it with an experimental campaign conducted on two types of acrylic anaerobic and different contact pressures [54].

Croccolo et al. [15,55] compared interference-fit hybrid joints made by steel hubs and shafts to mixed material hybrid joint made by aluminum shafts and steel hubs by following the superposition of the effects approach. They found that the adhesive contribution in aluminum-steel joint is poor because of the weak bonding forces between aluminum and adhesive, while the total strength of the aluminum-steel hybrid joint is similar to the steel-steel one. According to the theory of superposition of the effects, in aluminum-steel configuration the Authors stated the presence of an higher friction coefficient balancing lower static adhesive strength, as can be seen in figure 2.8.
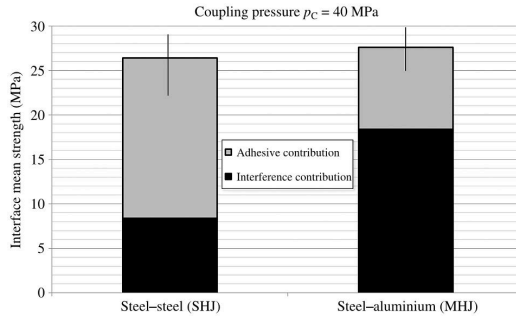
Figure 2.8: Comparison of total interface mean strength between steel-steel and steel-aluminum hybrid joint: interference contribution $(P\mu)$ and adhesive contribution (τ_a) are highlighted [15,55].

For what concern the type of adhesive, Mengel et al. [19] studied the mechanical behavior of an anaerobic acrylic and an epoxy adhesive on hub/shaft joints characterized by two combinations of adherent materials (steel-aluminum and steel-magnesium alloy) that were bonded under hydrostatic pressure. They found that the increase in hydrostatic pressure during curing implies an increase in the bond strength under quasi-statical as well as under fatigue loading for

both the adhesives used. Oinonen and Marquis [20] exploited an high modulus epoxy adhesive in mechanically clamped steel interfaces. They studied the effect of the surface roughness and clamping loads finding that for each of the three surface finishes tested, the shear strength of the bonded and non-bonded interfaces increased at a near constant rate with clamping pressure, as reported in figure 2.9. Therefore, the principle of superposition of the effects seemed to be applicable not only to the strong resistance anaerobic adhesive but also to the high modulus epoxy one. They also developed a model to evaluate the shear damage evolution of the hybrid joint confirming that the normal pressure acting on the hybrid interface provided a strong influence in dissipating the fracture energy [56].
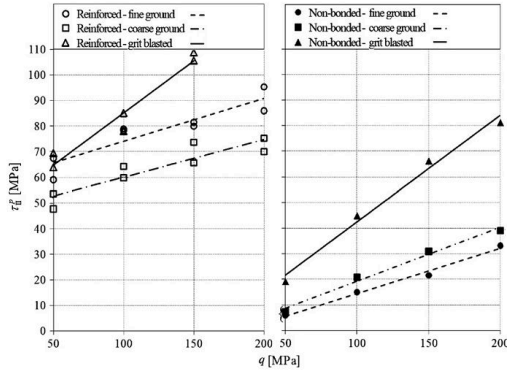
Figure 2.9: Peak values of the measured interface shear stress τ_{II}^p against the clamping pressure q are shown for the different surface finishes of the bonded and unbonded interfaces [20].

Sekercioglu [18,57] studied the interference-fit hybrid joints bonded with an anaerobic adhesive loaded in static and dynamic conditions examining the effect of parameters such as the interference or the clearance level and the surface roughness. For what concern the interference, as expected, the increase in the pressure between the components implied an increase in the performance of the joint. But it was noticed a decrease of this increment at higher interference levels, as can be seen in figure 2.10a.

For what concern the surface roughness, despite the evidence of a certain effect due to the surface finishing reported by Oinonen and Marquis [20] (see figure 2.9), a smooth effect of the parameter R_a to the final performance of
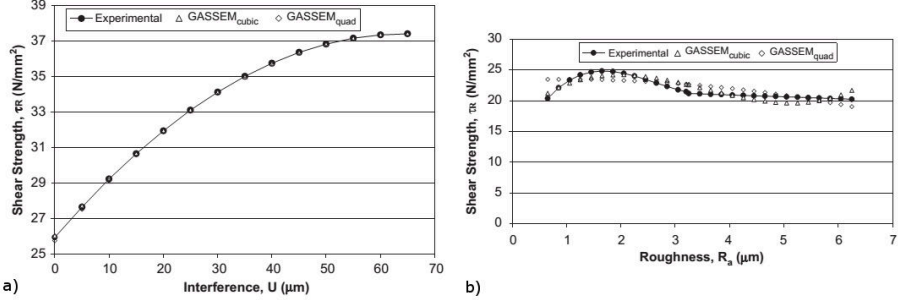
Figure 2.10: Comparison of the experimental and numerical results based on the effect of interference (a) and surface roughness (b) on the shear strength of the hybrid joint [57]

the hybrid joint was found in Sekergioglu experiment [57], as can be observed in figure 2.10b. This moderate effect of the roughness was also confirmed by Castagnetti et al. [14].

The fatigue resistance of the hybrid joint bonded with acrylic adhesive was investigated by different authors [15, 18, 19, 55, 58]. Sekercioglu et al. [18] and Mengel et al. [19] reported that the dynamic strength of hybrid joints increased as the interference value increased, as it happens for the static strength. Dragoni et al. [58] confirmed this evidence and reported that the hybrid joints subjected to fatigue exhibited a decay in strength with respect to their resistance to static loading. This decay seems to be referred to the adhesive contribution rather than the interference contribution. Indeed, they observed that the strength decay of the hybrid joints subjected to fatigue loading seems to be independent (in absolute terms) to the contact pressure. Moreover, the strength decay of the unbonded interference joint subjected to fatigue cycles appears to be negligible.

Croccolo et al. [15, 55] compared the fatigue behavior of steel/steel and steel/aluminum hub-shaft samples. Despite the different adhesion properties on the two exploited materials, they found a similar fatigue behavior for the two hybrid joints. The Authors performed tension–tension fatigue tests where the specimens were loaded with different force amplitudes: in particular, the minimum force was set equal to the calculated interference contribution, the maximum one equal to a percentage of the estimated static contribution of the adhesive. They found that the residual strength of the hybrid joints progressively decreased as a function of the load amplitude, in both the material

combinations studied. An example of this decreasing is shown in figure 2.11.
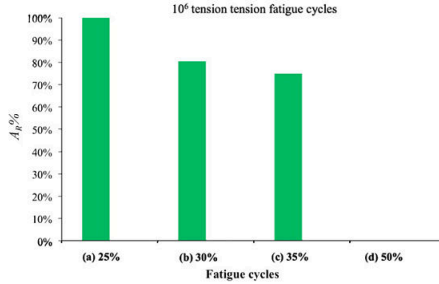
Figure 2.11: Adhesive residual strength as a function of the different fatigue cycles in steel–steel couplings [15]

The quantity of parameters that could influence the performance of this hybrid joint technique emerges clearly from the literature review presented in this section. The theory of the superposition of the effects seems to be a valuable and simple method to predict the total resistance of the hybrid joint, but it was demonstrated its inefficacy in various situations. For example, the employed type of adhesive could change the final behavior of the hybrid joint.

The effect of the adhesive nature and therefore of its mechanical and adhesive responses and the curing technology on the performances of the interference joints is still unclear. The acrylic anaerobics are the most studied adhesive system in this field. Their curing technology is convenient for their application in closed interference-fitted interfaces, (for further information about anaerobic polymerization see section 4.1), but in certain particular industrial applications other curing technologies could be more appropriate, especially when clearance zones are included in the joint design or different mechanical properties have to be matched.

Moreover the press-fit technique introduces important variables such as the coupling pressure, the spillage of the adhesive and the friction phenomena, involving parameters related to the rheology and tribology rarely investigated in literature. Further studies of the phenomena which occur at the interface level would be useful for the design of particular components that involve this hybrid joint technique.

Chapter 3

Methodology

Abstract

   As stated in the previous chapters, the strength of the joint is also dependent on the joint geometry and the resultant stress distribution in it. Testing the behavior of different adhesives and the effect of the interference contribution directly on the wheel would be an ideal solution, but could induce long testing times and uncertain outputs. The chapter describes the strategies for testing adhesive joints at laboratory scale. These solutions allow to detect the in-joint adhesive mechanical properties in certain particular controlled conditions. On the basis of literature the techniques employed to study the interference and adhesive contribution in the hybrid bonded-interference fitted joint are reviewed. In the second part of the chapter the chosen methodology is discussed in detail. Experiments were conducted at the laboratory level and then validated on the wheel system. Some consideration on the set-up of the applied tests are also reported.

3.1   Mechanical testing adhesive joints

The mechanical characterization of an adhesive joint is not a simple issue. As stated in the previous chapters, the measured strengths of a general joint depend not only on the degree of intrinsic adhesion achieved, but also on the mechanical properties of the adhesive material and of the substrates, as well as on the specific geometry of the joint, and on how the stresses are distributed inside it.

3.1.1   The mechanical properties of the adhesives

In material science, in order to mechanically characterize a material, its engineering properties have to be known. Typically the main properties required are the tensile, or Young's modulus (E), the shear modulus (G), the yield stresses, the fracture stresses and strains in uniaxial tension and in pure shear. Usually these properties are easily measurable in bulk specimens [59].

The same approach can be exploited in adhesive science. Bulk specimens of the adhesive material can be prepared and mechanically tested. The mechanical tests performed on bulk adhesive material specimens can provide useful information on the cohesive properties of the adhesives. Notwithstanding this, in order to study also its adhesive properties and its mechanical behavior in a joint, tests on the joint system have to be performed [8]. Testing adhesives in bulk material specimen could present also some issues that have to be taken into account. Indeed it is not clear if mechanical properties of a bulk adhesive material could differ from the properties of the same adhesive hardened '*in-joint*' [8,60]. In common joint systems the adhesive is applied as a liquid on the substrates and it hardens directly forming a thin layer between the two adherends. The presence of the substrates might alter the kinetics of the chemical reactions by which the adhesive hardens, and thus altering the final mechanical properties of the adhesive itself. For instance, the acrylic anaerobic curing technology is widely affected by the types of substrates to be bonded [61]. However, there are some evidences of similar results obtained in detecting the Young's modulus of an adhesive between '*in-joint*' configurations and '*bulk*' specimens [60]. Anyway, the mechanical properties obtained by exploiting bulk materials, could be a useful and easy approach to understand the general mechanical behavior of an adhesive. Whether or not they may be used in the design and analysis of adhesive joints, no information on adhesion properties and its behavior under particular stress loading could be obtained [8,60].

3.1.2   Testing the joints

A second characterization approach is to study the mechanical properties of the adhesive directly in the joint. This approach is less fast and easy with respect to the testing bulk specimens, but it permits to study the effective mechanical properties of the adhesive in the proper conditions [8]. The ideal case would be to test the adhesive directly in the final application or in a representative sample of it [7]. In the case of complicated joint geometry and loads, the testing of representative prototypes for each candidate adhesive and surface treatments

would be too expensive [7]. Different organizations such as the International Standards Organization (ISO), Europe Standards (EN), American Society for Testing and Materials (ASTM) developed a series of standard tests characterized by joint geometries designed to have an ideally and known stress distribution in order to detect the in-joint adhesive mechanical properties. Thus the solution is to select and apply the appropriate standard tests and to know what the result means in terms of the final application [7].

Table 3.1: Common standard test method for adhesive joint [7, 8, 22, 24, 60, 62]

Standard	Joint geometry	Comments
Single lap shear test ASTM D-1002 [63]		Simple test commonly used to compare the apparent shear strength. The same joint geometry can be used to investigate creep (ASTM D-1780) and fatigue (ASTM D-3166).
Thick adherend lap shear test ASTM D-5656 [64]		Shear stress-strain curve and mechanical shear properties of the adhesive could be determined.
Impact resistance test ASTM D-950 [65]		This test method can be used to compare the sensitivity of various adhesives to suddenly applied loads. It uses a block shear joint.
Double cantilever beam test ASTM D-3433 [66]		Test methods to determine the fracture strength in cleavage of adhesives. The fracture toughness can be calculated in proper test conditions.
'Boeing' wedge test ASTM D-3762 [67]		

'T' peel test ASTM D-1876 [68]		Test geometries for the determination of the resistance to peeling stress with two flexible substrate ('T' peel test) and a flexible and a rigid substrate (90° peel test).
90° Peel Resistance ASTM D-6862 [69]		
Pin and collar test ASTM D-4562 [70]		This test method can be used to determine the shear strength of adhesives used for retaining cylindrical assemblies. It is usually exploited for testing anaerobic adhesives.
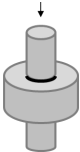
The American Society for Testing and Materials (ASTM) issues a very extensive list of standard tests for assessing the performances of adhesive joints. These test methods are the most commonly used by adhesive technologists to test adhesive joints in specific loading conditions [7, 8]. As stated in Chapter 1, the adhesive strength varies considerably with the joint geometry and the test conditions, so it is very important to define standard procedures. Some most used ASTM standard test methods are reported in table 3.1, with comments regarding the specific investigated condition [7, 8, 22, 24, 60, 62].

The pin and collar test method employs a joint geometry based on two cylindrical components. According to the standards ASTM D4562 [70] and EN 15337 [71] the pin and collar method is created with the purpose of testing anaerobic adhesive, the fairly more used type of adhesive in cylindrical components [62] (more information on the anaerobic adhesives can be found in section 4.1). Both the standards set a slight gap between the pin and the collar, generating a slip-fit condition.

3.1.3 Fractografic analysis

A potentially valuable tool for the post-test characterization of failures is fractography: the study of fracture surface topography [72]. Fractography is based

on the processes of observing, describing and interpreting a fracture surface and it involves microscopy in all its form [72]. In adhesion science fractographic analysis is used to discriminate the type of fracture such as adhesive/interfacial, cohesive, or mixed [6, 8]. Cohesive failures in the adhesive layer is an indication of a good adhesision between the adhesive and the substrate (see Chapter 1). Adhesive failure provides information on bad adhesion, and could be improved by selecting an adhesive with better wettability on the substrate or by considering a surface pretreatment on the adherend [6, 8].

The analyst could also consider the identification of the fracture origin (crack initiation, defects), the direction and pattern of crack propagation that is related to the energetic aspects of the fracture (single event or fatigue; brittle or ductile) [73]. The fracture energy and the type of crack propagation are also functions of the test temperature and rate [8]. At higher test temperatures, the yield stress of the adhesive is lower leading to instable or more ductile fractures. On the other hand, more brittle propagation patterns are observed at lower temperatures. The test rate influences the crack propagation in the opposite manner: higher test rates correspond to more brittle crack growth, lower test rates lead to more ductile propagation.

3.1.4 Test methods for the hybrid interference fit adhesive joint

There are no standard tests available for testing the hybrid adhesive bonded - interference fitted joints. Different strategies had been employed in literature to fulfill this purpose.

A method usually exploited in literature [15, 16, 48, 52, 53, 55, 58, 74] is based on the pillar and collar joint geometry described in table 3.1 . In this case the shaft diameter is bigger than the ring one in order to create the fitting force. Both shrink-fit and press-fit assembly techniques can be exploited for the sample preparation. The assembled joints could be tested with axial loads in traction or compression and with torsional loads.

Another method is based on hub/shaft joint geometry depicted in figure 3.1. This joint is similar to the pin and collar one, but in this case the shaft is not passing through a ring, but is inserted in a closed hub. Also in this case, the two components could be assembled using press-fit or shrink fit [18]. Mengel et al. [19] exploited an injection system based on hydrostatic pressure for curing the adhesive under pressure inside the hub/shaft joint without using any press-fit or shrink-fit. Torsion, compression and traction tests can be easily performed by holding the extremities of hub and shaft.
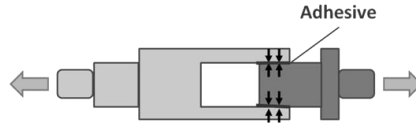
Figure 3.1: Schematic representation of the hybrid interference-fit joint in a hub/shaft joint geometry.

Another solution widely utilized in literature is to exploit torsional tests on clamped interferences [13,16,17,20,52–54]. The samples can differ by flanges [16, 17,20,52], tubular joint [54] or annular bushings [13,53], on which both an axial load and a torsional load can be applied by a test machine. In this configuration the axial load permits to precisely control the contact pressure between the components that in the other test methods is a result of the interference and thus subjected to machining errors. Then a torsional load is applied to the interface while the axial load is maintained constant. An example of this solution is showed in figure 3.2.
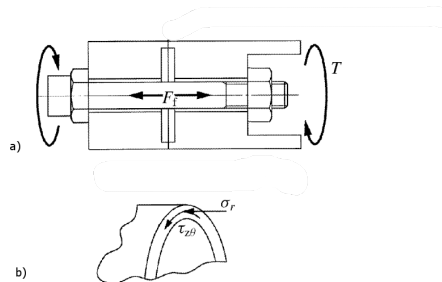
Figure 3.2: Schematic representation of the analogous test used for controlling the clamping force in clamped-bonded interfaces in Sawa et al. experiments [17]: a) testing scheme b) loads on the circumferential bonded area

3.2 Test methodology employed

The wheel has a complex design, where many variables can affect its structural behavior. Testing the behavior of different adhesives and the effect of the inter-

ference contribution directly on the component could induce long testing times and uncertain outputs. For instance, the interference level in the wheel is not univocal, during the press-fit the rim plastically deforms and the disc flange is inclined by a flange angle, thus the radial contact pressure due to the interference is not constant along the joint area and difficult to estimate. On the contrary, laboratory samples can be created in order to evaluate the different parameters. Obviously laboratory samples should be a simplification of the wheel system, and they could not simulate exactly what happen in the wheel, but they can provide precious information on the interaction between the different parameters involved in the hybrid joints.

In order to test the behavior of different adhesive systems in the hybrid joint, and to analyze the influence of the interference contribution on the chosen adhesive, laboratory samples were created. Among the main test methods identified in literature to study the interference-fit hybrid joints (see section 3.1.4), the hub/shaft joint geometry was chosen being the most suitable for the available test machines. The interference levels of laboratory samples were controlled by the tolerance dimensions of hubs and shafts and the press-fit technique was employed for assembling the components. The details and the assessment of the test method are described in the following sections.

3.2.1 Samples design and characterization

The hollow tubes and the shafts were designed according to the requirements imposed by our traction and fatigue test machines. The technical drawings of the hollow tubes and shafts are illustrated in figure 3.3.
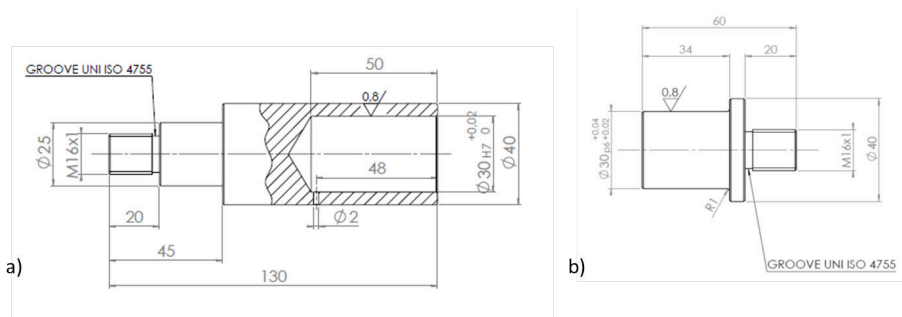
Figure 3.3: Dimensions in mm and tolerances of the specimens: a) hollow tube, b) shaft [75]

The coupling diameter of the samples was set to 30 mm. This represented a versatile value that facilitated a minimum extent of thermal expansion in the case of performing either the press-fit or the shrink-fit assembling techniques. The threaded extremities of the samples were designed to be correctly hitched to the fatigue test machine. Working at the resonance frequency, the threaded grabber is necessary to block the samples avoiding slipping effects. The head of the shaft was designed with a diameter of 40 mm after the threaded tip. This part had the same diameter than the external part of the hub and this allowed the alignment of the components during the press coupling. A coupling length of 10 mm was fixed. After the evidence of the first experimental campaign described in Chapter 4, a hole was opened on the side of the hub to prevent the formation of compressed air inside the joint. More consideration on this aspect are discussed at the end of section 4.5.

The laboratory samples where machined in C40 steel by the company C.M.S. Special Mechanical Construction of Torino. A picture of the components machined is reported in figure 3.4.

Figure 3.4: A hub and shaft. [76]

The coupling diameters of each hub and shaft were checked along four sections in the first 10 mm (the coupled length) with a Trimos horizontal measuring and calibration instrument. Then, an average diameter was calculated for each component. The mean diameters of hubs and shafts were listed in order to select the best coupling pairs to obtain the desired interference level. The considered interference for each specimen is calculated as the difference of the mean diameters of the related hub and shaft. Thus the error on the interference is based on eight measurements (four for the hub and four for the shaft).

The roughness of the samples in terms of R_a and R_z was also checked with a

rugosimeter. Two linear sections of 8 mm of length were checked for each hubs and shafts. Then mean R_a and R_z values for each specimen were calculated.

3.2.2   Assembly methodology

Before the assembling operations, the joint area of hubs and shaft was cleaned. The same surface preparation was followed for every samples both bonded and not-bonded. The surfaces were cleaned with acetone, dipped in acetone and placed in an ultrasonic bath for 5 minutes.

   The hub/shaft joints were assembled according to the press-fit method, as it would happen in the wheel system. This method introduces several problems concerning misalignments and the splitting away fo the adhesives, as described in section 2.3.1.

Figure 3.5: Schematic representation of the guides system exploited to guarantee the alignment of the joints. [76]

   The alignment between the shaft and the hub was a crucial parameter to obtain repeatable joints. A not-axial assembling induces far higher coupling and decoupling loads then an axial one. A method of guides, schematically illustrated in figure 3.5, was exploited to guarantee the alignment of the couples. During the press coupling operation, the samples (both hub and shaft) were not fastened but self-arranged into the guides. The method was validated by

examine the misalignments of a series of coupled specimens. The misalignment were estimated by putting in rotation the assembled joints and measuring the eccentricity between the hub and the shaft. Noticeable misalignment effects are avoided by means of the system of guides.

The pressing was performed by means of an automatic press in order to assure the same pressing rate for each sample.

The joint geometry surely implies the presence of spew fillets, being the shaft press-fitted into the hub. Two spew fillets appeared on both limits of the bonded area. The external spew fillet is visible after the coupling and it was removed before the adhesive cures. The internal one is observed after the breaking of the joint, but, the geometry of the sample makes impossible to remove it. According to the pin and collar test method, a cord shaped adhesive spew must remain in one of the collar ends, otherwise, enough adhesive must be applied to create it [62, 70]. The spew fillet aspect becomes relevant mainly comparing other adhesives to the anaerobic ones, as explained in section 4.3.

3.2.3   Considerations on the traction and fatigue tests

In order to understand the behavior of different adhesives and the extent of the interference contribution, the samples were tested under an axial pull-out load.

The traction test was carried out at a crosshead of 1.3 mm/min in quasi-static condition. Considering that for the employed test no standards are available, the crosshead speed was selected on the basis of the low load rate generally suggested in the standard shear tests on adhesive joints. The suggested crosshead speed for the pin-and-collar test was between 1 and 2 mm/min [62]. For what concern the single lap shear test a rate of loading of 80 to 100 Kg/cm^2/min is adviced, approximately equivalent to a crosshead speed of 1.3 mm/min [63]. The thick adherend lap shear test method recommends a rate of loading of 2455 N/min [64]. The load per unit area provided by a crosshead speed of 1.3 mm/min to an hybrid joint sample is compared in figure 3.6 to the recommended load rates of the single lap shear and the thick adherend lap shear tests.

Fatigue tests on hybrid joints were carried out on a resonant testing machine. The adopted approach was a tension-tension fatigue test, which implies a tensile cyclic loading.

Some considerations has to be done in respect of the tension-tension variable amplitudes employed. The minimum load amplitude was set constant for each sample, on the basis of the resistance provided by the interference contribution (F_{int}). The maximum amplitude was varied among a percentage of the static
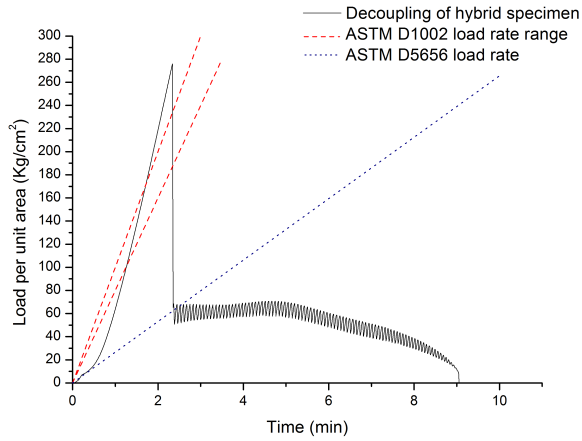
Figure 3.6: Load rate of decoupling test on hybrid joint at a crosshead speed of 1,3 mm/min, compared with the standard decoupling rate for the single lap shear and the thick adherend lap shear test
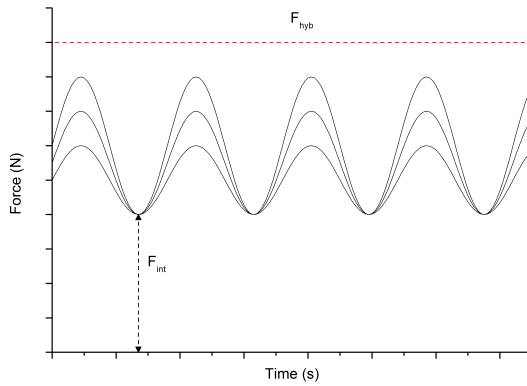

Figure 3.7: Schematic example of the load cycles employed in fatigue tests

total resistance of the hybrid joint (F_{hyb}). A schematic example of the fatigue cycles performed is presented in figure 3.7.

This approach is based on literature background. Dragoni et al. [58] showed that the strength decay of hybrid joints subjected to fatigue loading could be imputable to the adhesive contribution, meanwhile the non-bonded interface is virtually unaffected by a fatigue decay. Other researchers [15, 18] adopted a tension-tension fatigue test approach based on the standard ISO 9664 [77]. In particular Croccolo et al. [15] set the minimum amplitude force equal to the force provided by the interference contribution.

The load cycle frequency of the fatigue test is dependent on the typical frequency of the samples as the used fatigue machine operates in resonance frequency.

3.2.4   Tests for bonded wheel validation

The hybrid bonding technology studied at the laboratory scale was transferred on the wheel system. The wheel is a far more complicated system than the hub/shaft sample. The disc and the rim are plastically deformable, they have a relatively complex design and many variables can influence the structural resistance of the wheel.

Starting from the outcomes of the laboratory research, bonded wheel prototypes were created. Standard validation tests were carried out in MW in order to evaluate the feasibility of the hybrid joining technology in the wheel system. The objective of these tests were also to verify the importance on the wheel of the key parameters and the trends studied at the laboratory scale.

Chapter 4

The behavior of different adhesives in the hybrid joint

Abstract

Generally anaerobic acrylic adhesives, also known as "retaining compounds", are employed in interference-fitted cylindrical joints, being exploitable in this arrangement their curing technology based on a one component configuration. Nevertheless in certain particular industrial applications other curing technologies could be more appropriate, especially when clearance zones are included in the joint design or different mechanical properties have to be matched. The effect of the adhesive's chemical nature, curing technology and mechanical properties on the performance of the hybrid joint is still unclear. The work presented in this chapter aims to examine the behavior of different adhesives, including rigid epoxies and flexible polyurethanes, in the presence of an interference-fit. The static pull-out strength of bonded and unbonded interference fit joints and adhesive joints in clearance condition were compared and the advantages and disadvantages provided by different adhesives were pointed out.

65

4.1   The selection of the adhesives

The purpose of the study was to investigate the main families of structural
adhesive and consequently their typical mechanical properties and curing tech-
nologies in the hybrid joints. The choice of the proper adhesive is based on the
required parameters for the wheel application: high resistance on steel, high
durability and a wide range of operating temperatures to withstand different
outdoor climates.

The principal families of adhesive employed for structural purpose are based
on Epoxy, Acrylic or Polyurthane thermosetting resin systems [4, 6, 22]. The
different families of adhesives can be classified on the basis of the adhesion
strength that they provide against their flexibility. Generally rigid adhesives
provide high joint strengths and are selected for applications requiring high
shear resistance and low peel and impact strength. On the other hand, flexible
adhesives are characterized by a lower adhesion strength, but are suited for
joints loaded in peel or cleavage, or in presence of components vibrations, and
they usually provide good impact resistance. [6, 7] The positions of the main
families of adhesives in terms of joint strength and flexibility are illustrated in
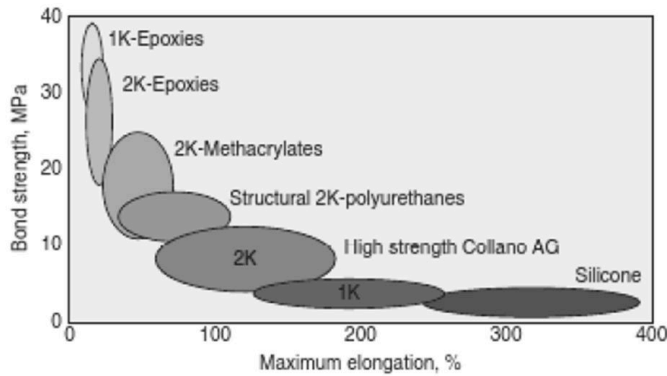figure 4.1.

Figure 4.1: Comparison among the main families of adhesives in terms of their
joint resistance and their flexibility [6]

A brief description of the investigated adhesives is given in the following
paragraphs. The technical data-sheets of the adhesives used are reported in the
Appendix B.

4.1.1   Epoxy resins

Epoxy resins occupy a dominant role in the field of structural adhesives for their excellent wettability on different substrates, excellent mechanical properties, resistance to high temperatures and high chemical inertia [6]. They have, however, two major drawbacks: once crosslinked they are brittle and therefore they have a low impact resistance. In addition, they have durability problems in wet environments due to water absorption [6–8]. To overcome these two major problems it is possible to change the structure of the adhesive material with the addition of additives and to pre-treat in some way the surface to be joined. Several studies described new formulations of epoxy resins, because they are the most versatile system to be modified by additives [6, 78–84]

The most common technique to crosslink the epoxy resin is a chemical reaction between a prepolymer system and an organic substance called hardener [8, 22]. Often the reaction is assisted by heating, and the heating time and temperature, strictly related to the specific system, are crucial parameters to achieve the optimum crosslinking. The most common hardeners for crosslinking epoxy resins are aliphatic or aromatic amines and anhydrides [6]. In figure 4.2 is schematized the hardening reaction of an epoxy resin with a primary amine, in which the epoxy ring reacts with the amino group and gives rise to a crosslinked structure.
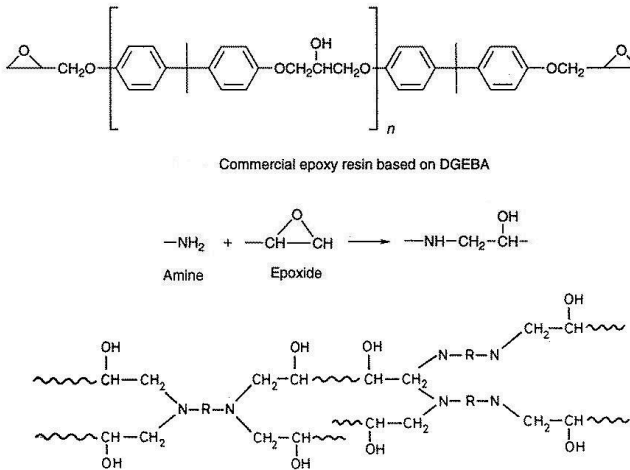

Figure 4.2: Reaction between a primary amine and an epoxy resin [22]

In this study two epoxy adhesives were investigated:

- A rigid epoxy adhesive: Hysol[R] 9492. This is an Henkel *2k* structural epoxy adhesive with an high resistance (Bulk tensile strength = 31 MPa), but with a low flexibility and peel resistance (Elongation at break = 0.8 % and Peel strength = 1.6 N/mm) [85]. It will be referred as "*R-EP*" in the text.

- A flexibilized and toughened epoxy adhesive: Scotch-weld[R] DP490. This is a 3M *2k* structural modified epoxy adhesive with high resistance (Shear on grit blasted steel = 28.7 MPa) and high peel resistance (Peel strength = 9,2 N/mm) [86]. It will be referred as "*FT-EP*" in the text.

4.1.2 Acrylic anaerobics

Acrylics are a large family of adhesives based on the acrylic functional group, schematically shown in figure 4.3.

Figure 4.3: Acrylic functional group where R1 and R2 represent various organic groups [6]

The family of acrylics is very wide and the curing of the adhesive can greatly vary, from the cyanoacrylates that are able to harden reacting with the humidity to the two components systems. Generally, the most used acrylic adhesives in cylindrical joints are the anaerobic adhesives [10–12]. They are employed as blockers and sealants because they are single-component adhesives able to cure at room temperature and in the absence of oxygen activated by the contact with metal surfaces [49]. The single-component adhesive is formed by the prepolymer, usually an ester methacrylate, and the initiator ,commonly an organic hydroperoxide. Hydroperoxides are highly reducible species in the presence of metal ions, usually present on many metal surfaces. The resultant electron transfer reaction leads to the formation of a radical $(RO°)$ that attacks the acrylic monomer initiating in this way the polymerization [6, 22, 61, 87], as schematically shown in figure 4.4.

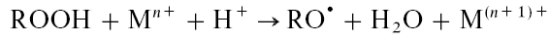$$ROOH + M^{n+} + H^+ \rightarrow RO^\bullet + H_2O + M^{(n+1)+}$$

Figure 4.4: Schematic diagram of the reaction between a hydroperoxide and a metal ion. [61]

This reaction takes place only in the absence of oxygen and for this reason it is defined anaerobic. The oxygen acts as an inhibitor because it reacts with the radical blocking the reaction [6, 22, 61, 87]. This type of adhesive is very attractive for industrial application: the storage of the adhesive takes place in open air and cross-linking occurs in closed interfaces with at least one surface containing metal ions. The disadvantage of this technique is that not all the surfaces contain metal ion activators. Generally metals are considered active surfaces, but with different reaction rates [61, 87]. In the case of non-active surfaces, it is possible to exploit activator systems able to spread active metal ions on the surface to be bonded.

The anaerobic acrylic adhesive tested in this study is the Loctite® 620, an Henkel high resistant anaerobic adhesive (Shear on steel = 17.2 MPa) designed to withstand high temperature range [88]. It will be referred as "AC" in the text.

4.1.3 Modified polyurethanes

Polyurethanes are resins derived from a pre-polymer isocyanate-urethane. In two component polyurethane adhesives, a polymer containing OH- groups (polyethers, aliphatic polyesters, polybutadiene) is mixed with an isocyanate [6] [22]. Any hydroxyl groups on the surfaces will possibly react with isocyanate to form co-valent bonds between adhesive and substrate [22]. One component formulation that reacts with the atmospheric humidity are also available [22, 89]. The characteristic functional group of the polyurethanes is schematically shown in figure 4.5.
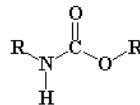

Figure 4.5: Urethane molecular structure where R represent various organic groups [6]

Polyurethanes are segmented polymers characterized by a two-phase microstructure mutually incompatible. The hard and rigid segments of the chains form a glassy or semi- crystalline phase, instead the flexible segments of the chains form an amorphous and rubbery matrix that surrounds the rigid phase. Thus, the cross-linked adhesive does not present a perfectly rigid behavior but is also characterized by low T_g and flexibility. These adhesives make the joints able to withstand vibration and oscillatory loads. The polyurethanes can be mixed with epoxy adhesives to obtain blends with mixed properties. Because of their property of absorbing the energy of an impact load, modified polyurethanes are attractive for automotive applications where they are known as *crash resistant adhesive* [4, 6].

The polyurethane adhesive tested in this study is the Araldite$^{®}$ 2029. It is a modified polyurethane adhesive by Huntsman that provides characteristics of both resistance (Shear on grit blasted steel = 24 MPa) and flexibility (Elongation at break = 39 %) [90]. It will be referred as "PU" in the text.

4.2   The design of the experiment

The role of the different adhesives in the interference fit joints was studied in a hub/shaft geometry. The hub/shaft samples were assembled as described in Chapter 3. The samples were tested under a static axial pull-out load, performed through a traction test using a MTS test machine with a cross-head rate of 1,3 mm/min (for further information see section 3.2.3).

It was decided to prepare a series of samples with an interference coupling of 20 μm, according to H7/p6 ISO standard of tolerance, and a series with a clearance coupling of about 40 μm according to a coupling tolerance of H7/f7 (for further information about ISO standards of fit and tolerance see Chapter 2). The four commercial adhesives based on different structural adhesive systems were tested. The traction tests were carried out on samples joined with the interference only, samples bonded with the four different adhesives in clearance conditions, and hybrid joints interference-fitted and bonded. The experimental design is resumed in table 4.1. For each of the above-described case studies, 4 samples were tested.

The same surface preparation was followed for every sample. The surfaces of hubs and shafts were cleaned with acetone, dipped in acetone and put in an ultrasonic bath for 5 minutes.

According to the producer suggestions [85, 86, 88, 90], the following curing protocols were applied:

Table 4.1: Design of the experiment

Adhesives	Interference levels	
	interference ISO H7/p6	Clearance ISO H7/f7
No adhesive	4 samples	/
Rigid epoxy	4 samples	4 samples
Flexibilized and thoughened epoxy	4 samples	4 samples
Acrilic anaerobic	4 samples	4 samples
Modified polyurethane	4 samples	4 samples

- *R-EP*: 72 hours at room temperature;

- *FT-EP*: 24 hours at room temperature followed by a post-curing at 80 °C for 1.5 hours;

- *AC*: 72 hours at room temperature;

- *PU*: 16 hours at 40 °C.

Particular attention was paid to the heat curing systems as the thermal extension of the adherends during heat curing and the adhesive shrinkage could result in residual stresses in the joint. In this experiments the epoxy *FT-EP* samples were exposed to a post curing treatment at 80 °C and the *PU* samples were cured at 40 °C. The hub and the shaft have a nominal diameter of 30 mm, thus, assuming a generic thermal expansion coefficient of $11 \cdot E^{-06}$ for carbon steel, their linear thermal expansion provided by the heating from room temperature to 80 °C is around 18 μm whereas a value of about 5 μm was calculated for the samples heated from 25 to 40 °C. It is important to underline that these values concern both the hub and the shaft, being both made of the same material. It is then reasonable that during heating the interference or clearance between the two components remains the same, as both diameters change of the same extent. On the other hand the circumference of the coupling area changes due to the expansion of the components. An increase of around 57 μm at 80 °C, and of 16 μm at 40 °C is estimated for a circumference nominal length of 95 mm. On the basis of these values, the dimensional modifications can be considered negligible. Secondly, for what concern the shrinkage of the adhesive, it is important to consider that the curing protocol followed for all the employed adhesives is suggested by the corresponding producers as the conditions to reach

the best adhesive strength. The curing technology is fundamental to compare the different systems, and the evaluation should take into account its positive or negative effects on the final performances of the hybrid joint.

4.3   Decoupling behaviors

The decoupling load/displacement curves of the different hybrid systems and the unbonded interference samples are reported in figure 4.6. For each case study the four decoupling curves were averaged for obtaining a representative mean curve, also applying a smoothing filter. The mean load/displacement curves were compared in figure 4.6.

The decoupling curves of the unbonded interference samples were characterized by a first peak after the elastic region, that corresponds to the point in which the joint forces are broken and the shaft starts to move. After this point, that is considered the resistance of the joint, a quite constant load was recorded, and the curves were characterized by a sinusoidal trend. It is reasonable to assume that the low speed of testing, chosen to evaluate the adhesive behavior in the hybrid joints, induced a discontinuous decoupling in the unbonded interference-fit condition, with consecutive stick–slip states. According to Bowden and Tabor [91] the intermitted motion depends on the fact that the static friction is often higher than the kinetic friction: the '*stick*' is due to the higher static friction between the surfaces, and the '*slip*' to the lower kinetic friction due to the slip itself. This behavior is profoundly affected by the speed of sliding. Indeed, as the speed increases, the two friction coefficients at the *stick* and during the *slip* become more nearly equal, with a corresponding decrease in the magnitude of the fluctuations. At a critical speed the difference between the two friction coefficients disappears and the motion is relatively smooth.

When different adhesives are employed, differences in the mechanical behavior can be observed, as highlighted in figure 4.6. The curves of the *R-EP*, *FT-EP* and *PU* two-component adhesives were characterized by two main phases: an initial load peak and a following additional load recording with the stick/slip trend typical of the interference contribution. The initial peak was due to the contribution of the adhesive plus the interference. The adhesive break up point occurred in correspondence with the maximum of the peak. After the adhesive failure, in order to complete the decoupling, an additional load is necessary to exceed the interference contribution. In the cases of the two epoxy systems, the drastic failure of the adhesive induced a recoil in the test machine that recorded load values close to zero. After that the interference contribution resistance was
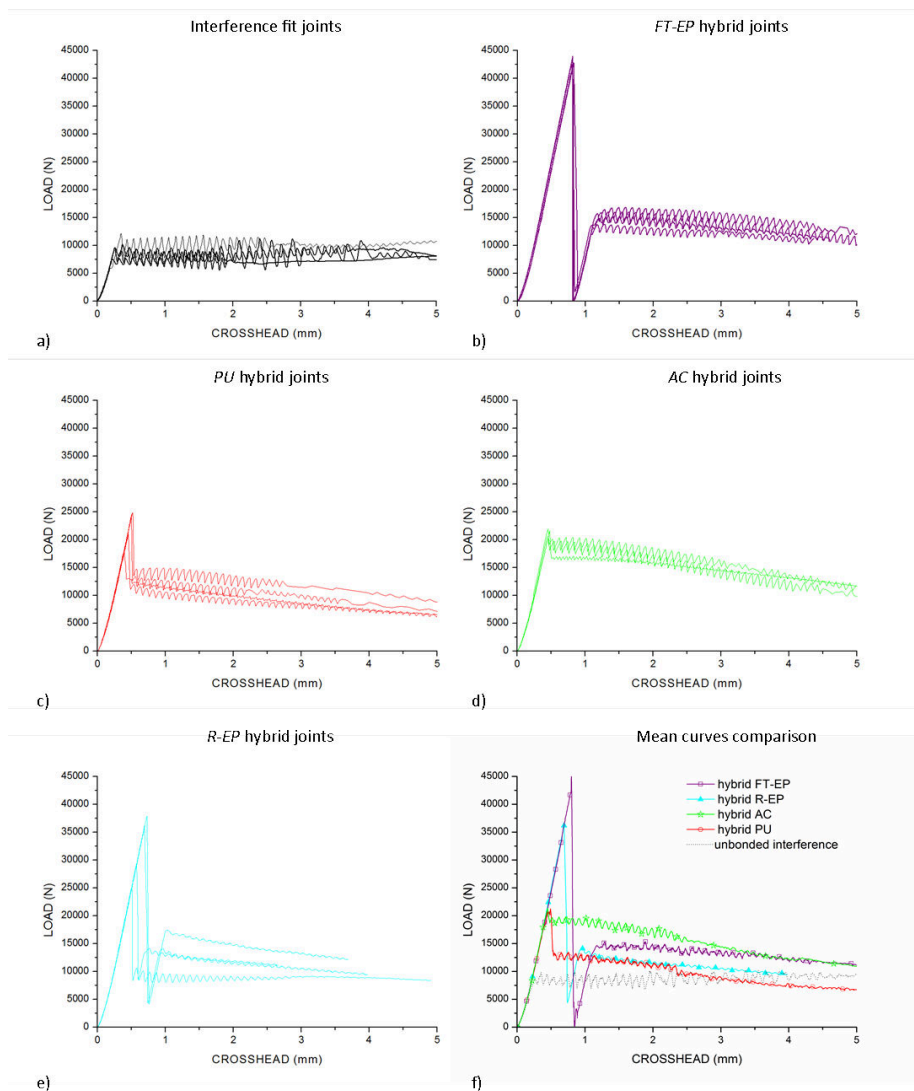
Figure 4.6: Load/displacement curves: a) unbonded interference-fit joints, b) *FT-EP* hybrid joints, c) *PU* hybrid joints, d) *AC* hybrid joints, e) *R-EP* hybrid joints, f) Comparison among the mean curves of all the interference systems [76]

recorded.

The decoupling curves of the AC samples presented some differences from the other ones: they were characterized by a lower adhesive failure peak and an higher interference contribution. This force trend without the drastic failure of the adhesive has been already observed by Croccolo et al. [15] using anaerobic acrylics on steel substrates. It seemed that the different type of curing mechanism induces an enhancement of the friction forces in the contact zone heightening the interference contribution and implying a less drastic crash of the adhesive. Another hypothesis could be related to the absence, in these joints, of a cured spew fillet. Indeed in these anaerobic systems, the spew fillets that generally is formed on both limits of the bonded area were not able to harden, because the oxygen inhibited the polymerization. Thus the additional resistance provided by this cured adhesive material at the end of the joint is absent in the anaerobic samples (for further information about the spew fillet see Chapter 3).

The fracture surfaces of every hub and shaft was checked after the decoupling: different examples of the shaft fracture surfaces are depicted in figure 4.7. The shafts and the hubs presented in the majority of cases some cured adhesive residues on the mating surface. In the case of FT-EP, AC and PU samples, the cured residues was present in a similar morphology on both the hubs and the shafts. Some examples of the cured residues of three shafts bonded with the three adhesive systems are shown in figure 4.7a, 4.7b and 4.7c. It is difficult to define if a cohesive fracture took place because a very thin layer of adhesive remained inside the junction. The fracture is most likely a mixed mode between adhesive and cohesive types.

On the contrary, as reported in figure 4.7d and 4.7e, different residue quantities of R-EP remained on the shafts of the various samples. By analyzing the hub and the shaft samples it seemed that a different amount of adhesive spread inside the joint during press-fit, rather than a case of adhesive fracture on the shaft side. This fact implied a wider variability in the related load-displacement curves, as can be observed in figure 4.6e.

The spreading of the adhesive in an interference fit joints depends on the flow properties of the adhesive that are studied by rheology. For what concern the rheology of the adhesives tested in this work, the FT-EP, AC and PU were reported as thixotropic [49, 92, 93], whereas this characteristic was not declared from the supplier in the case of the R-EP adhesive [49].

Thixotropy defines the capacity of reversible solid-liquid transition: a *gel* that converts into a *sol* when a shear load is applied [94–96]. In adhesive science thixotropic adhesives are 'non-sag' pastes that lower their viscosity when subjected to mechanical stresses [6]. In a rest condition and under low shear forces
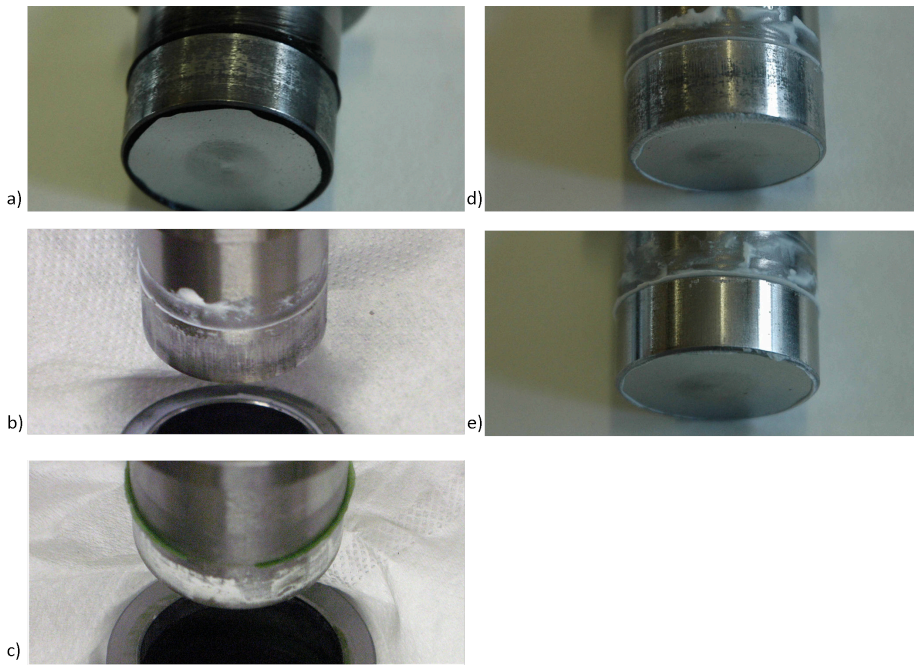
Figure 4.7: Fracture shaft surfaces of the decoupled joints: a) typical black layer of the cured *FT-EP* adhesive; b) typical white layer of the cured *AC* adhesive; c) typical grey residues of the cured *PU* adhesive; d) grey residues of the cured *R-EP* adhesive; e) *R-EP* sample where cured particles are not present on the mating surface.

the adhesive particles form a network structure that breaks down when a critical shear rate is reached [6]. In rheology, when the viscosity of a fluid decreases as an applied stress increases it is said that the fluid presents a 'pseudoplastic' behavior . Thixotropy differs from pseudoplasticity because the structural recovery from the sol state is not instantaneous, but it is subject to a hysteresis . Pseudoplastic fluids are not characterized by time-depending effects [94–96].

Generally a low viscosity is recommended in closer joints, while an high viscosity is preferable when a gap filling is required [49]. During the press-fit coupling considerable stresses were developed at the interface, therefore a thixotropic behavior could be advantageous. The *R-EP* adhesive, could be spewed away of the joint in a greater extent with respect to the thixotropic adhesives. Further studies have to be conducted to deeper analyze the relation between adhesive viscosity and its residual quantity in the junction.

4.3.1   Hybrid joints and adhesive bonded joints comparison

In order to better understand the behavior of the hybrid joints, their decoupling curves were compared with those of the corresponding bonded joints in clearance condition and the unbonded interference samples in figure 4.8. The reported curves are the mean load/displacement curves of the four samples for each of the three different cases (Bonded, Interference, Bonded+interference) related to the four adhesive systems. It is important to underline that the *R-EP* samples were affected by a higher variability of the results, as pointed out in the previous paragraph of this chapter. Thus, the algorithm employed to mean and smooth the curves did not allow to obtain a clear first peak shape. For this reason the mean maximum loads corresponding to the first peak were discussed later in paragraph4.5.

By comparison these curves, it was possible to observe that also in the case of the bonded joints in clearance condition, after the breakup of the adhesive, a residual load level is recorded (dashed orange curves). This load, probably due to the friction forces provided by the cured adhesive on the mating surface of the hub and the shaft, varied on the basis of the employed adhesive. Moreover, this residual load presented a different behavior with respect to the interference residual load in the hybrid joints (dotted blue curves), since it expired before the complete decoupling of the joint.

The load after break of the hybrid joint (dotted blue curves) was in any case slightly higher in value than the interference load recorded from the unbonded samples (black curve). The reason of this evidence could be imputable to the

fact that also in the hybrid joints cured adhesive particles were present between the two interference-fitted components. Therefore, the layer of the broken cured adhesive could have enhanced the pressure provided by the interference between the two components.
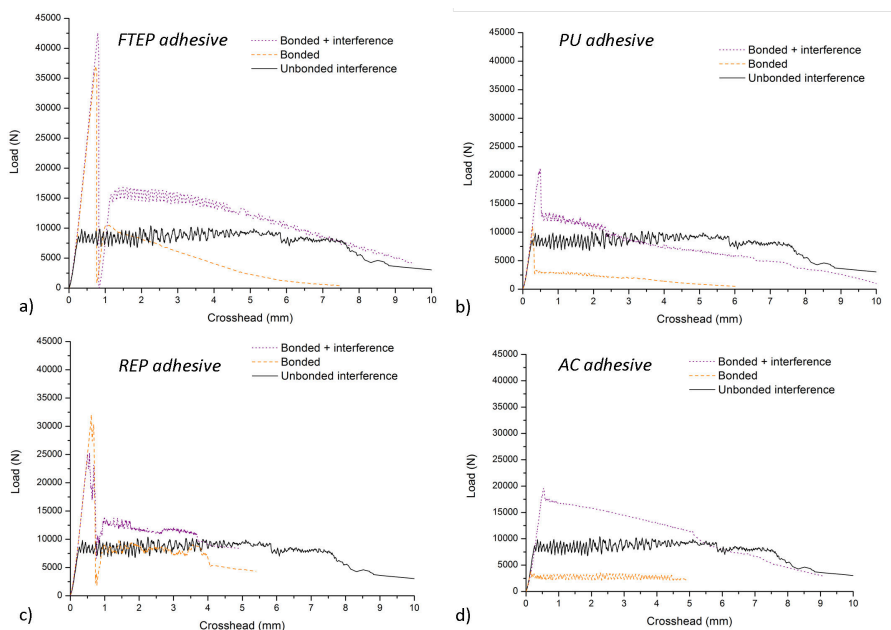

Figure 4.8: Average load/displacement curves of the hybrid, bonded with clearance and the unbonded interference samples of: a) *FT-EP* adhesive, b) *PU* adhesive, c) *R-EP* adhesive, d) *AC* adhesive.

The mean load/displacement curves related to *FT-EP* systems (Bonded, Interference, Bonded+interference in figure 4.8a) were converted in the corresponding mean stress/displacement curves reported in figure 4.9. The stress was calculated dividing the load by the bonded area, that was considered constant for the entire elastic section of the load/displacement curve. After the elastic region, when the shaft started to move, we assumed that the length of the bonded area was reducing according to the cross-head displacement from 10 mm to zero.

The interference provided a quite constant load resistance to the decoupling,

considering an average of the stick-slip trend. Since the bonding area was re-
ducing during the decoupling, the resultant calculated stress increased. The
stress-enhancing trend provided by the interference was clearly visible also in
the hybrid samples, making easier to detect the relevant contribution of the
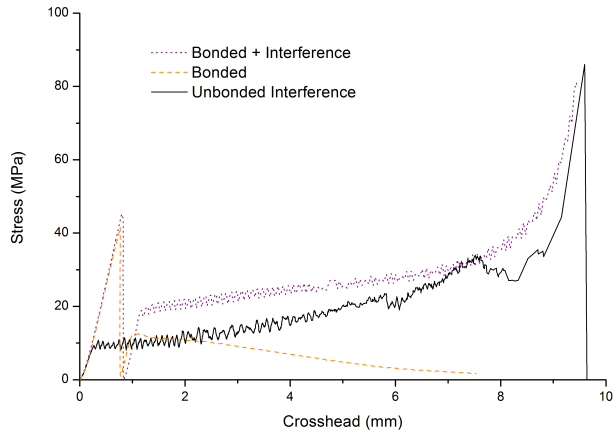interference after the breakup events.

Figure 4.9: Average stress/displacement curves of the hybrid, bonded with clear-
ance and the unbonded interference samples for the *FT-EP* adhesive [76].

The presence of the interference could also affect the stiffness of the hy-
brid system. The first elastic stretch of the curves of the hybrid systems are
compared in figure 4.10 with the ones of the systems bonded with clearance.
The differences in the slopes of the curves recorded by testing the bonded with
clearance samples were moderated in the hybrid systems by the interference.
Thus, it seemed that the interference could be able to control the stiffness of
the assembly.

In clearance conditions, among the examined adhesives, the *R-EP* provided
the stiffest samples, while the more flexible *PU* adhesive provided the samples
with the lowest stiffness. The *FT-EP* samples were characterized by interme-
diate values. Unfortunately, no precise and comparable information about the
Young modulus of the employed adhesives can be found in their data-sheets.
Among the two component adhesives we can say that the epoxy *R-EP* is a rigid
adhesive with a Young Modulus of 6700 N/mm^2 and an elongation at break
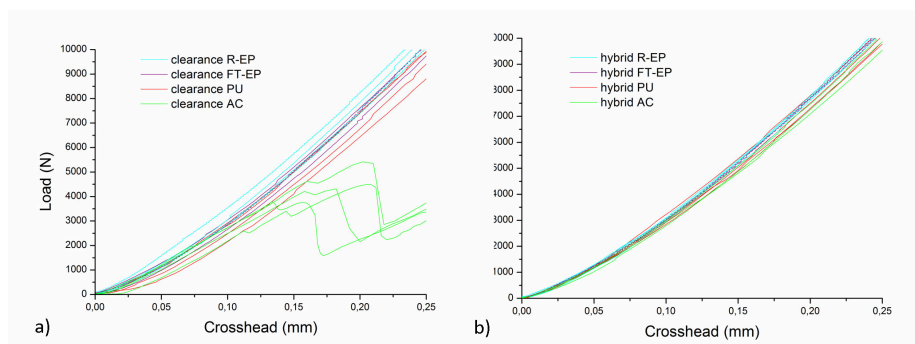of 0,8 %. The *FT-EP* is a more flexible and toughened blend, as stated by

Figure 4.10: First elastic stretch of: a) the bonded with clearance samples; b) the bonded with interference samples [76].

the supplier, but no comparable data are available. Finally, the PU adhesive is characterized by a lower modulus (576 N/mm^2) and a higher elongation at break (39 %) .

4.4   The effect of the roughness

The roughness of every hubs and shafts was checked and a mean value of R_a and R_z for every coupled sample was calculated according to the method reported in Chapter 3. Considering all the studied samples, the roughness values ranged around a mean value of 1,5 μm of R_a and 7 μmm of R_z. The frequency of the roughness values among the hub-shaft samples is reported in figure 4.11, where a statistical distribution could be detected.

No relation was found between the roughness values and the final strength of hybrid joints. As an example, in figure 4.12 the R_a values of the hybrid PU samples are reported as a function of the corresponding pull-out loads, showing that no particular trend can be noticed.

As stated in Chapter 2, there is not a unique interpretation of the effect of the roughness in the hybrid interference joint. Generally it is ascertain that roughening a surface can increase wettability and thus adhesion (for further information see paragraph 1.3.4), and evidence exist that roughness can also moderately influence the hybrid systems (for further information see paragraph 2.3.2). Notwithstanding this, it seemed that in the case of the press-fitted hybrid joint, the roughness played a slight effect on their pull-out loads. Moreover the
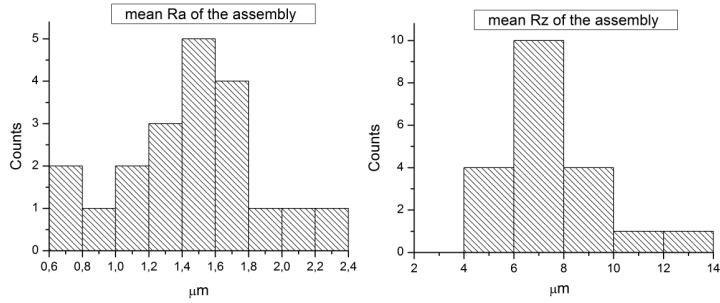
Figure 4.11: statistical distribution of the mean R_a and R_z calculated for every hub-shaft assembly [76].
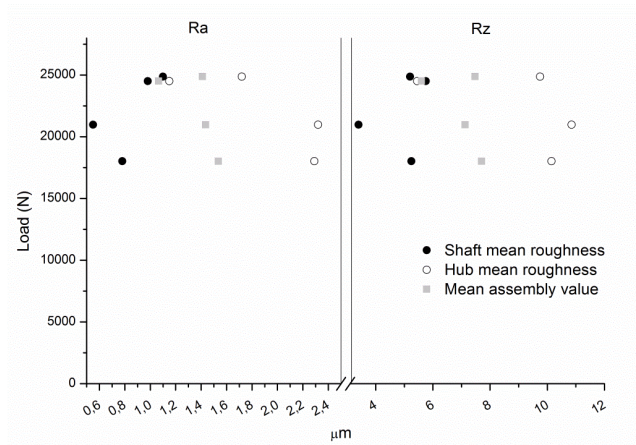

Figure 4.12: Values of R_a and R_z for the hubs, the shafts and the assembly for the 4 *PU* hybrid samples [76].

mating surfaces are in any case modified during the press-fit coupling, thus little differences in the values of R_a cannot influence the final performances of the joint.

4.5   Hybrid joint adhesion strength enhancement

The mean adhesion strength values of all the studied systems were extrapolated and the related data are reported in figure 4.13. For every joint the adhesion strength was calculated by dividing the first load peak of the decoupling curve by the nominal coupling area. The data collected in figure 4.13 were also in this case the resultant mean values of the four measured samples for every system.
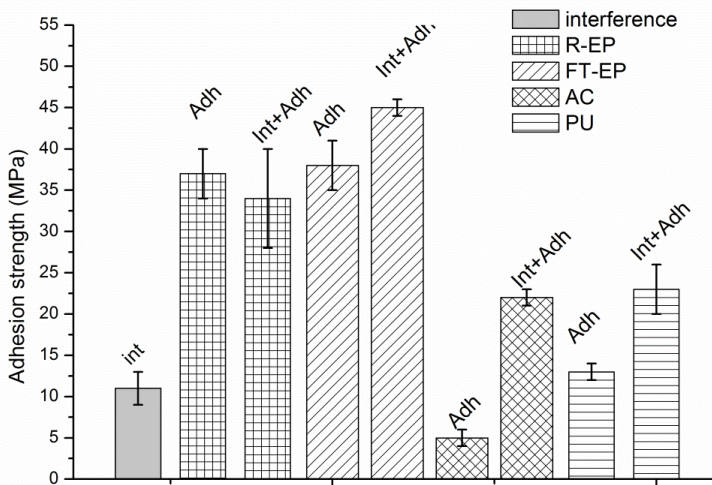
Figure 4.13: Comparison between the adhesion strength values of all the studied adhesive systems. The interference system is labeled as "*Int*", the bonded with clearance systems as "*Adh*", the hybrid systems as "*Int+Adh*" [76].

From figure 4.13 it was possible to observe that the adhesion strength of every adhesive was modified by different extents in the presence of the same level of interference. A similar interference contribution for every hybrid system could be assumed taking into account a mean interference value of $17 \pm 4 \ \mu m$

among the specimens. The resultant strength given by the interaction between the adhesive and the interference contribution changed in respect of the adhesive type.

The hybrid joints prepared with the *FT-EP* and *PU* adhesives presented an increase in the adhesion strength with respect to the unbonded samples. The use of the *FT-EP* adhesive provided values of maximum decoupling load four times higher than those of the interference alone. In the case of the *PU* adhesive, the interference decoupling load was doubled in the hybrid joints . The *R-EP* was the only adhesive that seemed to be negatively affected by the interference. This result was surely related to the high data dispersion already discussed in paragraph 4.3, and it was probably connected to the rheology of this adhesive.

Particular attention must be paid to the acrylic system. The *AC* adhesive presented the higher resistance improvement in the presence of the interference fit. Indeed, even considering the theory of the superposition of the effects (for further information see Chapter 2), in this case the resistance of the hybrid joint was higher than the sum of the "*adhesive*" and "*interference*" contributions. However, it must be taken into account that this heightening could be overestimated, considering the low results obtained with the adhesive alone. The mean value of adhesion strength of clearance *AC* joints was equal to 5 MPa. This value seemed to be too low if compared to those stated in the datasheet of the adhesive. Further experiments were carried on and single lap shear tests were conducted on *AC* bonded carbon steel. The obtained mean values of the shear tests was ∼12 MPa. The reason of the low performances of the *AC* clearance joint was probably due to the compressed air that remained inside the coupled cylindrical joint. During the push-in phase of the shaft into the hub, the air inside the hub could partially escape through the clearance between the two components, affecting the curing of the anaerobic adhesive. This poor result did not occur in the hybrid joint, where the interference entrapped the air inside the joint promoting the curing of the anaerobic adhesive in a correct absence of oxygen. This could confirm the role of an incomplete curing on the low mechanical behavior of the clearance *AC* samples.

As a consequence of this evidence, in the later experiments (described in Chapter 5), a little hole was opened inside the hub in order to permit an escape route for the compressed air. Anyway, some considerations must be done about the supplementary forces that the air pressure could create inside the joint. According to an approximate evaluation based on the Boyle's law, the volume variation caused by the coupling creates an increase in pressure inside the joint of about 0.02 MPa. This value corresponds approximately to a force acting on the shaft of about 15 N. It is reasonable to consider this force negligible

compared to the obtained values of the pull-out load of the hybrid joints (20000 - 45000 N).

4.6 Conclusions

- Assuming similar interference contributions for every hybrid systems, the resultant interaction with the adhesive contributions seemed to change in respect of the adhesive type: a downgrade for the *REP* an enhancement of different proportion for the <u>AC</u>, *FTEP* and *PU*.

- Both the curing technology and the chemical nature of the adhesive were able to influence the decoupling behavior of the hybrid joints. Epoxies and polyurethane adhesives presented similar curves characterized by an high initial peak, identified with a drastic adhesive failure, and a subsequent plateau related to the interference contribution. On the other hand anaerobic acrylic samples were characterized by an almost irrelevant adhesive failure peak and an higher interference contribution.

- The stiffness of the hybrid joints seemed to be not influenced by the rigidity of the different adhesives, but it was mostly ruled by the presence of the interference.

- The rheology of the adhesive was an important factor to take into account in the press fit joint, influencing the quantity of adhesive that remains between the mating surfaces and its consequent contribute to the strength of the adhesive joint.

Chapter 5

Interference contribution on the performance of the hybrid joint

Abstract

The contributions of the adhesive and the interference on the performance of the final joint were still not completely clear. Hub-shaft samples, joined by means of a press fit and a toughened and flexibilized epoxy adhesive were tested under an axial pull-out load. Hybrid joints were compared to both adhesive joints in clearance conditions and interference joints. In particular, different levels of interference were analyzed in order to clarify the role played by the tensile field between the hub and the shaft, and the influence of the friction effects between them. Numerical simulations and analytical approach were also employed to support the experimental data in the evaluation of the contribution of the interference level and all the other phenomena influencing the hybrid system. It was found that tribological phenomena played an important role in governing the mechanical behavior of the unbonded samples, while they can be considered negligible in the presence of the adhesive. The correlation between bonded and unbonded press-fitted joints was investigated pointing out that the maximum strength of the hybrid joint is mainly related to the resistance of the epoxy adhesive.

5.1 The resistance of the unbonded interference fit joints

The strength of a solely interference fit joint in static axial push out depends on the pressure between the hub and the shaft P, the friction coefficient μ, and the contact area, according to equation 2.1 discussed in paragraph 2.2. Moreover, the radial pressure P linearly depends on the interference fit level δ of the mating parts, that can be computed as stated in equation 2.2. Thus, also a linear relationship between the interference level and the pull-out resistance can be expected.

5.1.1 FE model and theoretical behaviour

A 3D finite element study of an interference fit assembly subjected to external loads was performed in collaboration with the Department of Management and Production Engineering (DIGEP) of the Politecnico di Torino also involved in the partnership with MW spa.

FE models enable to analyze perfect shapes with nominal values that cannot be, on the contrary, easily manufactured and tested. All the boundary conditions can be kept constant, without introducing new affecting variable parameters, and the influence of every variable can be isolated and studied. Thus a numerical analysis of the shaft-hub assembly process provides useful information to theoretically evaluate the effect of the interference level on the pull-out resistance of the unbonded joints. Moreover, the stress distribution of the two components can be detected.

A numerical model made of $2 \cdot 10^5$ linear tetrahedral elements of type C3D4 was developed in Abaqus, as presented in figure 5.1.

Figure 5.1: Finite element model: assembly mesh with tetra elements (C3D4) [75].

A static analysis of the fitting force and pull-out behaviors was run. The procedure was divided in three steps: the push-in phase during which the shaft is press-fitted into the hub, the spring-back phase during which applied forces are removed and constraints for reaching null reaction forces are properly selected, and the following pull-out phase that brings the shaft into the initial position.

Boundary conditions similar to those employed during the experimental set-up were applied to the numerical model: enforced displacement was set on the threaded end of the shaft, whereas fixed displacement for the threaded end of the hub. Assuming negligible plastic deformations, the performed analysis was linear.
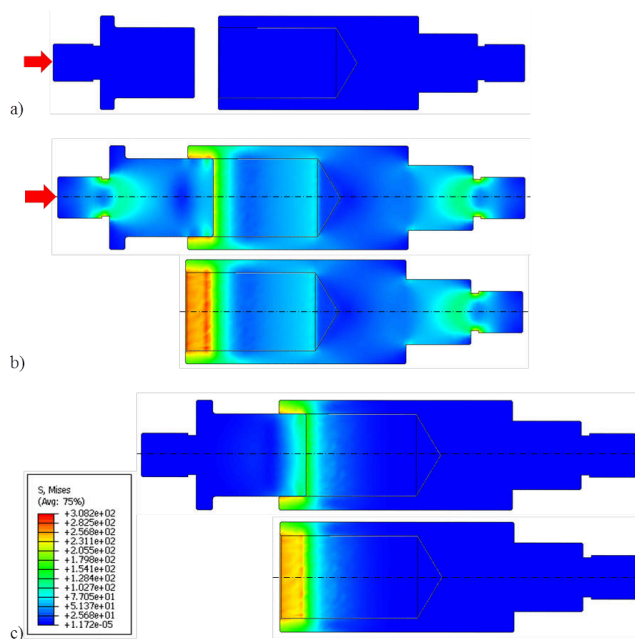
Figure 5.2: Stress map (Von Mises [MPa]) on hub and shaft, cut view: a) beginning of fitting process, b) end push-in phase, c) end of spring-back phase [75].

Proper contact sets for the mating surfaces were applied both on the outer surface of the shaft and the inner surface of the hub. Different values of the

friction coefficient were employed, taking into account an upper limit of $\mu = 0.4$ representing the nominal condition in the case of dry steel-steel contact, and a lower limit ($\mu = 0.3$) to simulate the slightly lubricated surfaces of the specimens. The material properties used the for the described model were: Young's modulus $E = 190 - 210$ GPa, Poisson ratio $\nu = 0.3$, density $\rho = 7900$ kg/m^3. The changes in Young modulus E and the friction coefficient μ parameters were made in order to simulate a certain uncertainty in the material properties and contact conditions.

Von Mises stresses for three different frames during the process are depicted in figure 5.2. By observing the stress field at the end of the fitting process, it could be stated that the interference fit affects the mating surface and mainly the hollow tube. The stresses concentrated along the constrained ends of the two components (figure 5.2b) dropped to zero after the spring back phase (figure 5.2c), and only near the contact surfaces a pre-stress condition was maintained. The highest values were reached on the interior surface of the hollow tube, but the stress field can be considered quite constant and the main contribution was due to a circumferential stress.
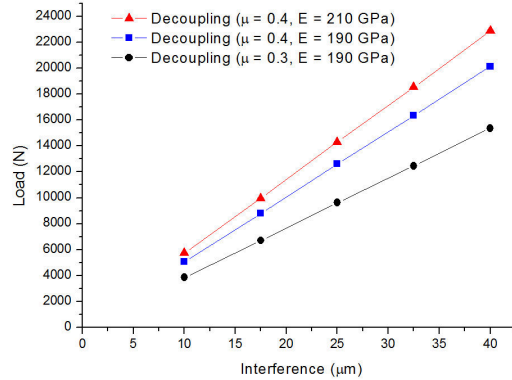

Figure 5.3: Numerical data of the max pull-out forces of unbonded joints by comparing different values of Young Modulus and friction coefficient [75].

Three static analysis were run, changing the Young modulus E and the friction coefficient μ parameters. The obtained results of the pull-out resistance of the unbonded joints are plotted in figure 5.3. As expected a linear relation

between the interference level and the pull-out force were found. The variability in the friction coefficient gave rise to a range of max pull-out force that tended to grow by increasing the interference fit level, and the gradient of the linear trend rose up as the elastic modulus of the material was increased.

5.1.2 Experimental behavior and tribological effects

Unbonded interference-fit samples were prepared on the basis of the press-fitted hub/shaft joint described in Chapter 3. The samples were tested under a static axial pull-out load, performed with a traction test using a Zwick z-100 dynamometer with a crosshead rate of 1.3 mm/min (for further information see section 3.2.3). The prepared samples with the corresponding dimensions of hub and shaft and the calculated interferences are reported in table 5.1.

Table 5.1: Unbonded press-fit samples

Sample	Mean hub diameter [mm]	Mean shaft diameter [mm]	Mean interference [μm]
IS10/fH18	29,999 $\pm$ 0,001	30,009 $\pm$ 0,002	9,5 $\pm$ 2
IS07/fH26	29,999 $\pm$ 0,005	30,009 $\pm$ 0,002	10 $\pm$ 7
IS14/fH7	29,999 $\pm$ 0,001	30,009 $\pm$ 0.001	10 $\pm$ 2
IS03/fH15	30,000 $\pm$ 0,001	30,010 $\pm$ 0,002	10,5 $\pm$ 3
IS16/H25	29,984 $\pm$ 0,005	30,007 $\pm$ 0,001	23 $\pm$ 6
IS15/0H6	29,983 $\pm$ 0,001	30,007 $\pm$ 0,001	24,5 $\pm$ 3
IVS12/fH3	30,011 $\pm$ 0,004	30,039 $\pm$ 0,002	28,5 $\pm$ 6
fS8/0H8	29,992 $\pm$ 0,001	30,023 $\pm$ 0,002	31 $\pm$ 3
fS2/fH35	29,997 $\pm$ 0,004	30,032 $\pm$ 0,001	35 $\pm$ 5
fS34/fH36	29,998 $\pm$ 0,004	30,033 $\pm$ 0,001	35 $\pm$ 5
fS7/fH11	29,998 $\pm$ 0,003	30,033 $\pm$ 0,002	35 $\pm$ 5
fS6/H2	29,998 $\pm$ 0,004	30,033 $\pm$ 0,002	35 $\pm$ 5

Assuming the same friction coefficient between steel and steel for all the samples, the theoretical linear relationship between the interference and the pull-out force should be expected also at the experimental level. Nevertheless, the formulas (equation 2.1 and 2.2) and the numerical analysis (see section 5.1.1) describe an ideal simplified system; wear and micro-adhesion phenomena between the two steel components occurred during the decoupling of the real interference joints without lubricants. In fact, the experimental results related

to the unbonded joints were affected by a wide variability of the results, as
can be seen in figure 5.4. By analyzing the experimental results, even if it
possible to observed that joints with higher interference levels required higher
decoupling loads, the expected linear relationship was not verified. In figure
5.4b the experimental points are compared with the results of the numerical
analysis and the values obtained by processing the data reported in table 5.1
with the analytical equations (equation 2.1 and 2.2).

The influence of the friction coefficient and the Modulus of the steel on the
pull-out values can be verified by varying these parameters in the numerical
and analytical solutions. For instance, by varying the friction coefficient from
a value of 0.3 (in the case of slightly lubricated surfaces) to a maximum of 0.8
(in the case of dry steel contact) [91]. Nevertheless, it is impossible to refer
the experimental results to one of these theoretical systems, because of the
high deviation of the data, especially at higher interference values (samples at
$\delta=35\mu$m).
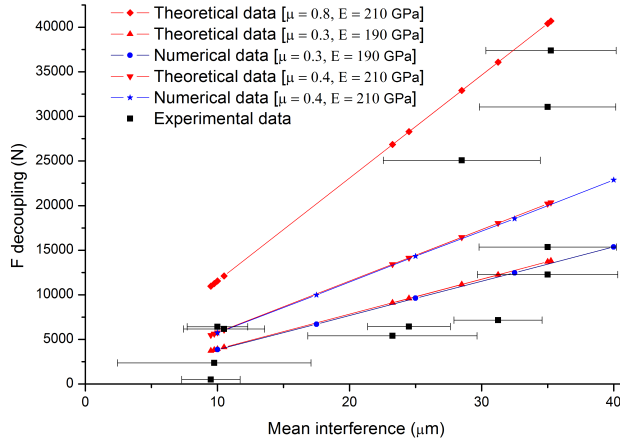
Figure 5.4: Max pull-out force of unbonded samples at different interference
levels compared with theoretical and numerical data.

The observation of the contact surface of the samples after the decoupling
(figure 5.5) confirmed the occurrence of wear and micro-adhesion phenomena
between the two steel components. In order to verify if these friction phenom-
ena occurred both during coupling and decoupling operations, the surface of

a coupled shaft was observed cutting the hub after the joint was assembled by press-fit. The shaft surface was slightly scratched, demonstrating that the friction phenomena started to occur during the coupling phase.
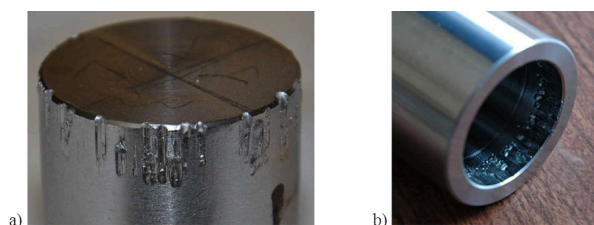

Figure 5.5: Scratches present after the decoupling on both the mating surfaces of: a) shaft and b) hub [75].
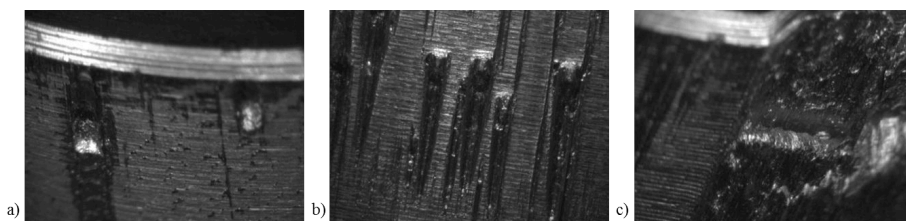

Figure 5.6: Scratch pattern on shaft due to: a) the coupling effect, b) the decoupling effect, c) the coupling + decoupling effect [75].

The fracture surface of the coupled shafts was compared to that of a decoupled sample by means of microscopic observation. The employed microscope was a Leica DVM2000. Different shapes of the scratches can be identified in the mating area of samples due to the coupling or decoupling operations. The different patterns of scratches are reported in figure 5.6. It was possible to note that the scratches presented a preferential direction: in fact, the material was dragged in the opposite way with respect to the moving direction of the shaft. Thus, during the coupling operation (Figure 5.6a) the scratches were oriented in the opposite way to the direction of insertion of the shaft into the hub. On the other hand, several scratches in decoupled samples presented the opposite orientation as a result of the material dragged during the decoupling (Figure 5.6b). In certain specimens, especially for higher interference levels, the scratches were

characterized by more complicated shapes due to multiple deformations in both coupling and decoupling phases (Figure 5.6c). These more complicated shapes could give rise to a sort of interlocking mechanism between the two mating surfaces. Thus, it seemed reasonable to suppose that the scratches were formed during coupling and they were further amplified and deformed during the decoupling.

In order to quantify the extent of the wear on the decoupled samples, the surface was analyzed by means of a profilometer. The measurements were carried on with the profilometer Marsurf XC2. This machine is able to sample a linear section of a standard length obtaining a roughness profile. The measured real profile with all the scratches and imperfections was arithmetically averaged in order to obtain a best fitted ideal mean profile. By subtracting the measured real profile to the averaged ideal one an absolute value of discrepancy was obtained. This discrepancy was a R_a roughness value. An example of the profile analysis of a decoupled shaft is reported in figure 5.7.
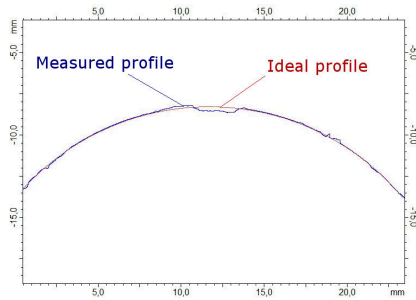

Figure 5.7: Discrepancy between the real profile of a decoupled scratched interference fit joint from its averaged ideal profile [75].

Thus, an absolute value able to indicate the extent of scratches was obtained for every shafts. The measurements were carried out by evaluating a quarter of the circumference of the shaft at a time. Two measurements, one at the beginning of the decoupling length, the other at the end, were made for every quarter of circumference. Then a mean value of the eight measures was extrapolated for every shaft obtaining in this way a parameter labeled as *scratch profile roughness value* (spR_a).

The scratches provided some additional resistance during the whole decoupling process. Besides the energy wasted in the friction phenomenon, the scratches probably could locally give rise to mechanical interlocking mechanisms

implying the formation of further scratches on the surface of the specimens. This additional grip resistance was visible on the decoupling curves of the specimens presented in figure 5.8. In the curves of the samples affected by an extended wear, the maximum load recorded by the test machine occurred when the decoupling was already in the middle of its length. Assuming the ultimate strength of the joint as the point in which the joint forces are broken and the shaft starts to move, we should consider the "*yield point*" of the curve as the joint resistance. When the shaft started to move, the coupling area was reduced but the load continued to increase. This additional contribution is in contrast with the theoretical system according to which when the area is reducing the decoupling load is also reducing. Thus, the phenomena related to a micro-adhesion of metal to metal and parts of the broken surface that induce mechanical interlocking forces were the probable causes of the increase in the load during the progress of the decoupling.
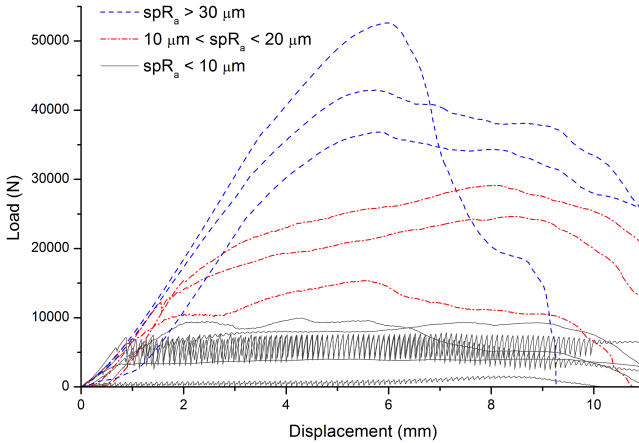

Figure 5.8: Load-displacement curves of unbonded press-fit joints during the decoupling phase: three classes of samples could be identified in relation to the extent of the scratch phenomena detected on the shaft after the decoupling.

In figure 5.8, it is possible to observe that the samples with a spR_a value higher than 10 μm reached the maximum decoupling load when the shaft had already started to move. Instead, the samples showing low values of spR_a presented decoupling curves characterized by a stick-slip behavior, as observed

in previous experiments (see Chapter 4). It was reasonable to assume that the low speed of testing induced a discontinuous decoupling with consecutive stick–slip states only in unbonded samples without a significant presence of wear.

According to Bowden and Tabor [91], when a metallic junction is formed between two sliding surfaces made of the same metal, the wear phenomenon including process of deformation, local adhesion and welding can appreciably increase its shear-strength. In this case the shearing of the junction rarely occurs at the interface itself, but would take place within the bulk of the metals, producing very large surface damages of both the sliding bodies.

The importance of the wear and micro-adhesion phenomena on the resistance of the unbonded joints could be appreciated by plotting the spR_a as a function of the obtained pull-out loads (figure 5.9). In this case, a linear relationship between the effect of the friction phenomena and the measured resistance of the joint could be detected. The samples more affected by the friction phenomena are also the ones that provided the maximum decoupling loads. As no scratches occurred at lower loads, it could be argued that only when certain stresses were reached at the contact interface, the wear and micro-adhesion phenomena began to occur.
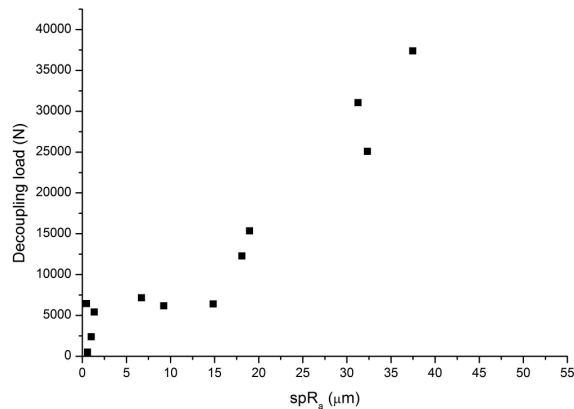

Figure 5.9: Relation between the spR_a, consequence of the friction phenomena, and the resistance of the joint [75].

Bowden and Tabor [91] stated that there is not a direct relation between the

amount of wear and the friction coefficient. The mechanism of wear is a complex process which includes many variables related to the type of junction formed. For instance, the formation of oxide layers on the surface plays an important role, especially in the absence of lubricants. According to more recent literature [97], the micro-structure of the sliding metals, their hardness and their melting point in relation to the temperature developed by friction are the critical properties able to control the wear due to the micro-adhesion phenomena.

The influence of the interference level on the friction and wear phenomena was checked plotting the extent of the scratches as a function of the interference (figure 5.10a). Important surface damages occurred more frequently at higher interferences, but among the investigated samples, a clear relation between the extent of the scratches and the interference was not evident (figure 5.10a).
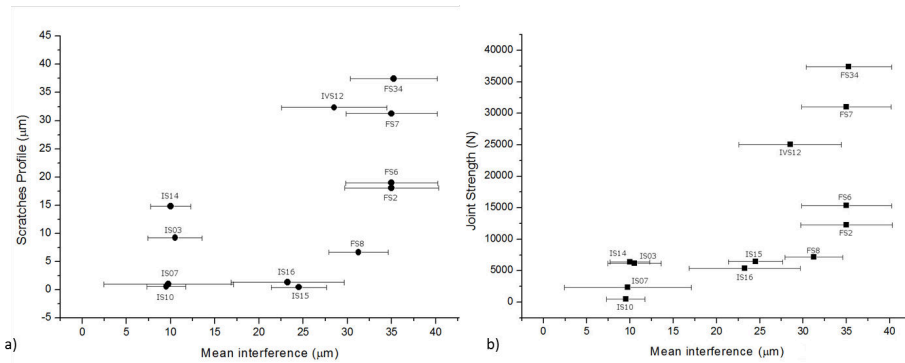

Figure 5.10: Relation between the spR_a and the interference level (a) and its consequence on the measured decoupling loads (b)

Comparing the results shown in figure 5.10a with the relation between the interference and the decoupling load of the samples (figure 5.10b), it was possible to better understand the high dispersion of the data related to the unbonded joints and the not linear relationship between the interference level and the decoupling loads. Considering the two samples IS14 and IS03 (with an interference level of 10 μm) in figure 5.10b, they presented almost the same resistance of samples IS15 and IS16 at 25 μm of interference. This is due to the fact that the former specimens presented a more evident wear than those with 25 μm of interference (figure 5.10a). Indeed, the samples with the most evident surface damages presented the highest resistance among the ones at the same

interference level. Thus, the resultant resistance of the joint seemed to be affected by both the parameters: the pressure between the components due to the interference and the phenomena related to friction and wear. Probably, the latter contribution played a more important role as an almost linear relationship between those effects and the decoupling loads was observed (figure 5.9).

The analytical formula and the numerical analysis considered a unique value of the friction coefficient that did not take into account the wear and micro-adhesion phenomena observed on the metal-metal interface. The joints that presented low extent of scratches could be modeled more efficiently with the analytical and numerical solutions, thus only these joints were taken into account for further analysis.

5.2   The resistance of the hybrid joints

The hybrid joints resistance was detected by pull-out measurements on hub/shaft assemblies. The tests were performed using a Zwick z-100 dynamometer with a crosshead rate of 1.3 mm/min, as for the unbonded interference samples. The adhesive used was the flexibilized and toughened epoxy adhesive (*FT-EP*), selected on the basis of the previous tests described in Chapter 4. The same surface preparation was followed for each sample. The surfaces of hubs and shafts were cleaned with acetone, dipped in acetone and placed in an ultrasonic bath for 5 minutes. The adhesive was cured for 24 hours at room temperature, with a post-curing treatment at 80 °C for 1.5 hours. The tested samples were characterized by a level of clearance of -22.5 μm and three different level of interference at 10, 22.5 and 35 μm, as reported in table 5.2.

5.2.1   Interference contribution detected from hybrid joints

No scratches and wear was present on the mating area of the hybrid joints after the decoupling. Confirming the previous experiments, (see Chapter 4) the mating surfaces of both the components was covered by a thin layer of adhesive, as illustrated in figure 5.11. During the coupling operation, the adhesive, still liquid, act as a lubricant preventing friction effects. During the decoupling, the cured adhesive avoids the direct metal-metal contact and consequently the formation of scratches.

The fracture surfaces of hubs and shafts were observed and a section of the bonded area of the shaft for each case study was analyzed at the Scanning Electron Microscope (SEM). Unfortunately, it was not possible to properly measure

Table 5.2: Bonded press-fit samples

Sample	Mean interference [μm]	Sample	Mean interference [μm]
IS12/fH20	10 ± 2	fS4/fH29	35 ± 6
IS04/fH31	10 ± 6	fS18/fH32	35 ± 5
IS01/fH9	10 ± 2	fS40/H24	35 ± 3
fS13/fH39	9 ± 4	fS9/fH23	35 ± 3
		fS31/fH13	35 ± 2
0H9/IS09	23 ± 3	fS20/fH4	35 ± 2
0H5/IS05	23 ± 2	fS3/fH6	35 ± 3
0H4/IS08	22 ± 4	fS39/fH37	35 ± 3
0H2/IS06	22 ± 1		
0S8/0H7	-22 ± 1	0S9/0H10	-23 ± 2
0S4/0H1	-22 ± 1	0S5/0H14	-23 ± 2

the thickness of the adhesive layer in respect to the level of interference studied. Very few differences were observed between the samples at different levels of interference and the process itself of cutting a section of fracture surface for the SEM analysis could remove some particle from the adhesive layer. The fractures were most likely a mixed mode between adhesive and cohesive failure types. Nevertheless it is certain that a quantity of adhesive always remained inside the joint without being split away at each level of interference, as already observed by other researchers [54]. As an example a SEM magnification of the fracture surface of a shaft at 35 μm is shown in figure 5.12. It is appreciable that residues of the adhesive layer were present over the metal surface of the shaft.

The samples presented the same mechanical behavior detected in previous experiment involving the *FT-EP*: an initial peak corresponding to the breakup of the adhesive, followed by an additional load related to the interference contribution. The curves of this additional load were characterized by a stick-slip behavior, typical of the interference joint without the presence of relevant friction effects. The adhesive joints in clearance conditions were also characterized by a residual load level after the breakup of the adhesive, as observed in previous experiments. This is due to the friction forces between the cured adhesive residues present on the fracture surfaces (for further information see Chapter
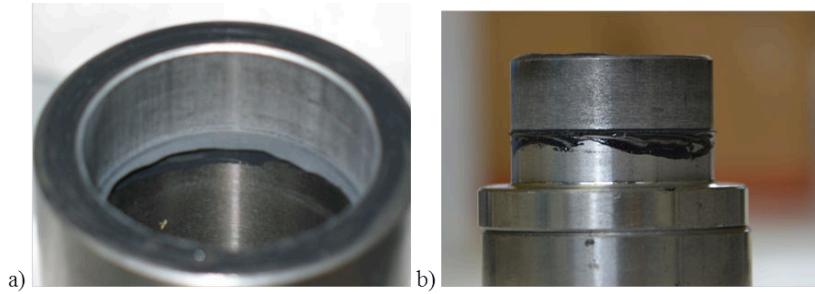
Figure 5.11: a) Hub and b) shaft of a hybrid joint at 35 μm of interference after the decoupling phase [75]
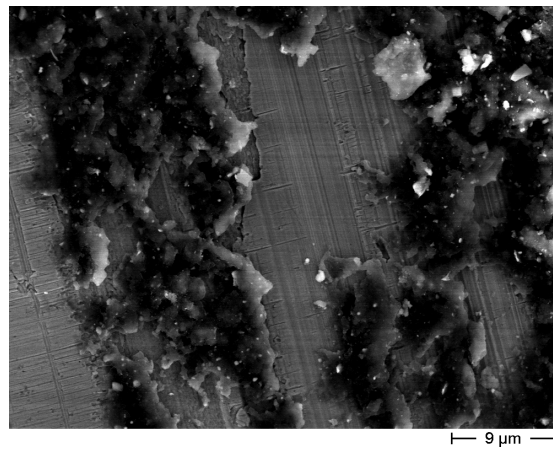

Figure 5.12: SEM magnification of the fracture surface of a shaft from a hybrid joint at 35 μm of interference after the decoupling phase

4).

The hybrid joint samples with three different classes of interferences (10, 22,5 and 35 μm) provided three different additional loads after the breakup of the adhesive. Some examples of load-displacement curves related to the decoupling of hybrid joints at different levels of interference and of an adhesive joint in clearance condition are shown in figure 5.13.
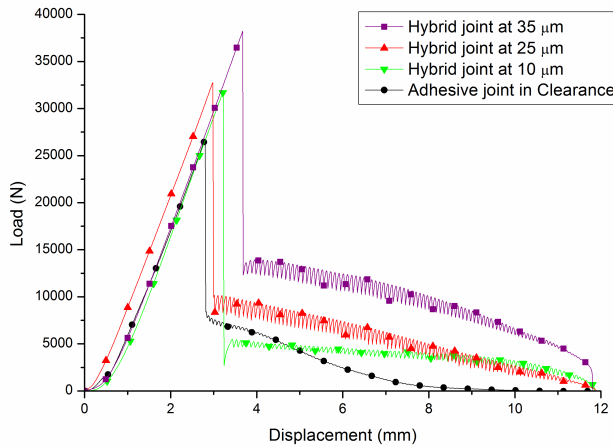
Figure 5.13: Decoupling curves of three hybrid joints at different interferences and an adhesive joint in clearance condition. The curve of one sample among the four tested is shown in the graph, as an example. [75]

The load after break in the hybrid joints mainly depended on the radial contact pressure present between the hub and the shaft due to the interference fit. The important contribution due to the friction and wear phenomena observed in the unbonded samples is absent in these joints, thus the load after break can be most likely referred to the system described by the analytical equations and the numerical analysis (see equations 2.2 and 2.1 and paragraph 5.1.1). According to this hypothesis, the load after break can be more easily related to the contribution provided by the interference level. In order to obtain an estimation of this additional load, the mean value between the first peak and first valley of the stick and slip state was calculated. The obtained values are plotted in figure 5.14 compared to those of the unbonded interference samples.

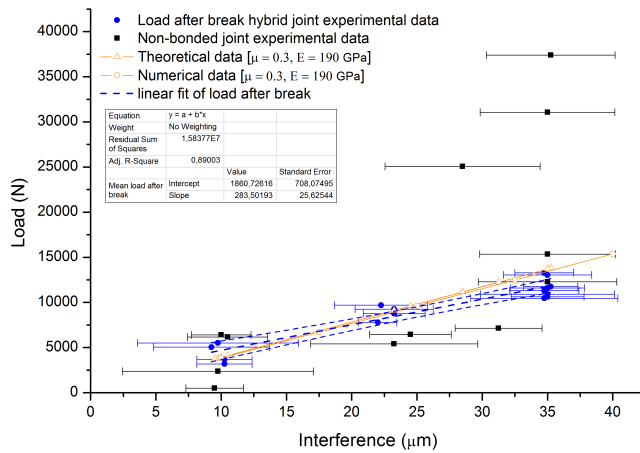As highlighted in figure 5.14, the loads after break of the hybrid joints were

Figure 5.14: Comparison among the interference contribution detected from the load after break of hybrid joints, the unbonded interference samples, and the results of the analytical equations and the numerical analysis. The linear fits of the experimental points with the related 95% confidence bars are also depicted.
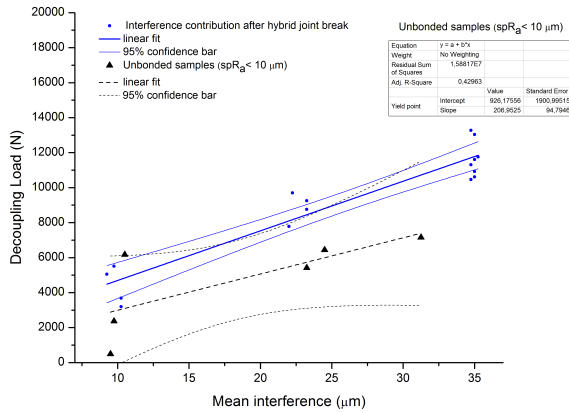
(a)
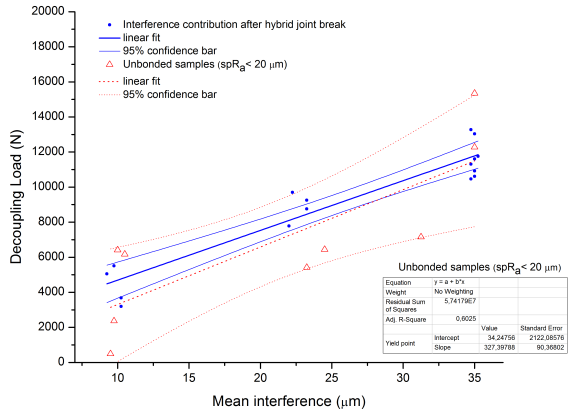
(b)

Figure 5.15: Comparison between the linear fits of the load after break points, and results of the unbonded joints characterized by values of (a): $spR_a < 20$ μm, and (b): $spR_a < 10$ μm

in good agreement with the analytical and numerical solutions that exploit a coefficient of friction equal to 0.3 and a Modulus of the steel adherends of 190 GPa. The linear fit of the experimental data provides a good level of confidence, with a R-squared of 0.89. The linear fit of these data is in better agreement with the theoretical curves with respect to the experimetal points obtained by the unbonded samples.

In figure 5.15, the linear trend extrapolated by the loads after break is compared with the results of the unbonded samples characterized by a spR_a values lower than 20 μm (figure 5.15a) and < 10 μm (figure 5.15b).

The points related to the unbonded samples characterized by a large extent of friction phenomena (values of $spR_a > 20$ μm) were excluded from this data analysis. The points related to the samples with values of spR_a lower than 20 μm presented a similar trend with respect to those relating to load after break values, but with a higher variability confirmed by the wider confidence bars. The points characterized by a spR_a lower than 10 μm (black triangles in figure 5.15b) were related to the unbonded samples that present considerably low friction and wear phenomena and a stick -slip decoupling behavior. It was possible to note that the majority of these samples lied under the load after break points. This could be related to the presence of the cured adhesive layer between the components in the hybrid joints. As reported in Chapter 4, the cured adhesive remaining on the mating surfaces implied a slight increase in the radial pressure between the hub and the shaft, on the basis of the adhesive used. This additional contribution was not high in value, and could be estimated by comparing the linear fits of the loads after break to the ones of the unbonded samples with a spR_a lower than 10 μm (black and blue lines in figure 5.15b).

The above described data suggested that the values of the load after break of hybrid joints could be useful parameter to understand the interference contribution in these samples. In the following paragraph this parameter is taken into consideration.

5.2.2   The resultant strength of hybrid joints

The total resistances of the hybrid joints are plotted in figure 5.16 together with the interference contributions detected from the loads after break of the same samples. In addition the resistances of adhesive joints in clearance condition are also presented.

The total resistance of the hybrid joints is characterized by a high dispersion of the data. It is still possible to see that the interference enhanced the joint strength of the hybrid systems, especially for higher levels of interference. This
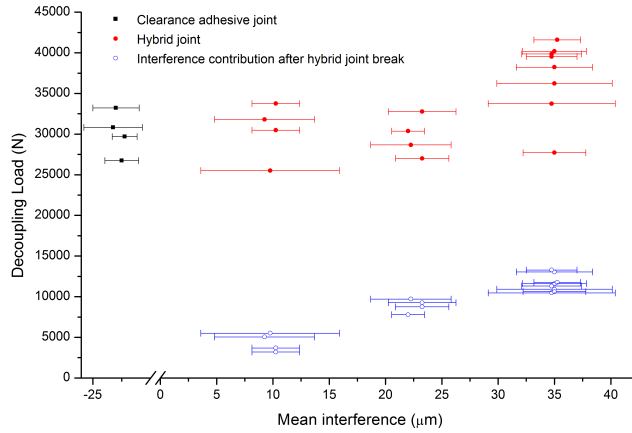
Figure 5.16: Load-interference plot of the resistance of the hybrid joints (red points), the interference contribution detected by the load after break of the hybrid joints (blue circles) and the adhesive joints in clearance condition (red squares)
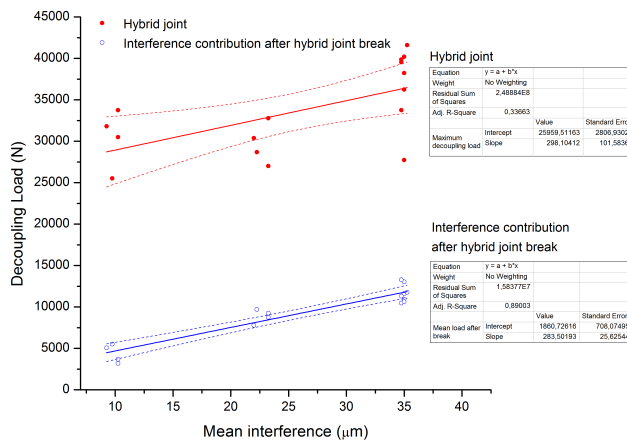

Figure 5.17: Linear fit of the experimental points of the hybrid joints (and 95% confidence bars) and the interference contribution detected by the load after break of the hybrid joints (and 95% confidence bars)

variability was probably introduced by the adhesive contribution, since the load recorded after the break of the same hybrid joints was clearly dependent on the level of interference, with a low dispersion of the data. Thus, the total strength of the hybrid joint seemed to be ruled to a large extent by the resistance of the adhesive. As a matter of fact, the strength values of the adhesive joints in clearance condition were in the same order of magnitude.

The linear fit of the points related to the hybrid joints resistance is compared in figure 5.17 with that obtained by the load after the break of the same joints. The two linear fits were characterized by similar slopes, suggesting that the resistance of the hybrid joint is enhanced accordingly to the interference contribution. This parallelism can be referred to the theory of the superimposition of the effects of the pressure between hub and shaft and the resistance of the adhesive. But, the theory of superposition can not be confirmed because of the high dispersion of the data of the hybrid joints resistance. The linear fit of these points has a coefficient of determination, R^2, of 0.3, indicating a poor correlation with the experimental data and thus an uncertain slope.

5.3   Fatigue behavior of hybrid joints

The hybrid joints at 35 μm of interference and the bonded with clearance samples were tested under fatigue loading in order to investigate a beneficial influence of the interference on the fatigue behavior of the joints. A tension–tension fatigue test was performed with a Rumul Testronic 100K resonant testing machine. For further information on the adopted test method see section 3.2.3.

The specimens were loaded with a force amplitude set on the basis of the previous static tests:

- The minimum load force (F_{min}) was set at 10 KN, on the basis of the interference contribution detected on the hybrid joint at 35 μm.

- The maximum load force (F_{max}) of the test was varied and represented as a percentage of the average static resistance of the joint ($\%SR$).

The same load amplitude was employed both for the hybrid samples and the bonded with clearance ones in order to obtain comparable results. The static resistances used as reference for both the cases were calculated from the previous experiments (see the samples characteristics in table 5.2 and the results in figure 5.16). The reference values were:

- for the hybrid joints at 35 μm of interference: 39000 $\pm$ 2200 N;

- for the adhesive joint at -22,5 μm of clearance: 30000 $\pm$ 2700 N

The frequency of the test was dependent on the typical frequency of the samples as the fatigue machine operated in resonance frequency. Both the systems were characterized by similar resonance frequencies of 198.5 $\pm$ 1.5 Hz.

The single fatigue test was considered terminated at the attainment of 10^6 fatigue cycles or at the joint failure (identified by a variation in the testing resonance frequency). The samples that withstood the total amount of fatigue cycles were tested statically at the traction machine in order to evaluate an eventual decay of their pull-out strength.

The results of the fatigue tests are reported in table 5.3 for both the hybrid samples and the clearance ones. Two samples were tested for each investigated amplitude value, with the exception of the hybrid joints at the amplitude 10-32 KN and the clearance joint at 10-27 KN where it was possible to test only one sample.

Table 5.3: Fatigue test results

Sample name	Interference level (μm)	Stress amplitude (KN)	F_{max} - %SR	Cycles attained	Following pull-out strength (N)
Hybrid joints					
fS3/fH6	35 $\pm$ 3	10-16	45%	10^6	39854
fS9/fH23	35 $\pm$ 3	10-16	45%	10^6	40188
fS20/fH4	35 $\pm$ 2	10-20	55%	10^6	41598
fS31/fH13	35 $\pm$ 2	10-20	55%	10^6	39541
fS17/fH38	35 $\pm$ 4	10-26	70%	10^6	37810
fS36/fH19	35 $\pm$ 2	10-26	70%	10^6	38929
fS38/fH16	35 $\pm$ 3	10-30	85%	10^6	32780
fS15/fH5	35 $\pm$ 2	10-30	85%	10^6	32733
fS18/fH17	35 $\pm$ 2	10-32	90%	469605	/
fS26/fH8	35 $\pm$ 3	10-34	95%	138403	/
fS21/fH10	35 $\pm$ 2	10-34	95%	50213	/
Clearance joints					
fS33/0H3	-25 $\pm$ 3	10-18	60%	10^6	33467
0S6/0H16	-23 $\pm$ 1	10-18	60%	10^6	29850
0S10/0H12	-23 $\pm$ 2	10-24	80%	94377	/
fS37/0H15	-23 $\pm$ 1	10-24	80%	81811	/

fS25/0H11	-23 ± 4	10-27	90%	9148	/

The results obtained for the hybrid joints were not comparable with the clearance adhesive samples in terms of absolute value of the amplitude load. In fact, the hybrid joints had a higher statical resistance of about 7000 N more than the clearance ones, so they were expected to begin to suffer the effects of fatigue cycles at higher amplitudes. Nevertheless it was possible to compare the two cases when considering the F_{max} in terms of a percentage of the static resistance of the junction not subjected to fatigue test ($\%SR$).

The comparison of the fatigue behavior of the hybrid and clearance joint is depicted in figure 5.18.
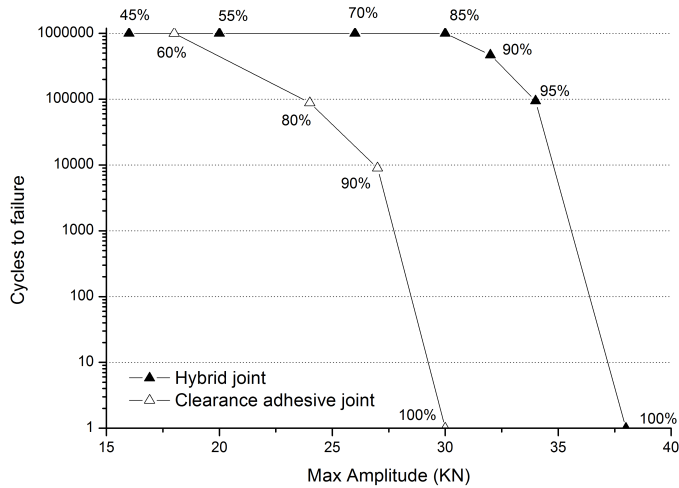

Figure 5.18: Comparison between the attained cycles to failure of hybrid joints and clearance adhesive joints at difference maximum stress amplitudes. The F_{max} in percentage of the total static resistance is indicated for both case.

It could be noted that the hybrid joints underwent the total amount of the fatigue cycles up to a amplitude of about 85%SR. For higher amplitudes, the samples did not pass the test, failing at about half million of cycles at a maximum amplitude of 90 % SR and at the beginning of the test for an amplitude amounting to 95 % SR. On the other hand the adhesive joint in

clearance condition failed around 10000 cycles if stressed with a max amplitude equal to only 80 % SR, and underwent the million cycles at 60 % SR. It seemed that the interference played a beneficial role on the fatigue behavior of the samples, as the hybrid joints managed to sustain 10^6 cycles at amplitudes equal to higher percentages of their static resistance with respect to the clearance joint.

The load recorded in the pull-out test performed on the samples that underwent the total amount of fatigue cycles is analyzed in figure 5.19 for what concern the hybrid joints. A slight strength decay of hybrid joint subjected to fatigue loading emerged by the results. Indeed only the samples that undergo 1 million cycles at a max amplitude of $85\%SR$ showed an appreciable decay in strength (about 6000 N) with respect to the joint not subjected to fatigue.
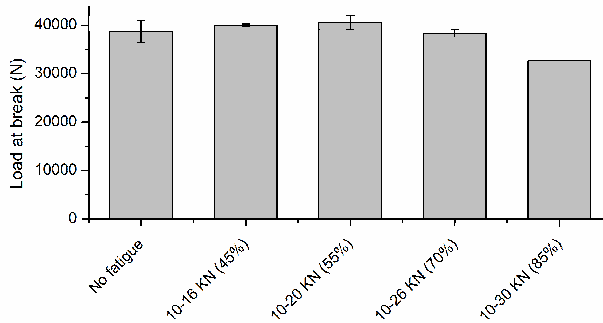

Figure 5.19: Strength decay of hybrid joint after 10^6 fatigue cycles at different force amplitude in respect to their static pull-out strength. The F_{max} in percentage of the total static resistance is also indicated.

Unfortunately, for the clearance joints, the amount of samples tested was not large enough to obtain information on the strength decay of the samples. The samples tested dynamically at 60 % SR showed no appreciable changes in the static pull-out strength after the fatigue cycles. On the contrary the samples tested dynamically at 80 % SR failed already during the fatigue test making impossible the following traction test. Probably the strength decay, if it exists, would happen by testing the sample dynamically at amplitudes in between 60 % SR and 80 % SR.

5.4   Conclusions

- The numerical model and the analytical equations were not influenced by the uncertainty and variability of the measures and could be successfully combined with the experimental data to aid the interpretation of the results.

- The variability of the results related to the unbonded samples was more influenced by the friction effects rather than the interference level.

- A layer of adhesive remained inside the junction for each level of interference tested. The formed layer of adhesive avoided the formation of scratches on the mating area, limiting the friction effects.

- In the case of the interference joints bonded with an epoxy adhesive, the contact pressure contribution to the hybrid joints resistance could be evaluated by the residual load after break. In fact, the load after the break was directly dependent on the pressure between the components without being affected by all the tribological phenomena observed in the unbonded joints. The data collected by the load after the break were in good agreement to the ideal system described by the numerical analysis and analytical equations.

- The maximum strength of an hybrid adhesive joint was highly dependent on the resistance of the adhesive. Though, taking into account the high variability of the data, the linear fit of the experimental points seemed to support the theory of the superimposition of the effects of the contact pressure and the resistance of the adhesive for the epoxy adhesive used.

- The presence of the interference positively affected the fatigue behavior of the cylindrical joint. Hybrid joints sustained 10^6 fatigue cycles at load amplitudes equal to an higher percentage of their static resistance compared to the clearance joint.

Chapter 6

Application of the hybrid joint to the automotive wheel

Abstract

The technology of the interference-fitted adhesive-bonded hybrid joint investigated at the laboratory scale was described in the previous chapters. The technology was transferred on the wheel system to understand if the trends and the key parameters identified at the laboratory scale were verified also in the application case. This chapter firstly describes the assembling of bonded wheel prototypes. Then it reports the results obtained on two types of bonded wheel prototypes from the static standard tests adopted for component validation in MW. Fracture analyses of the bonded area is also reported out. Furthermore an experimental campaign set to understand the role of the fitting force on the hybrid joint in the wheel system is described, including static and dynamic tests carried out for this purpose. The bonding technology was found promising for the wheel system, but its actual joint geometry should be rethought in order to exploit the main advantages of the hybrid bonding technology. In the presence of the actual components design, the bonded area was revealed the most influencing parameter in the static tests on wheels. On the contrary, it played a moderate effect on the fatigue behavior of the samples, where the interference seemed to play a more relevant role.

109

6.1 Bonded wheel prototypes: Preliminary results

Preliminary static tests were conducted on bonded wheel prototypes in order to understand the general structural resistance of the hybrid adhesive joint in the wheel application. Two types of static decoupling tests were performed according to the MW standards: the peel test and the shear test. The results obtained for the bonded prototypes were compared to the data relative to the normal production welded wheel. The test methods and the results are described in this section.

Initially two types of wheel were assembled:

- A passenger car wheel with a nominal diameter of 15 inches. It will be referred as "PCW" in the text.

- A commercial vehicle wheel with a nominal diameter of 16 inches. It will be referred as "CVW" in the text.

The nominal load value of PCW wheels is equal to 500 Kg [3], that is the normal load due to the vehicle weight that acts on the wheel in normal operative conditions. The nominal load value for CVW wheels is 1200 Kg [3].

These values are given in order to provide a general idea of the load sustained by a wheel in normal operative conditions. The standard tests and thresholds described in the following paragraphs involves higher loads, as the tests conditions must be distinctly more severe than the operational ones.

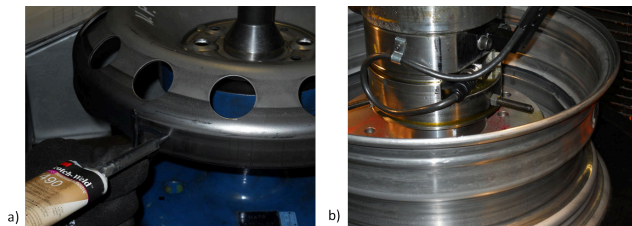The generic nomenclature of the wheel parts used in this chapter is depicted in the Appendix A.

Figure 6.1: Two pictures of the assembly process of the wheel protoypes: (a) the spreading of the adhesive on the disc flange; (b) the press-fit of the components

On the basis of laboratory tests (see Chapter 4) conducted on different adhesives, the rigid and toughened epoxy adhesive Scotch-weld® DP490 was chosen for bonding the first wheel prototypes.

The approach for the assembly of the wheels was set on the procedure employed for the hub/shaft samples. The disc and the rim were collected separately from the production line. The two coupling surfaces, the disc flange and the rim well, were de-greased with acetone. Then the adhesive was spread on both these surface. A spatula was employed for covering the whole size of the disc flange and the rim well, in order to be sure that the adhesive wetted all the coupling area. The components were then press-fitted together according to the production-line procedure. The so formed wheel was left 24 hours at room temperature and thus heated in an oven at 80°C for 1 hour according to the curing protocol of the employed adhesive. Two images related to the assembly operation are reported in figure 6.1.

6.1.1 Peel test on bonded wheel

The peel test is a check requested by some automobile manufacturers for the quality of the weld. The test methodology is described in the scheme reported in figure 6.2. The wheel is simply pressed on the disc nose without any back support or constrains for the rim. Thus the disc and the rim are free to deform plastically and a peeling type stress is created in the junction. The threshold that indicates the end of the test is the deformation of the disc. In the 'traditional' welded wheel the disc has to be deformed plastically before the welds are torn off.
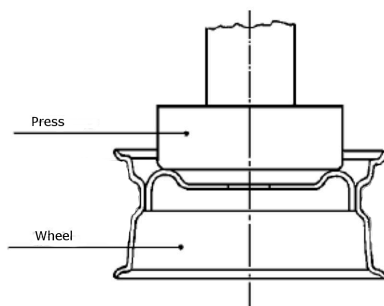

Figure 6.2: Schematic representation of the peel test on wheel [3].

Three prototypes for both the studied wheels were tested. Also two normal production *PCW* welded wheels and one *CVW* were evaluated as reference.

The maximum loads recorded by the pressure switch during the tests are collected in table 6.1, together with the failure modes.

Table 6.1: Peel tests results

Passenger car wheel			Commercial vehicle wheel		
	Mean load (Kg)	Failure mode		Mean load (Kg)	Failure mode
Bonded	14000±1000	Rim and disc deformed	Bonded	21000±3000	Rim bead seat deformed
Welded	15200±200	Disc deformed	Welded	33000	Disc deformed

The bonded *PCW* reached the load range of the welded *PCW* after an important plastic deformation of the steel. Instead the *CVW* system bonded wheel was not able to reach loads comparable to the welded one and the adhesive breakup occurred after slight deformations of the rim. The failure modes were different between bonded and welded wheels. In fact, in the former configuration, the stresses were transferred from the disk to the rim by the bonded area and the rim firstly deformed. At this point, in the case of the passenger car wheel, when the rim was completely compressed also the disc started to bend. In the case of the commercial vehicle wheel, rim and disc are thicker, thus, despite the reached loads were higher, a more limited deformation happened before the breaking of the adhesive. On the other hand, in the welded case the disc is bended upside down until the four weld beads started to be torn off.

Considering that the stresses provided by the normal pressure were not entirely concentrated on the joint area, but were dissipated in multiple deformations of the steel, the usage of the peel test was estimated rather limited. No proper informations could be obtained on the resistance of the glue. As an example, four frames collected by the video of the *PCW* test are arranged in figure 6.3. In this case, the rim was the first to plastically deform, in particular at the bead seat level. Then, as the rim flange was constrain by the ground, the rim well began to fold on itself at the well bottom radius. After the rim was totally compressed, the disc starts to plastically deform. The adhesive breakup took place drastically along all the bond line when the disc nose was already deformed.
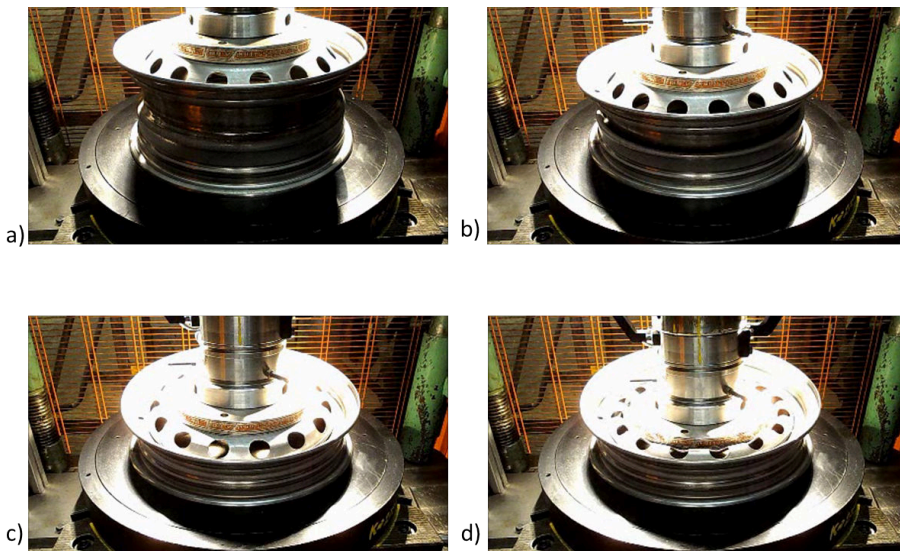
Figure 6.3: Frames collected from the video of the peel test on the bonded passenger car wheel: a) frame at 0s, the beginning of the test; b) frame at 20s, the rim is already deformed at the bead radius level, and the rim well is folding; c) frame at 50s, the rim is totally compressed, the disc nose is starting to bend; d) frame at 1m 03s, the adhesive is broken, end of the test.

6.1.2   Shear test on bonded wheel

The shear test provides more precise information on the shear resistance of the wheel joint. In this test, the disk is pulled out of the rim as in the peel test, but the rim is constraint and cannot be plastically deformed. Also the disk is not able to deform as the load acts on a disk shaped mold placed inside it. Thus avoiding in this way all the plastic deformations, all the stresses are concentrated in the joint area, as can be seen in the schematic representation of figure 6.4.
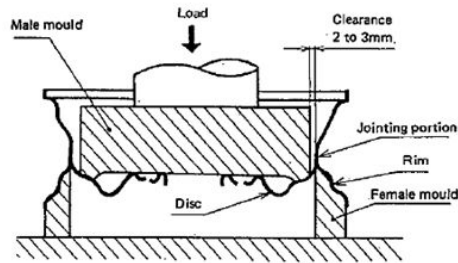
Figure 6.4: Schematic representation of the shear test on wheel [3].

The test is created to test the quality of the welding. The weld resistance must be higher than 30000 Kg. Usually no damage on the weld is recorded at this pressure load on the normal production welded wheel. Instead a little strain of the metal can happen on the rim well.

Three bonded samples were tested for both *PCW* and *CVW* cases. One welded wheel for each case was also tested as reference. The results obtained for the bonded wheels are reported in figure 6.5. The welded wheels passed the test by undergoing 30000 Kg without breaking.

It was possible to notice that the adhesive broke before the 30000 Kg for both the wheel systems. Both the *PCW* and *CVW* wheels reached a static decoupling resistance of about 20000 Kg. The *CVW* wheels reached slightly more elevated performances characterized by an higher variability of the results. The joint area in the *CVW* system was wider than in the *PCW* system. The difference in bonding area was estimated about 68,5 cm^2, according to a wider rim well and a bigger diameter of the *CVW* model.

The results of the shearing test provided good information on the shear-resistance of the bonded joint. Some consideration have to be done on the limit of 30000 Kg. The threshold is set with the purpose to quality check the welding process, and this is not the structural limit fixed for the wheel system.
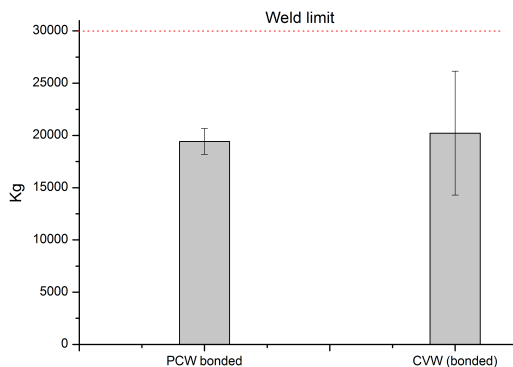
Figure 6.5: Results obtained by the shear test of the bonded wheel. Both the *PCW* case and the *CVW* are depicted.

The decoupling shear load employed in the shear test rarely would happen in normal operative conditions. The radial load that simulate the steer of the vehicle is the more close to a decoupling type of load. In normal operative conditions the lateral load sustained by wheel is far more lower with respect to the limit of 30000 Kg. For instance the loads employed for fatigue rolling tests in order to simulate a harsh operative life of the wheel are more than one order of magnitude less. The combination of radial and lateral loads employed in fatigue analysis of *CVW* wheels is equal to 2280 Kg of radial load and 912 Kg of lateral load. The respective combination for *PCW* wheels is 1000 Kg of radial load and 400 Kg of lateral load. Thus the shear test can be used to compare the static shear resistance of different bonded and welded solutions, not to test the structural resistance of the wheel, according to a load threshold.

6.1.3 Fractographic analysis

The bonded areas of the bonded wheels decoupled during the shear test were examined. Samples of mating surfaces of disc and rim were collected and observed by using an optical and a stereoscopic microscope. Employing a lateral light source that induces shadows on the samples, the stereoscopic microscope provides an image with three dimensional characteristics.

Typical fracture surface images of the bonded area of disc and rim obtained with the stereoscopic microscope are reported in figure 6.6. In order to aid the interpretation of the fracture topography a section of the joint area is depicted in the same figure and the limits of the joint area are also marked.
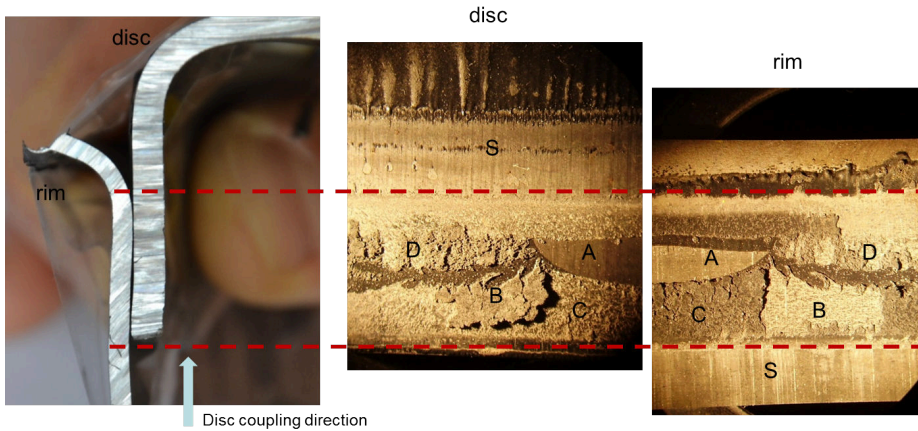

Figure 6.6: Mating fracture surfaces of disc and rim. The areas A, B, C, D and S are identified in both the rim and the disc surfaces. A section of the joint is depicted and the limits of the joint area are marked.

A complex fracture surface could be observed. When the disc was coupled into the rim, the adhesive deposited on both the surface was dragged. The areas identified as S on disc and rim took part in the coupling operation, but at the end of the pressing were outside the final joint. The signs of the dragging were still visible in these areas.

Inside the final joint different areas could be identified. The effects of a mainly cohesive type of fracture were observed in areas B, C and D. For instance, the adhesive remained attached to the disc in the B area left its imprint in the specular B area on the rim. On the other hand, in C area the majority of the adhesive layer remained attached on the rim. In D area both the phenomena were observed as adhesive parts were located on both the surfaces. The area marked with the letter A presented peculiar characteristics. Indeed the layer remained on this area appeared thinner at the stereoscopic microscope than the other layers on both disc and rim. In the closed configuration of the joint the two A areas did not touch each others. Moreover the topography of this

layer did not reveal signs of any type of fracture. Both this characteristic are highlighted in the magnifications in figure 6.7. This A zone could be referred to an air void present inside the joint that ran all along the circumferential bonded area.
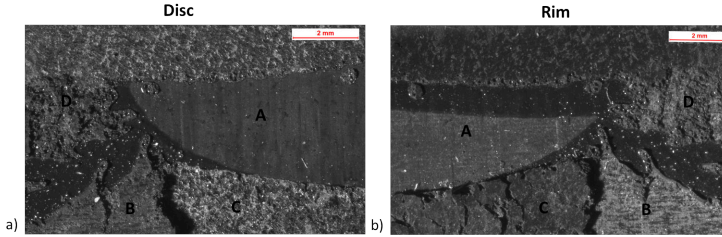

Figure 6.7: Stereoscopic microscope magnifications of the mating fracture surfaces of disc and rim. The areas A, B, C and D S are identified in both the rim and the disc surfaces.

The formation of the air void probably due to the geometry of the joint and in particular to the flange angle, could be argued by the section of the joint presented in figure 6.6. The disc flange is not straight, but it is characterized by an inclination. The extent of this inclination is indicated by the *flange angle* f_α, as depicted in figure 6.8. The inclination of the disc combined with the enlargement of the rim due to plastic deformations created a clearance inside the junction. On the contrary, the extremities of the joint area were characterized by a high interference. The few adhesive dragged in the joint because of the interference was not sufficient to fill the clearance inside it and thus the air void was formed. The formation of the air void was highlighted in the following experiments with different fitting forces, described in section 6.2 of this chapter.
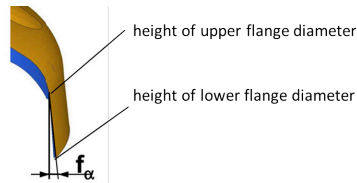

Figure 6.8: Schematic representation of the disc flange inclination identified by the flange angle.

As described in section 6.2, the presence of the air void all along the bonded area could lowering the static performance of the joint. Moreover a correct bonded joint should be designed in order to avoid the creation of systematic defects.

6.2   Influence of the fitting force

An experimental campaign was conducted to evaluate the interaction between the adhesive and the interference level in the wheel system.

A passenger car wheel with a nominal diameter of 15 inches was used. It will be referred as "$PC2W$" in the text. This model of wheel was different from the PCW model used in the preliminary tests.

The methodology followed for the assembly process was the same employed for previous bonded wheel prototypes (described in section 6.1) and it was based on the laboratory set-up for the hub/shaft samples. After receiving discs and rims from the production line, the coupling operation were followed according to the schematic flowchart reported in figure 6.9.

During the assembly, the following parameters were checked: the disc upper flange diameter (UFD), the disc lower flange diameter (LFD), the rim well diameter (RWD), the maximum fitting force recorded (MFF), the fitting force at the end of the coupling ($ETFF$). The load/displacement coupling curves were also recorded during the assembly operation. In order to check the quality of the coupling, the axial runout (AR) of the assembled wheel was measured. The axial runout is the measure of the discrepancy between the maximum and the minimum distance that exist between the disc attachment face and the rim horn [3]. This distance discrepancy is a normal result of a little misalignment of disc and rim. Values of AR inferior to one millimeter are allowed in normal production [3]. The phases of the process where the output data were collected are reported in figure 6.9.

In order to create various levels of fitting force, rims were produced with different rim well diameters. The normal production discs were coupled with the different rims obtaining four separated classes of interference: stronger interference (A), normal production interference (NP), lower interference (B), transition fit (C).

A fifth class of samples was also produced by turning the disc flange in order to eliminate the presence of the flange angle. This class was created in order to understand the effects of the flange angle on the bonded area, including the formation of the air void described in section 6.1.3.
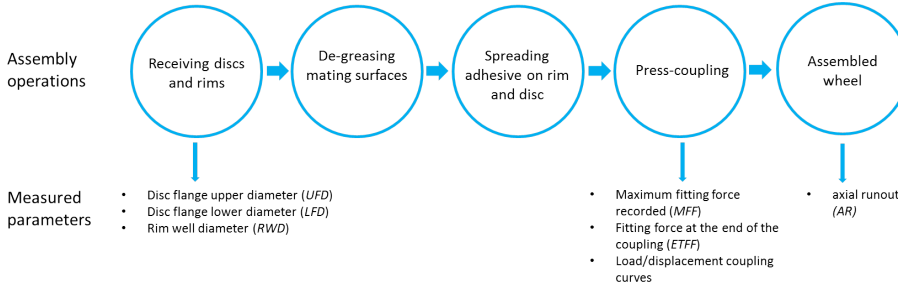
Figure 6.9: Schematic flow-chart of the assembly operations. The parameters measured during every stage of the process are also depicted.

All the interferences and diameters of the classes of samples are collected in table 6.2.

Table 6.2: Diameters and interferences of *PC2W* system

Interference classes	*UFD* (mm)	*LFD* (mm)	*RWD* (mm)	δ with *UFD* (mm)	δ with *LFD* (mm)
case A	339.9 ± 0.1	341.7 ± 0.1	338.6 ± 0.1	≈ 1.3	≈ 3.1
case NP	339.9 ± 0.1	341.7 ± 0.1	339.2 ± 0.1	≈ 0.7	≈ 2.5
case B	339.9 ± 0.1	341.7 ± 0.1	339.8 ± 0.1	≈ 0.1	≈ 1.9
case C	339.9 ± 0.1	341.7 ± 0.1	340.4 ± 0.1	≈ -0.5	≈ 1.3
case TR	339.7 ± 0.1	339.7 ± 0.1	338.6 ± 0.1	≈ 1.1	≈ 1.1

6.2.1 Coupling behaviour

The coupling load/displacement curves of the bonded wheels were collected during press-fitting. The curves of the A, B and C hybrid systems and of the relative unbonded wheels are reported in figure 6.10.

The comparison shown in figure 6.10 revealed a good repeatability of the coupling process among the samples at the same interference level. Moreover the presence of the adhesive did not modify the coupling behavior of the wheels as the curves of the bonded systems were coincident with the non-bonded ones. The glue did not imply an increase in the coupling force, but at the same time
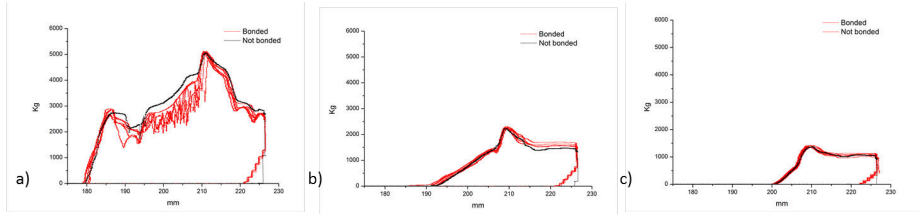
Figure 6.10: Comparison among the coupling curves of bonded and unbonded wheels of the different fitting-force cases: a) fitting case A, with a strong interference, b) fitting case B, with a low interference, c) fitting case C, with a transition fit.

it was not able to act as a lubricant. Only in the central part of the coupling of the A system, a stick-slip proceeding could be observed in bonded samples, probably imputable to the high interference level.

For each case study the coupling curves were averaged for obtaining a representative mean curve, also applying a smoothing filter. The mean load/displacement curves are compared in figure 6.11.

The level of interference strongly influenced the coupling curves. All the samples, excluding the TR cases, were assembled by using the same discs having the same flange angle. Thus two level of interference were calculated for the *UFD* and the *LFD* as reported in table 6.2. The A, NP, B and C cases were differentiated from each other by a jump of 0.6 mm of interference. This rate of increasing the interference from case C to case A could be observed in the different height of the peak at 210 mm of the coupling curves. Indeed the height of this peak increased of about the same amount from case C to case A. This peak at 210 mm was due to the entrance in the rim well of the larger end of the disc flange, thus at the level of the *LFD*. On the contrary, the peak of the entrance of the thinner upper part of the disc flange was visible at 185 mm only for the case A and NP. Indeed the interference level at the *UFD* was practically inexistent in the B case (0.1 mm), corresponding to a very smooth peak. For what concern the C case, a clearance was present between the upper part of the flange and the rim well, thus no loads were recorded at that displacement.

The situation was different for the TR case. The flange angle was removed and the resultant disc flange appeared straight. Thus the contact with the rim well was more homogeneous during all the coupling. This type of contact produced an elevated and quite constant load during all the coupling, considering
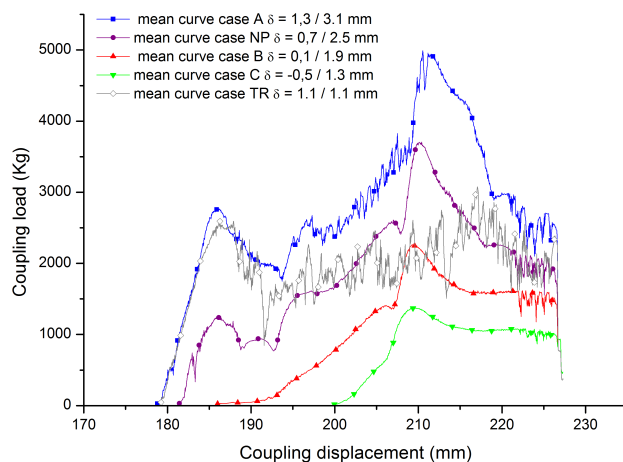
Figure 6.11: Comparison among the mean coupling curves of bonded wheels for the different fitting-force cases.

the mean of the stick-slip peaks. The strong stick-slip behavior could be partially imputed to the high circumferential roughness produced by the turning operation as highlighted in figure 6.12.

Figure 6.12: Roughness on the disk flange of the TR case, due to the turning operation .

The high stick-slip behavior observed in the turned wheel leads to misalignments between the disc and the rim. Indeed the mean axial runout measured for the TR wheel is 2.2 ± 0.7 mm, decisively higher than the mean values measured for all the other samples of the cases A, B, C and NP (0.9 ± 0.4 mm).

6.2.2   Shear test and fractographic analysis

Five bonded wheels for the cases A, B and C, three for the cases NP and two for the TR were submitted to the shear test, according to the methodology described in section 6.1.2.

On the basis of the tests conducted at laboratory scale, the increase of the interference should imply an increment in the shear strength. On the contrary, from the shear tests on bonded wheels an opposite trend was recorded, as illustrated in figure 6.13 where the shear strength is plotted against the maximum fitting force.
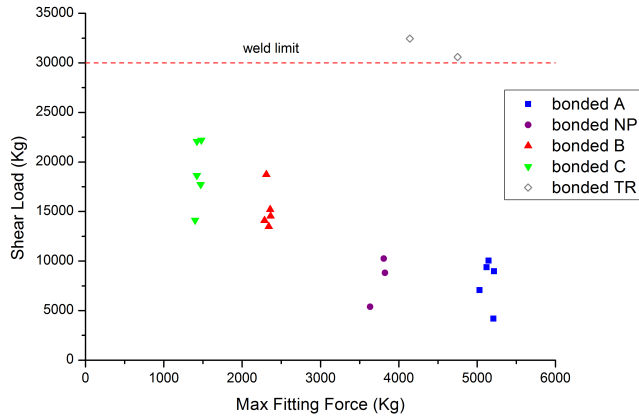

Figure 6.13: Shear test results of bonded wheels joined with different interference systems.

The shear decoupling load of the C case (the transition fit) was the highest among the samples with the non-modified disc flange. On the contrary, the A case, characterized by the highest interference, showed the poorest results. Instead, considering the modified disc flange, the TR wheels showed the best shear resistance, higher than the threshold set for the weld.

The reason of these unexpected results was explainable through the fractographic analysis of the wheel bonded areas.

Discs and rims were then cut and analyzed at the optical microscope. The fracture surfaces samples are illustrated in figure 6.14.
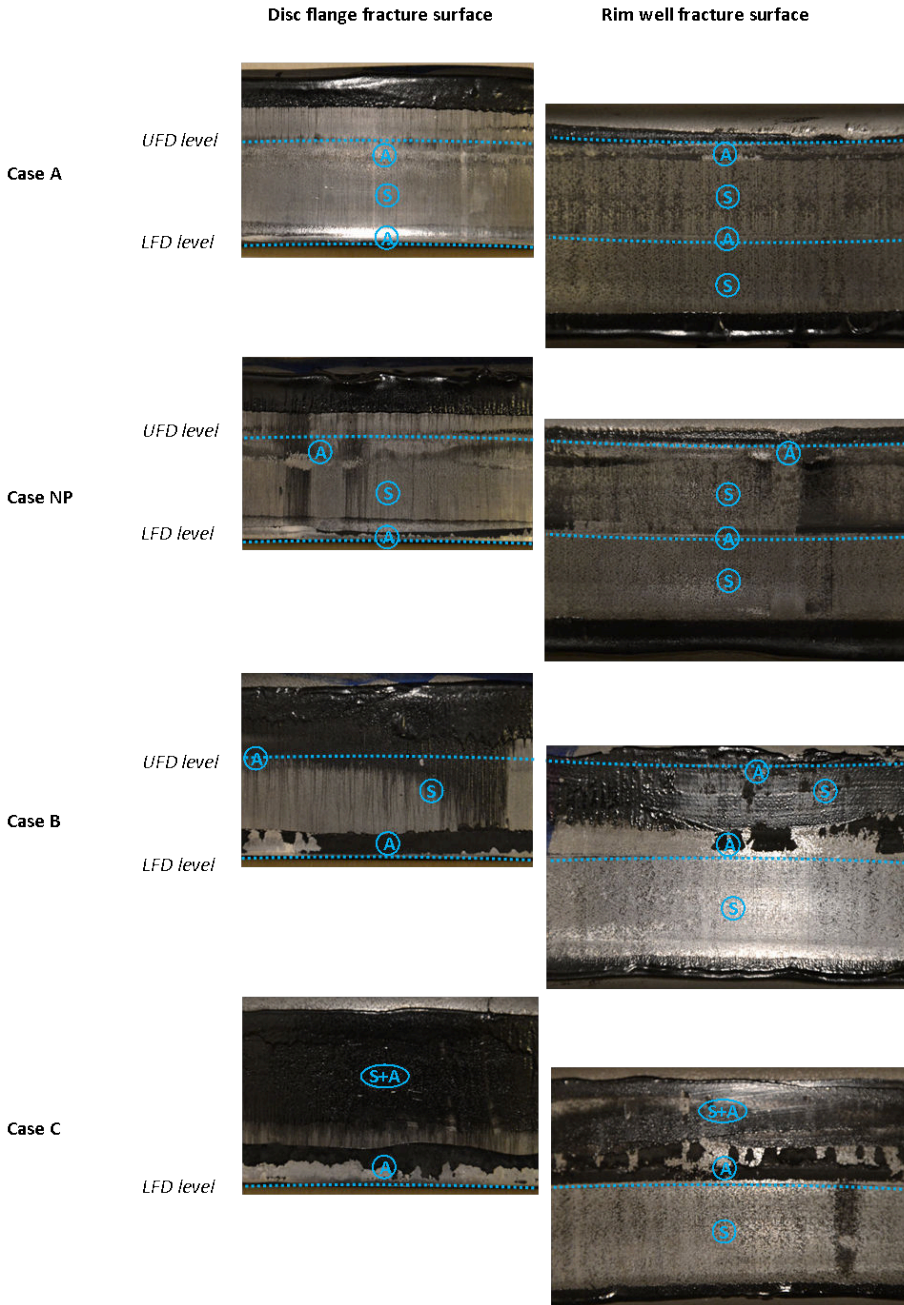
Figure 6.14: Mating surfaces of discs and rims joined with different interference levels after the shear test. Areas indicated with letter A present clear signs of fracture surface. Areas indicated with letter S does not present signs of fracture.

The mating surfaces of disc and rim of the A case presented very few adhesive residues inside the joint. Moreover, the adhesive showed a clear fracture surface not in the whole mating area, but only in restricted circumferential stripes at the height of *UFD* and *LFD*. These zones were indicated with the A letter in figure 6.14. The rest of the mating area did not present clear signs of fracture and it was similar in topography to the area of the rim well that remained outside of the joint, where the adhesive was dragged but there was not contact with the other surface. These areas were identified with the letter S in figure 6.14. Thus, it seemed that the only contact points between the surfaces of disc and rim were at the level of *UFD* and *LFD*. According to this interpretation a very few contact area involving adhesive and interference was present in the case A. This situation seemed similar to the one observed in previous fractographic tests (see figure 6.6), but here the majority of the mating area represented the non-contact area.

The mating surfaces of disc and rim for the NP case showed a situation similar to the A case. Here, the two contact areas corresponding to the *UFD* and *LFD* were wider than in A case. Due to the less strong interference, more adhesive could be found in correspondence with the contact points.

A different situation could be observed in the B samples that were characterized by a wider fracture surface at the height of the *LFD*. On the other hand, the upper part of the contact was barely visible. An important quantity of adhesive reached to flow inside the junction during the press-fit thank to the lower interference at the *UFD*. The adhesive was then accumulated in the end of the joint gathered by the *LFD* interference. The non-contact area was present, but with reduced dimensions. On the disc side, it was possible to observe the dragged adhesive in the non-contact area, marked with the letter S.

The case C presented characteristics similar to the case B. In this case there was a clearance at the *UFD* level, indeed it was impossible to identify a clear point of contact in the upper part of the joint. The contact and non-contact areas between the mating surfaces were mixed together: it is possible to detect parts of fracture surfaces and parts where the adhesive was clearly cured without contact with the opposite surfaces. In the lower part of the joint, a wide fracture surface could be noted. The adhesive gathered by the interference at the *LFD* level was more than in the B case.

The higher loads reached in shear in the case C seemed plausible considering the quantity of glue that actually formed the bonded joint inside the mating surfaces. The adhesive contribution could be considered higher in the C and B samples than in the NP and A cases. Because of the particular joint geometry, an higher *UFD* interference level limited the adhesive penetration inside

the joint. Consequently higher interference samples showed less shear strength values because characterized by a considerably lower adhesive contribution.

The behavior of the TR samples confirmed this hypothesis. The TR samples presented a more simple fracture surface, illustrated in figure 6.15a. The whole mating area of both the disc and the rim was characterized by the presence of cured adhesive particles. Also the areas outside the joint, marked with the letter S, presented cured adhesive particles dragged during the press-fit. The different light reflection allowed to clearly discern the fracture surface by the dragged adhesive cured outside the joint. Indeed all the mating area was characterized by a fracture surface.
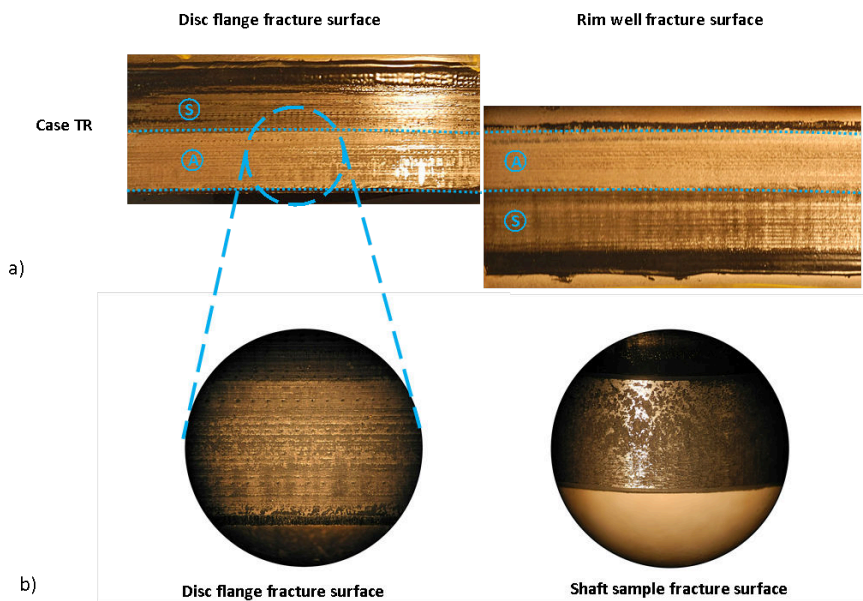

Figure 6.15: a) Mating surfaces of disc and rim from TR samples after the shear test. Areas indicated with letter A present clear signs of fracture surface. Areas indicated with letter S does not present signs of fracture. b) Magnification of the fracture surface of the TR disc flange compared to that of a hub/shaft sample with an interference of 35 μm.

A similar fracture surface was detected in the hub/shaft samples used in laboratory tests described in Chapter 5. In figure 6.15b a magnification of the

fracture surface of the disc is compared to a magnification of the fracture surface of a shaft of a sample with an interference of 35 μm. Both the fracture surfaces presented a uniform presence of small cured adhesive particles.

The contribution of adhesive and interference acted in these samples on the same wide joint area. The absence of the flange angle permitted a more uniform flow of the adhesive inside the joint. Indeed the TR joints reached the highest shear resistance, higher than the quality limit fixed for the welded joints.

6.2.3   Fatigue behavior

The rolling test was employed to simulate the fatigue stress to which the wheel is subjected during its operating life on vehicles. In this test the wheel is placed on a roller to undergo rolling cycles. The machine is able to apply a radial load and a lateral load to simulate the use on vehicles, with a constant monitoring of these parameters during the test.
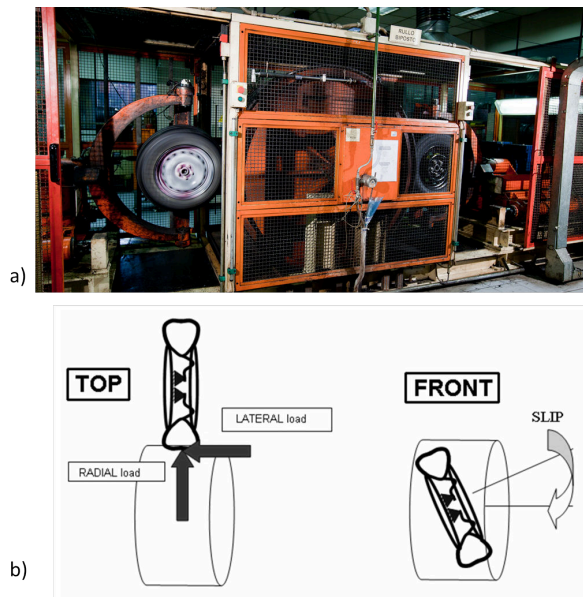

Figure 6.16: The rolling test on wheels: a) picture of the test machine [3] b) loading scheme [3]

A picture of the test machine is depicted in figure 6.16a with its loading scheme (6.16b). The machine is equipped with devices for the automatic stop in case of failure of the wheel under test, such as accelerometers and linear transducers.

Considering the long times of tests (two or three days for each one), only some bonded wheels were examined (the rolling machines present in MW laboratory were not always available, being exploited to verify the production components).

The fatigue cycle parameters were chosen on the basis of the most harsh standard fatigue test for the $PC2W$ wheel: a radial load of 1020 Kg combined with a lateral load of 408 Kg. According to specifications [3] the speed of the test should be set in a range between 25 Km/h and 70 Km/h. Changing the speed inside this range does not affect the fatigue behavior. The only reported influence of the speed is when it triggers heating phenomena or resonance frequencies that can affect the fatigue response [3]. The speed of the test was set to 50 Km/h, a standard value for the $PC2W$ wheel. According to the quality protocol [3], the 90% of the normal production wheel should undergo a minimum number of cycles of 330 000. This type of limit is commonly used in reliability engineering and is based on Weibull statistic distribution [98].

According to MW experience [3] the "traditional" welded wheel extensively overcome the minimum number of cycles, reaching more than 1.5 millions of cycles without breaking.

In particular, two bonded wheels were tested: one from the B case, and one from the C case. Both the wheel passed the test and they underwent without breakages 1 620 000 and 1 583 000 cycles, respectively.

In order to obtain comparable data in a reasonable time, it was decided to further increase the loads of the test of 15%. The radial load was then fixed to 1173 Kg and the lateral one to 470 Kg. According to these new values, the speed of the test was reduced to 30 Km/h for safety purpose in the case of decoupling of disc and rim, and for reducing the wear of the tires.

Two bonded and two welded wheels for the cases A, B and C were tested in these conditions. The obtained results are reported in figure 6.17.

The results obtained from the fatigue tests showed a peculiar situation. There was not great difference between the behavior of the welded and the bonded wheels. Nevertheless a high variability of the data was recorded for the welded wheels. According to MW experience [3] this high dispersion could be referred to the quality of the welding.

A linear relationship between the interference and the fatigue resistance was not recorded for both the welded and the bonded wheels. Instead, it seemed that
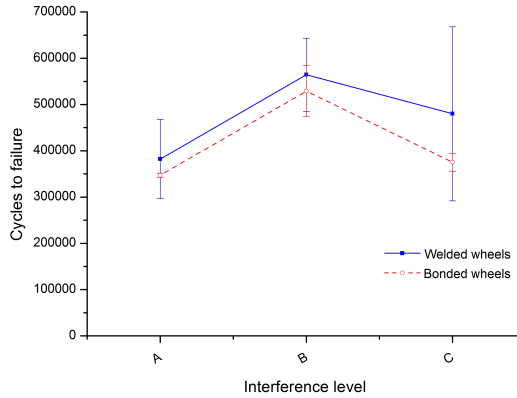
Figure 6.17: Results of the rolling tests of A, B and C wheels with the radial and lateral loads augmented of 15%

both the systems reached an apex of their fatigue resistance in correspondence with the case B (low interference level). The wheels characterized with higher interference levels (case A) and transition fits (case C) failed at lower number of cycles.

The presence of an optimum of the interference level for obtaining the best fatigue behavior was already hypothesized by MW technicians for the 'traditional' welded wheels. Moreover, modal analysis conducted by the Department of Management and Production Engineering (DIGEP) of the Politecnico di Torino with MW spa showed that there was a relationship between the interference level and the frequencies of the wheel. On these basis, it was reasonable to suppose that the frequency and stiffness of the component could play a role in determining the fatigue behavior. The influence of the interference on the stiffness of the hybrid joint was demonstrated in the laboratory tests (see Chapter 4).

For all the tested wheels a similar disc failure type was observed. According to MW experience [3], this type of failure was probably due to the increased tested loads. The disk failure is a not-desirable drastic type of failure in which a crack starts at the disc window and it propagates towards the joint area. When the crack reaches the joint area, the disc is not able to provide the interference level, thus all the stresses are concentrated on the welding or the adhesive, inducing in this way the wheel failure. An example of a disc failure on a welded

wheel is reported in figure 6.18.

The failure of the welded joint was usually less drastic then the failure of the adhesive one. Regarding the welded wheels, in the 50 % of cases the damage was revealed by the loss of air of the tire from the weld bead. In the other 50 % (mainly from A and C cases), all four welded beads were torn off and the wheel was decoupled. For what concern all the bonded wheels, when the adhesive failed the wheel was decoupled.
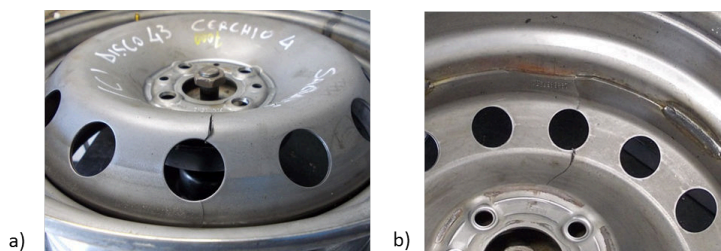

Figure 6.18: Failure mode common to all the samples tested to fatigue rolling. The crack, started by a disc window, reaches the joint area inducing the wheel decoupling

Two TR bonded wheels were also checked with the rolling test. The mean of their withstood cycles was 326000 ± 26000. Thus, even if the TR wheels presented the best performances in the decoupling test, a failure at a relatively low number of cycles was recorded. The interference level in this case was equal to 1.1 mm at both the *UFD* and the *LFD* levels and the type of contact was different from the other cases because of the removed flange angle. The stress distribution in this joint was then different, and no comparison in terms of the interference level was possible with the other systems. Moreover these wheels were characterized by higher values of axial runout, that could be also detected by the swaying of the TR wheels during rolling. Despite there were too few data for underline a trend, this parameter could also have influenced the fatigue test results of the TR wheels.

Notwithstanding these results, the preliminary tests carried out in this PhD thesis were not sufficient to evaluate the optimization of the bonded joint through the modification of the wheel design. For instance, no tests were carried out on turned-and-welded wheels as reference or on TR wheels with different interference degrees.

Considering the limited number of fatigue tests conducted, it was reasonable

to state that the shear resistance of the bonded wheel and its fatigue behavior were not correlated. In fact, the C and TR case that showed the best performances in static shear did not present also the best fatigue behavior. While the size of the bonded area seemed to govern the decoupling resistance, the interference seemed to play the biggest role in ruling the fatigue behavior.

6.3   Conclusions

- The tested configurations of bonded wheels showed similar performances with respect to the welded systems.

- The hybrid solution required the optimization of the joint geometry and the interference level.

- The following trends were recorded when an adhesive is exploited with the actual design of the wheel component.

  - The behaviour of the wheel loaded in static shear was mainly dependent on the extent of the bonded area.

  - The fatigue behaviour of the wheel seemed to be independent from its static resistance. Among the different variables able to influence the system, the interference seemed to play an important role.

- Appling the adhesive after removing the flange angle could:

  - provide a better distribution of the adhesive in the joint area inducing better static performances.

  - increase the stick-slip behaviour in coupling operations resulting in an high axial runout in the assembled wheel.

  - compromise the fatigue performances, although no data at different interference levels were collected.

Conclusions and future perspective

This thesis demonstrated that the resultant strength of the examined hybrid joint was not always a result of the sum between the adhesive resistance and the interference contribution. The experiments carried out at laboratory level showed that different adhesive types provided dissimilar behaviors in the hybrid system. Indeed, a major influence of the adhesive on the maximum strength attainable for the hybrid joint was observed. Rheology of adhesive played a relevant role in determining how much adhesive was spewed away from the joint. If a few quantity of adhesive remained inside the joint the adhesive contribution resulted lowered, also affecting the total resistance of the hybrid joint. The exploitation of adhesives with different flexibility did not provide changes in the stiffness of the hybrid system, that seems rather dependent on the interference.

The flexibilized and thoughened epoxy adhesives that showed the best performances was chosen for further laboratory tests and for wheels prototyping. In the case of this adhesive an enhancement of the resistance of the hybrid joint was recorded by increasing the interference. The effect of the interference contribution could be more easily detected in this hybrid joints by considering the load recorded after the breakup of the adhesive. The enhancement provided by the interference contribution seemed to present the same rate of enhancement recorded for the total resistance of the hybrid joint, suggesting a superposition of the effects for this adhesive type. However the high variability introduced by the adhesive contribution must be taking into account. A layer of the adhesive remained inside the joint at each interference level tested, avoiding wear and friction effects.

In the wheel system the hybrid joint was mainly affected by the joint geometry. The presence of the disc flange angle and the deformability of the rim well

created zones of clearance inside the joint. The quantity of adhesive penetrated inside the joint depended on the interference level: the more the interference the less the quantity of adhesive penetrated inside the clearance. The extent of the bonded area played a relevant role on the total static resistance of the hybrid joint. Turned wheels with a wider and more uniform contact area showed the best performances in decoupling test. On the contrary, the fatigue life of the bonded wheels seemed to be independent to its resistance to the decoupling. The interference level presented a more relevant impact in this case.

In conclusion adhesive bonding was found a promising technique for joining wheels. Without changes in the component design, bonded solution showed similar performances with respect to the welded one. Adjustment in design should be studied in order to avoid clearance zones inside the joint, but maintaining a certain degree of interference between the components.

Further studies has to be carried out to evaluate the durability of the hybrid system under the operative environmental conditions. In this sense a proper pre-treatment of the surface to be bonded should be taken into consideration.

Bibliography

[1] Steelworks, the online resource for steel.

[2] Automotive news.

[3] M.W. Italia Spa. Archive.

[4] D.A. Dillard. *Advances in structural adhesive bonding.* CRC Press, 2010.

[5] S.T. Amancio-Filho and J.F. Dos Santos. Joining of polymers and polymer–
metal hybrid structures: Recent developments and trends. *Polymer Engi-
neering & Science*, 49(8):1461–1476, 2009.

[6] E. M. Petrie. *Handbook of adhesives and sealants.* McGraw-Hill, 2000.

[7] R.D. Adams, J. Comyn, and W.C. Wake. *Structural adhesive joints in
engineering.* Springer, 1997.

[8] A. J. Kinloch. *Adhesion and adhesives: science and technology.* Chapman
and Hall, 1987.

[9] L.F.M. da Silva and A. Pirondi. *Hybrid adhesive joints*, volume 6. Springer,
2011.

[10] E. Dragoni and P. Mauri. Science of friction–adhesive joints. In *Hybrid
Adhesive Joints*, pages 201–225. Springer, 2011.

[11] J. Abenojar, Y. Ballesteros, J.C. del Real, and Martinez M.A. Pin-and-
collar test method. In *Testing Adhesive Joints: Best Practices*, pages 155–
160. Wiley-VCH.

[12] F. Kleiner and W. Fleischmann. Technologies of threadlocking and interference-fit adhesive joints. In *Hybrid Adhesive Joints*, pages 227–255. Springer, 2011.

[13] E. Dragoni and P. Mauri. Intrinsic static strength of friction interfaces augmented with anaerobic adhesives. *International journal of adhesion and adhesives*, 20(4):315–321, 2000.

[14] D. Castagnetti and E. Dragoni. Predicting the macroscopic shear strength of adhesively-bonded friction interfaces by microscale finite element simulations. *Computational Materials Science*, 64:146–150, 2012.

[15] D. Croccolo, M. De Agostinis, and N. Vincenzi. Static and dynamic strength evaluation of interference fit and adhesively bonded cylindrical joints. *International Journal of Adhesion and Adhesives*, 30(5):359–366, 2010.

[16] M. Yoneno, T. Sawa, K. Shimotakahara, and Y. Motegi. Axisymmetric stress analysis and strength of bonded shrink-fitted joints subjected to push-off forces. *JSME international journal. Series A, mechanics and material engineering*, 40(4):362–374, 1997.

[17] T. Sawa, M. Yoneno, and Y. Motegi. Stress analysis and strength evaluation of bonded shrink fitted joints subjected to torsional loads. *Journal of adhesion science and technology*, 15(1):23–42, 2001.

[18] T. Sekercioglu, A. Gulsoz, and H. Rende. The effects of bonding clearance and interference fit on the strength of adhesively bonded cylindrical components. *Materials & design*, 26(4):377–381, 2005.

[19] R. Mengel, J. Häberle, and M. Schlimmer. Mechanical properties of hub/shaft joints adhesively bonded and cured under hydrostatic pressure. *International journal of adhesion and adhesives*, 27(7):568–573, 2007.

[20] A. Oinonen and G. Marquis. Shear decohesion of clamped abraded steel interfaces reinforced with epoxy adhesive. *International Journal of Adhesion and Adhesives*, 31(6):550–558, 2011.

[21] S. Wu. *Polymer interface and adhesion*. CRC Press, 1982.

[22] J. Comyn. *Adhesion science*, volume 13. Royal Society of Chemistry, 1997.

[23] L.-H. Lee. The chemistry and physics of solid adhesion. In *Fundamentals of Adhesion*, pages 1–86. Plenum Press, 1991.

[24] F. Awaja, M. Gilbert, G. Kelly, B. Fox, and P. J. Pigram. Adhesion of polymers. *Progress in polymer science*, 34(9):948–968, 2009.

[25] D. Arrowsmith. *Transactions of the institute of metal finishing*, 48:88, 1970.

[26] H. Onusseit, R. Wefringhaus, G. Dreezen, J. Wichelhaus, J. Schall, L. Thiele, and A. van Halteren. Adhesives, 1. general. In *Ullmann's Encyclopedia of Industrial Chemistry*. Wiley-VCH.

[27] S.S. Voiutskii. *Autohesion and adhesion of high polymers*. Wiley, 1963.

[28] R.M. Vasenin. Adhesion, fundamentals and practice. *Ministry of Technology, MacLaren, London*, 1969.

[29] B.V. Derjaguin and V.P. Smilga. Adhesion, fundamentals and practice. *Ministry of Technology, MacLaren, London*, 1969.

[30] D. Hays. Role of electrostatics in adhesion. In *Fundamentals of Adhesion*, pages 249–278. Plenum Press, 1991.

[31] L.H. Sharpe and H. Schonhorn. Surface energetics, adhesion, and adhesive joints. *Adv. Chem. Ser*, 43:189–201, 1964.

[32] F.M. Fowkes. *Chemistry and physics of interfaces*. Am. Chem. Soc.,, 1965.

[33] W. Gutowski. Thermodynamics of adhesion. In *Fundamentals of adhesion*, pages 87–135. Springer, 1991.

[34] F.M. Fowkes. Acid-base interactions in polymer adhesion. *Microscopic Aspects of Adhesion and Lubrication*, 1:119, 1982.

[35] R. David, J. Spelt, J. Zhang, and D. Kwok. Contact angles and solid surface tensions. In *Applied Surface Thermodynamics*, pages 491–554. CRC Press, 2010.

[36] I. Stewart, A. Chambers, and T. Gordon. The cohesive mechanical properties of a toughened epoxy adhesive as a function of cure level. *International Journal of Adhesion and Adhesives*, 27:277–287, 2007.

[37] E. Thomas. Polymer physics course, mit opencourseware.

[38] O. Volkersen. Die nietkraftverteilung in zugbeanspruchten nietverbindungen mit konstanten laschenquerschnitten. *Luftfahrtforschung*, 15(1/2):41–47, 1938.

[39] X. He. A review of finite element analysis of adhesively bonded joints. *International Journal of Adhesion and Adhesives*, 31(4):248–264, 2011.

[40] L.F.M. da Silva and R.D.S.G. Campilho. *Advances in numerical modelling of adhesive joints*. Springer, 2012.

[41] L.D.R. Grant, R.D. Adams, and L.F.M. da Silva. Experimental and numerical analysis of single-lap joints for the automotive industry. *International Journal of Adhesion and Adhesives*, 29(4):405–413, 2009.

[42] S. Mostovoy and E Ripling. In *Adhesion science and technology*, volume 1. Plenum Publishing Corporation, 1975.

[43] A. Matting and U. Draugelates. Die schwingfestigkeit von metallklebverbindungen. *Adhäsion*, 1:5–22, 1968.

[44] T. B. Jones and N. Williams. In SAE, editor, *SAE International Congress and Exposition*, 1986.

[45] G.L. Schneberger. *Adhesives in manufacturing*, volume 11. CRC Press, 1983.

[46] T. Sadowski and T. Balawender. Technology of clinch–adhesive joints. In *Hybrid Adhesive Joints*, pages 149–176. Springer, 2011.

[47] E. Chirone and S. Tornincasa. *Disegno Tecnico Industriale, 2*. Edizioni Il Capitello, 2004.

[48] D. Croccolo, M. De Agostinis, and P. Mauri. Influence of the assembly process on the shear strength of shaft-hub hybrid joints. *International Journal of Adhesion and Adhesives*, 44:174–179, 2013.

[49] Henkel Ag & Co. KGaA. *Henkel Product Selector, issue 2*.

[50] C. O'Reilly. Designing bonded cylindrical joints for automotive applications, paper 900776. In SAE, editor, *SAE International Congress and Exposition*.

[51] F. Mahon. Use of anaerobic adhesives to enhance strength and capacity of flanged couplings, paper 950125. In SAE, editor, *SAE International Congress and Exposition*.

[52] H. Kawamura, T. Sawa, M. Yoneno, and T. Nakamura. Effect of fitted position on stress distribution and strength of a bonded shrink fitted joint subjected to torsion. *International journal of adhesion and adhesives*, 23(2):131–140, 2003.

[53] E. Dragoni and P. Mauri. Cumulative static strength of tightened joints bonded with anaerobic adhesives. *Proceedings of the Institution of Mechanical Engineers, Part L: Journal of Materials Design and Applications*, 216(1):9–15, 2002.

[54] D. Castagnetti and E. Dragoni. Experimental assessment of a micromechanical model for the static strength of hybrid friction-bonded interfaces. *The Journal of Adhesion*, 89(8):642–659, 2013.

[55] D. Croccolo, M. De Agostinis, and N. Vincenzi. Experimental analysis of static and fatigue strength properties in press-fitted and adhesively bonded steel–aluminium components. *Journal of Adhesion Science and Technology*, 25(18):2521–2538, 2011.

[56] A. Oinonen and G. Marquis. A parametric shear damage evolution model for combined clamped and adhesively bonded interfaces. *Engineering Fracture Mechanics*, 78(1):163–174, 2011.

[57] T. Sekercioglu. Shear strength estimation of adhesively bonded cylindrical components under static loading using the genetic algorithm approach. *International journal of adhesion and adhesives*, 25(4):352–357, 2005.

[58] E. Dragoni. Fatigue testing of taper press fits bonded with anaerobic adhesives. *The Journal of Adhesion*, 79(8-9):729–747, 2003.

[59] M.F. Ashby, H. Shercliff, and D. Cebon. *Materials: engineering, science, processing and design*. Butterworth-Heinemann, 2009.

[60] K.L. DeVries and D.O. Adams. Mechanical testing of adhesive joints. In *The Mechanics of Adhesion*, pages 193–234. Elsevier.

[61] S. Moane, D.P. Raftery, M.R. Smyth, and R.G. Leonard. Decomposition of peroxides by transition metal ions in anaerobic adhesive cure chemistry. *International journal of adhesion and adhesives*, 19(1):49–57, 1999.

[62] L.F.M. da Silva, D.A. Dillard, B. Blackman, and R.D. Adams. *Testing Adhesive Joints: Best Practices.* Wiley-VCH, 2013.

[63] Astm d1002 - 01. standard test method for apparent shear strength of single-lap-joint adhesively bonded metal specimens by tension loading (metal-to-metal).

[64] Astm d5656-01 standard test method for thick-adherend metal lap-shear joints for determination of the stress-strain behavior of adhesives in shear by tension loading.

[65] Astm d950 - 03. standard test method for impact strength of adhesive bonds.

[66] Astm d3433-99 standard test method for fracture strength in cleavage of adhesives in bonded metal joints.

[67] Astm d5041-98 standard test method for fracture strength in cleavage of adhesives in bonded joints.

[68] Astm d1876 - 01. standard test method for peel resistance of adhesives (t-peel test).

[69] Astm d6862 - 03. standard test method for 90 degree peel resistance of adhesives.

[70] Astm d4562 - 01 standard test method for shear strength of adhesives using pin-and-collar specimen.

[71] En 15337:2007. adhesives. determination of shear strength of anaerobic adhesives using pin-and-collar specimens.

[72] D. Hull. *Fractography: observing, measuring and interpreting fracture surface topography.* Cambridge University Press, 1999.

[73] S.J. Marshall, S.C. Bayne, R.t Baier, A.P. Tomsia, and G.W. Marshall. A review of adhesion science. *dental materials*, 26(2):e11–e16, 2010.

[74] D.A. Aronovich, A.F. Murokh, A.P. Sineokov, and Z.S. Khamidulova. Study of the properties of anaerobic adhesives cured in cylindrical joints. *Polymer Science Series D*, 1(4):260–265, 2008.

[75] G. Gallio, G. Marcuccio, E. Bonisoli, S. Tornincasa, D. Pezzini, D. Ugues, M. Lombardi, D. Rovarino, P. Fino, and L. Montanaro. Study of the interference contribution on the performance of an adhesive bonded press-fitted cylindrical joint. *International Journal of Adhesion and Adhesives*, 2014.

[76] G. Gallio, M. Lombardi, D. Rovarino, P. Fino, and L. Montanaro. Influence of the mechanical behaviour of different adhesives on an interference-fit cylindrical joint. *International Journal of Adhesion and Adhesives*, 47:63–68, 2013.

[77] Iso 9664. adhesives – test methods for fatigue properties of structural adhesives in tensile shear.

[78] T.H. Hsieh, A.J. Kinloch, K. Masania, A.C. Taylor, and S. Sprenger. The mechanisms and mechanics of the toughening of epoxy polymers modified with silica nanoparticles. *Polymer*, 51(26):6284–6294, 2010.

[79] S. Bhowmik, R. Benedictus, J.A. Poulis, H.W. Bonin, and V.T. Bui. High-performance nanoadhesive bonding of titanium for aerospace and space applications. *International Journal of Adhesion and Adhesives*, 29(3):259–267, 2009.

[80] L. Zhai, G. Ling, J. Li, and Y. Wang. The effect of nanoparticles on the adhesion of epoxy adhesive. *Materials Letters*, 60(25):3031–3033, 2006.

[81] M. May, H.M. Wang, and R. Akid. Effects of the addition of inorganic nanoparticles on the adhesive strength of a hybrid sol–gel epoxy system. *International Journal of Adhesion and Adhesives*, 30(6):505–512, 2010.

[82] E. Sancaktar and J. Kuznicki. Nanocomposite adhesives: Mechanical behavior with nanoclay. *International Journal of Adhesion and Adhesives*, 31(5):286–300, 2011.

[83] A. Hartwig, A. Lühring, and J. Trautmann. Spheroidal nanoparticles in epoxide-based adhesives. *Macromolecular Materials and Engineering*, 294(6-7):363–379, 2009.

[84] S. Yu, M.N. Tong, and G. Critchlow. Use of carbon nanotubes reinforced epoxy as adhesives to join aluminum plates. *Materials & Design*, 31:S126–S129, 2010.

[85] Loctite Corporation. *Hysol® 9492, Technical Data Sheet.*

[86] 3M United Kingdom PLC. *Scotch-Weld® EPX Adhesive DP490, Product Data Sheet.*

[87] B. George, Y. Grohens, F. Touyeras, and J. Vebrel. New elements for the understanding of the anaerobic adhesives reactivity. *International journal of adhesion and adhesives*, 20(3):245–251, 2000.

[88] Loctite Corporation. *Loctite® 620, Technical Data Sheet.*

[89] G. Malucelli, A. Priola, F. Ferrero, A. Quaglia, M. Frigione, and C. Carfagna. Polyurethane resin-based adhesives: curing reaction and properties of cured systems. *International Journal of Adhesion and Adhesives*, 25(1):87–91, 2005.

[90] Huntsman Corporation. *Araldite® 2029 Structural Adhesives, Technical Data Sheet.*

[91] F.P. Bowden and D. Tabor. The friction and lubrication of solids. 1950.

[92] 3M Company. *3M^{TM} Scotch-Weld^{TM} EPX.*

[93] Huntsman Corporation. *AdMat Araldite® 2000plus selector guide.*

[94] R.K. Gupta. *Polymer and composite rheology.* Marcel Dekker Inc., 2000.

[95] G Schramm. Introduzione alla viscosimetria pratica. *Gebruder Haake GmbH, Karlsruhe*, page 10, 1981.

[96] A.G. Fredrickson. Principles and applications of rheology. 1964.

[97] G. Stachowiak and A.W. Batchelor. *Engineering tribology.* Butterworth-Heinemann, 2011.

[98] W. Weibull. A statistical distribution function of wide applicability. *Journal of applied mechanics*, 18(3):293–297, 1951.

Appendix A

Wheel general design and terminology [3]

Appendix B

Data sheets of the adhesive employed in the experimental work of this thesis.

LOCTITE®

Research, Development & Engineering

Tallaght Business Park,
Dublin, Ireland

Technical Data Sheet
Hysol® 9492

July 2003

PRODUCT DESCRIPTION

Loctite Hysol 9492 is a high temperature resistant, two component epoxy adhesive. It is a lower viscosity version of Hysol 9491 and retains the high performance features of this product:

- Very low outgassing
- High temperature resistance
- Excellent solvent resistance

TYPICAL APPLICATIONS

Hysol 9492 is a general purpose adhesive that bonds and repairs a wide variety of materials. Fully cured Hysol 9492 bonds offer superior thermal shock resistance, mechanical, electrical and impact resistant properties.

PROPERTIES OF UNCURED MATERIAL

Resin	Typical Value
Chemical Type	Epoxy
Appearance	White opaque paste
Specific Gravity @25°C	1.51
Brookfield RVT viscosity @25°C Spindle 6 @5rpm, mPas	50,000 to 120,000
Viscosity, DIN 54453, mPas D= 10s⁻¹ D= 100s⁻¹	45,000 34,000
Flash Point (TCC), °C (°F)	>93 (>200)

Hardener	Typical Value
Chemical Type	Modified Amine
Appearance	Grey opaque liquid
Specific Gravity @25°C	1.52
Brookfield RVT viscosity @25°C Spindle 7 @50rpm, mPas	20,000 to 50,000
Viscosity, DIN 54453, mPas D= 10s⁻¹ D= 100s⁻¹	27,000 20,000
Flash Point (TCC), °C (°F)	>93 (>200)

Mixed Adhesive	Typical Value
Appearance	White opaque paste
Mix Ratio by Volume (Resin/Hardener)	2:1
Mix Ratio by Weight (Resin/Hardener)	100:50
Maximum gap fill (mm)	1
Working Life of mixed adhesive @22°C (100g mix), minutes	15
Fixture Time (light handling, (0.1N/mm²) @22°C, minutes	75

TYPICAL CURING PERFORMANCE
Cure Speed vs. time/temperature

Hysol 9492 develops complete cure within three days at room temperature. After 24 hours, approximately 90% of full cure properties are attained. Hysol 9492 will achieve light handling strength in 75 minutes at 22°C (Note: this can vary with different bond configurations). The following graph indicates development of shear strength on grit-blasted steel lapshears with 0.05mm gap as a function of time and temperature, tested according to ASTM D-1002/EN 1465. Note: Bond heat up time must be added to this cure time.
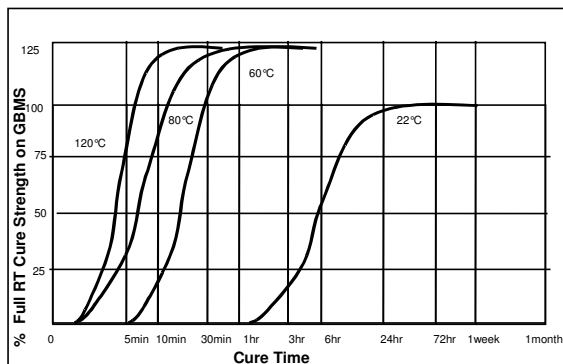
TYPICAL PROPERTIES OF CURED MATERIAL
(1.2mm thick samples cured for 7days@22°C)

Physical Properties	Typical Value
Tensile Strength, ASTM D882, N/mm²	31.0
Young's Modulus, ASTM D882, N/mm²	6700
Elongation, ASTM D-882, %	0.8
Hardness, ASTM D1706, Shore D	80
Coefficient of Thermal Expansion, ASTM D 696 (-40° - 80°), m/m/ K	63 x 10⁻⁶
Coefficient of Thermal Conductivity, W/m/K ASTM C177-63	0.3
Compressive Strength, ASTM D695, N/mm²	80

Electrical Properties	Typical Value
Dielectric Strength, ASTM D149, KV/mm	17.5
Dielectric Constant, MIL 1-16923. K 1kHz	6.1
Dissipation Factor, ASTM D 150 1kHz	0.09

PERFORMANCE OF CURED MATERIAL
(Cured for 7 days @22°C, unless otherwise stated)

Shear Strength, ASTM D1002/EN 1465 (0.05mm gap unless otherwise stated), N/mm²	Typical Value (N/mm²)
Steel, Grit Blasted Mild Steel (GBMS)	20
Aluminium, Abraded (Silicon Carbide Paper, A166 grit, P400A grade)	14
Aluminium, Etched in Acidic Ferric Sulphate	15
Stainless Steel	12
Brass	1
Hot Dipped Galvanised Steel	2.2
Zinc Dichromate	6
Polycarbonate	5.3
ABS	3
GRP (Polyester Resin Matrix)	5
PVC	1.9
Epoxy (Glass Fibre Reinforced Epoxy)	7

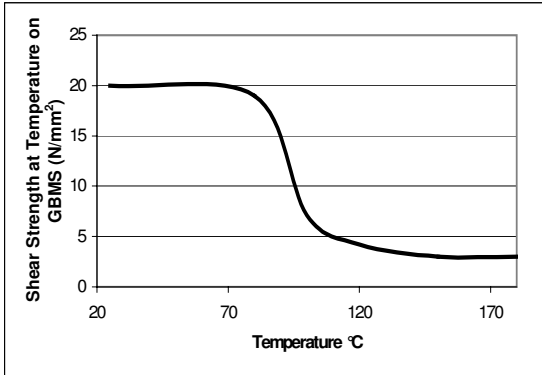| IZOD Impact Resistance, ISO 9653/ASTM D950-98, Steel, GBMS, J/m²	3.7

180° Rigid Peel Strength, ASTM D1876 Steel, GBMS, N/mm	1.6

TYPICAL ENVIRONMENTAL RESISTANCE

Test procedure :	ASTM D1002/EN 1465
Substrate:	Grit Blasted Mild Steel (GMBS)
Bondline gap:	0.05 mm
Cure procedure:	7 days @22°C

Hot Strength
Tested at temperature.

Temperature Storage.
Cured for 5 days @22°C. Stored in air at temperature indicated and tested @22°C.

Temperature	% Initial Strength retained after			
	100hr	500hr	1000hr	3000hr
100ºC	125	140	140	130
125ºC	140	135	130	135
150ºC	120	120	120	110
180ºC	130	90	65	30

Chemical/Solvent Resistance
Cured for 5 days @22°C. Immersed in conditions indicated and tested @22ºC.

Solvent	Temp.	% Initial Strength retained after		
		500hr	1000hr	3000hr
Motor Oil	22°C	115	115	115
Unleaded Petrol	22°C	115	115	115
50% Water Glycol	87°C	130	110	105
4% NaOH/water	22°C	125	110	115
98% Relative Humidity	40°C	105	105	105
Water	60°C	130	120	120
Water	90°C	95	85	85
Acetone	22°C	80	70	65
10% Acetic Acid	22°C	105	95	95
7.5% Salt water solution	22°C	105	100	100

GENERAL INFORMATION
This product is not recommended for use in pure oxygen and/or oxygen rich systems and should not be selected as a sealant for chlorine or other strong oxidising materials.

For safe handling information on this product, consult the Material Safety Data Sheet, (MSDS).

Directions for Use
1. For best performance surfaces for bonding should be clean, dry and free of grease. For high strength structural bonds, special surface treatments can increase the bond strength and durability .
2. To use, resin and hardener must be blended. Product can be applied directly from dual cartridges by dispensing through the mixer head supplied. Discard the first 3-5cm of bead dispensed. Using bulk containers, mix thoroughly by weight or volume in the proportions specified in Properties of Uncured Material section. For hand mixing, weigh or measure out the desired amount of resin and hardener and mix thoroughly. Mix approximately 15 seconds after uniform colour is obtained.
3. Do not mix quantities greater than 0.5kg as excessive heat build-up can occur. Mixing smaller quantities will minimise the heat build-up.
4. Apply the adhesive as quickly as possible after mixing to one surface to be joined. For maximum bond strength apply adhesive evenly to both surfaces. Parts should be assembled immediately after mixed adhesive has been applied.
5. Working Life of the mixed adhesive is 15 minutes at 22°C. Higher temperature and larger quantities will shorten this working time.
6. Excess uncured adhesive can be wiped away with organic solvent (e.g. acetone).
7. Keep the assembled parts from moving during cure. The joint should be allowed to develop full strength before subjecting to any service loads.
8. After use and before adhesive hardens mixing and application equipment should be cleaned with hot soapy water.

Storage
Product shall be ideally stored in a cool, dry location in unopened containers at a temperature between 8°C to 21°C (46°F to 70°F) unless otherwise labelled. Optimal storage is at the lower half of this temperature range. To prevent contamination of unused product, do not return any material to its original container. For further specific shelf life information, contact your local Technical Service Centre.

Data Ranges
The data contained herein may be reported as a typical value and/or range. Values are based on actual test data and are verified on a periodic basis.

Note
The data contained herein are furnished for information only and are believed to be reliable. We cannot assume responsibility for the results obtained by others over whose methods we have no control. It is the user's responsibility to determine suitability for the user's purpose of any production methods mentioned herein and to adopt such precautions as may be advisable for the protection of property and of persons against any hazards that may be involved in the handling and use thereof. In light of the foregoing, **Loctite Corporation specifically disclaims all warranties expressed or implied, including warranties of merchantability or fitness for a particular purpose, arising from sale or use of Loctite Corporation's products. Loctite Corporation specifically disclaims any liability for consequential or incidental damages of any kind, including lost profits.** The discussion herein of various processes or compositions is not to be interpreted as representation that they are free from domination of patents owned by others or as a license under any Loctite Corporation patents that may cover such processes or compositions. We recommend that each prospective user test his proposed application before repetitive use, using this data as a guide. This product may be covered by one or more United States or foreign patents or patent applications.

Bulk Numbers: **Part A: 210032**
                                Part B: 210033

3M

Scotch-Weld™

EPX™ Adhesive DP490

Product Data Sheet

Product Description	DP490 is a black, thixotropic, gap filling two component epoxy adhesive with particularly good application characteristics.	It is designed for use where toughness and high strength are required and shows special benefits in the construction of composite assemblies.	The product has excellent heat and environmental resistance.

Physical Properties
Not for specification purposes

	BASE	ACCELERATOR
Specific Gravity	1.00	1.00
Consistency	Non-sag paste	Non-sag paste
Mix Ratio By Weight By Volume	100 100	50 50
Colour	Black	Off-White
Work Life	1.5 hours minimum at 23°C	
Time to Handling Strength	4 to 6 hours at 23°C	
Time to Full Strength	7 days (test to full performance at one week)	
Shelf Life	15 months from date of despatch by 3M when stored in the original carton at 21°C (70°F) & 50 % Relative Humidity	

Performance Characteristics
Not for specification purposes

Performance Characteristics of the Cured Adhesive.

Two cure cycles were evaluated as follows:

Cure Cycle 1	7 days at 23°C
Cure Cycle 2	24 hours at 23°C, 1 hour at 80°C

| **Performance Characteristics (Cont...)** | **Temperature Performance in Shear and Peel.** | (Etched Aluminium) Shear Strength to BS 5350 C5, Peel Strength was floating roller peel to BS5350 C9. | Tests were performed at 23°C unless otherwise stated. |

Not for specification purposes

Temperature (°C)	Shear Strength (1) (N/mm²)	Shear Strength (2) (N/mm²)	Peel Strength DaN/cm
-55	23.7	31.6	N/A
23	30.2	28.7	9.24
80	11.9	12.7	7.32
120	2.8	3.2	N/A
150	1.9	1.7	N/A

Adhesion to Etched Aluminium after Environmental Ageing

Ageing Condition	Shear Strength (N/mm²)
RT Control	26.2
Water at 23°C, 750 hours	25.6
50°C, 96% RH, 750 hours	22.0
120°C, 750 hours	25.3
175°C, dry heat, 120 hours	29.6
Skydroll 500B at 23°C, 750 hours	27.6
JP4 at 23°C, 750 hours	28.7
Hydraulic Oil at 23°C, 750 hours	29.5

DP490 shows good adhesion to many plastic surfaces even by simply solvent wiping.

This can be improved still further by the use of 3M Scotchbrite abrasion and/or use of the primer Scotch-Weld 3901.

Plastics	Shear Strength (N/mm²)
Carbon Fibre Reinforced Epoxy	36.1 (cohesive)
Polyester Sheet Moulding Compound	4.3 (substrate)
Glass Fibre Reinforced Phenolic	30.3 (cohesive)
ABS (filled)	3.2 (substrate)
PVC (filled)	2.9 (substrate)
Azloy (glass filled polycarbonate)	3.0 (adhesion)
Valox (glass filled PET)	1.4 (substrate)
PMMA	3.7 (adhesion)
Noryl (tm XTRA) (glass filled PPO)	4.9 (adhesion)

| **Storage Conditions** | Store product at 15°C to 25°C for maximum storage life. |

Directions for Use /Clean Up

Place the cartridge into the 3M EPX Applicator and clip into position.

Remove the resealable cap.

Expel a small quantity of adhesive and ensure both components flow freely.

Attach correct mixer nozzle (this should have 20 or more elements).

Dispense the adhesive as required.

When finished either leave the nozzle in place and store, or remove the nozzle, wipe clean the tip, and replace cap.

To re-start after storage remove the old nozzle with cured adhesive and re-fit a new nozzle, or remove the cap and fit a new nozzle.

Surface Preparation:
The degree of surface preparation depends on the bond strength required and the environment likely to be encountered by the bonded structure. For most plastics solvent wiping with 3M VHB surface cleaner, followed by abrasion with 3M Scotchbrite 7447, followed by a further solvent wipe until clean, will give good performance (except for acetal, polyethylene and polypropylene and some other low surface energy materials). This also applies to powder coat paints and other stoved paint systems.

The same surface preparation will also give good adhesion to metal surfaces. The objective is to remove loosely attached surface films such as oils, waxes, dusts, mill-scale, loose paints and all other surface contaminants in addition to enhancing mechanical adhesion. Grit-blasting using a clean, fine grit also offers excellent adhesion on many metallic substrates.

Where humid environments are likely to be encountered by metallic substrates we recommend additional priming with 3M Scotch-Weld 3901. Alternatively, chemical conversion coating techniques combined with priming can offer the best durability.

Clean-Up:
Excess uncured adhesive can be removed with the following solvents:

3M VHB Surface Cleaner (mild alcohol based cleaner)
3M Scotch-Grip Solvent No2. (Ketone blend)
3M Industrial Cleaner (Aerosol).

Additional Product Information

Please contact your 3M Salesperson for additional information on the preparation of difficult surfaces, or likely exposure to aggressive environments.

Health & Safety Information

Precautions:
Causes severe eye irritation, may cause permanent eye damage. Irritating to skin. May cause sensitisation by skin contact. Avoid contact with the skin and eyes. Wear suitable gloves and eye/face protection.

Launder contaminated clothing before re-use. Avoid prolonged breathing of vapours. Avoid inhalation of dust when grinding or cutting cured material.

First Aid:

Eye Contact: Immediately flush eyes with copious amounts of water for at least 15 minutes, holding eyes open. Call a physician.

Skin Contact: Wash immediately with plenty of soap and water.

For further information please contact the Toxicology Department at the Bracknell Head Office on (0344) 858000.

3M, EPX, Duo-Pak, Scotch-Grip, Scotchbrite and Scotch-Weld are trademarks of the 3M Company.

3M

Specialty Tapes & Adhesives

LOCTITE® 620

PRODUCT DESCRIPTION

LOCTITE® 620 provides the following product characteristics:

Technology	Acrylic
Chemical Type	Methacrylate ester
Appearance (uncured)	Green liquid[LMS]
Components	One component - requires no mixing
Viscosity	High
Cure	Anaerobic
Secondary Cure	Activator
Application	Retaining
Strength	Medium to High

LOCTITE® 620 is designed for the bonding of cylindrical fitting parts. The product cures when confined in the absence of air between close fitting metal surfaces and prevents loosening and leakage from shock and vibration. Typical applications include locating pins in radiator assemblies, sleeves into pump housings and bearings in auto transmissions. Particularly suitable for applications where temperature resistance up to 200°C is required.

TYPICAL PROPERTIES OF UNCURED MATERIAL

Specific Gravity @ 25 °C   1.16
Flash Point - See MSDS
Viscosity, Brookfield - RVT, 25 °C, mPa·s (cP):
  Spindle 5, speed 20 rpm   5,000 to 12,000[LMS]
Viscosity, EN 12092 - MV, 25 °C, after 180 s, mPa·s (cP):
  Shear rate 129 s^{-1} 1,200 to 2,400

TYPICAL CURING PERFORMANCE

Cure Speed vs. Substrate

The rate of cure will depend on the substrate used. The graph below shows the shear strength developed with time on steel pins and collars compared to different materials and tested according to ISO 10123.
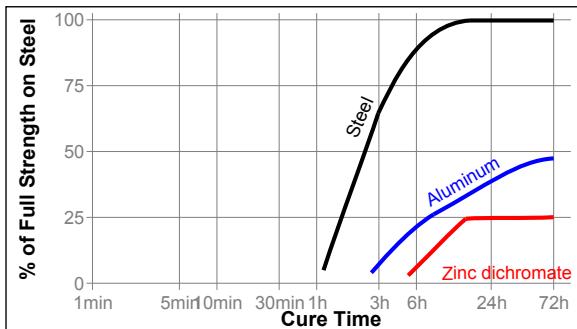
Cure Speed vs. Bond Gap

The rate of cure will depend on the bondline gap. The following graph shows shear strength developed with time on steel pins and collars at different controlled gaps and tested according to ISO 10123.
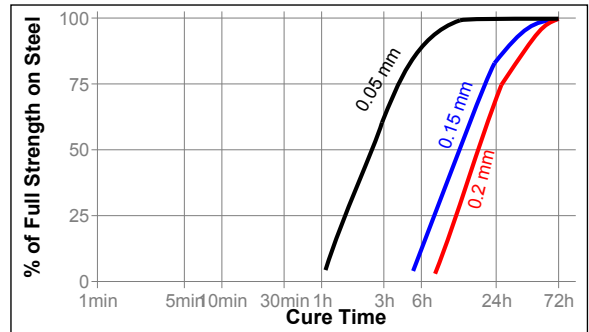
Cure Speed vs. Temperature

The rate of cure will depend on the temperature. The graph below shows the shear strength developed with time at different temperatures on steel pins and collars and tested according to ISO 10123.
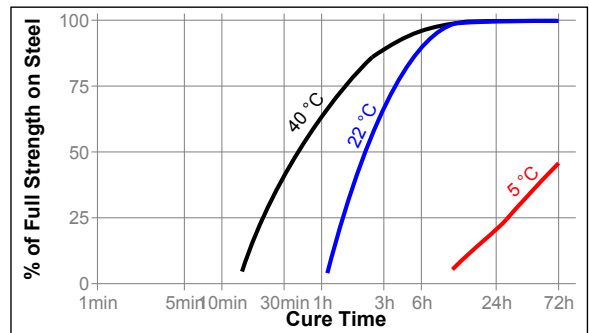
Cure Speed vs. Activator

Where cure speed is unacceptably long, or large gaps are present, applying activator to the surface will improve cure speed. The graph below shows the shear strength developed with time on zinc dichromate steel pins and collars using Activator 7471™ and 7649™ and tested according to ISO 10123.

Henkel
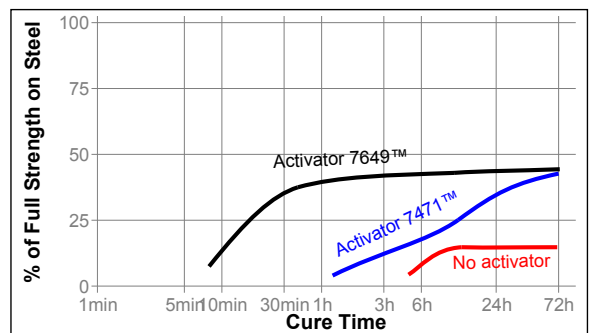
TYPICAL PROPERTIES OF CURED MATERIAL
Physical Properties:

Coefficient of Thermal Expansion, ISO 11359-2, K^{-1}	80×10^{-6}
Coefficient of Thermal Conductivity, ISO 8302, W/(m·K)	0.1
Specific Heat, kJ/(kg·K)	0.3
Elongation, at break, ISO 37, %	<1

TYPICAL PERFORMANCE OF CURED MATERIAL
Adhesive Properties

After 24 hours @ 22 °C
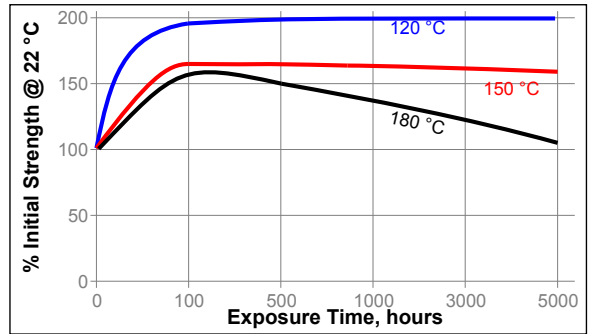 Compressive Shear Strength, ISO 10123:

Steel pins and collars	N/mm²	≥17.2[LMS]
	(psi)	(2,495)

Cured for 24 hours @ 22 °C, followed by 24 hours @ 177 °C, tested @ 22 °C
  Compressive Shear Strength, ISO 10123:

Steel pins and collars	N/mm²	≥24.1[LMS]
	(psi)	(3,495)

TYPICAL ENVIRONMENTAL RESISTANCE
Cured for 1 week @ 22 °C
  Compressive Shear Strength, ISO 10123:
    Steel pins and collars

Hot Strength
Tested at temperature

Heat Aging
Aged at temperature indicated and tested @ 22 °C

Heat Aging
Aged at temperature indicated and tested @ 22 °C

Chemical/Solvent Resistance
Aged under conditions indicated and tested @ 22 °C.

Environment	°C	% of initial strength		
		100 h	500 h	1000 h
Motor oil (MIL-L-46152)	125	100	100	100
Unleaded Petrol	22	95	95	95
Brake fluid	22	100	100	100
Water/glycol 50/50	87	95	80	80
Ethanol	22	100	100	75
Acetone	22	95	95	95

GENERAL INFORMATION
This product is not recommended for use in pure oxygen and/or oxygen rich systems and should not be selected as a sealant for chlorine or other strong oxidizing materials.

For safe handling information on this product, consult the Material Safety Data Sheet (MSDS).

Where aqueous washing systems are used to clean the surfaces before bonding, it is important to check for compatibility of the washing solution with the adhesive. In some cases these aqueous washes can affect the cure and performance of the adhesive.

This product is not normally recommended for use on plastics (particularly thermoplastic materials where stress cracking of the plastic could result). Users are recommended to confirm compatibility of the product with such substrates.
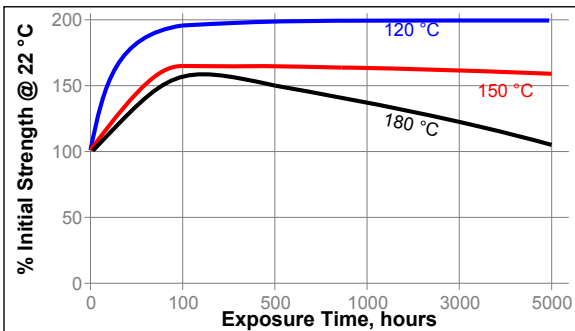
Directions for use:
For Assembly
1. For best results, clean all surfaces (external and internal) with a LOCTITE® cleaning solvent and allow to dry.
2. If the material is an inactive metal or the cure speed is too slow, spray with Activator 7471™ or 7649™ and allow to dry.
3. Shake the product thoroughly before use.
4. **For Slip Fitted Assemblies**, apply adhesive around the leading edge of the pin and the inside of the collar and use a rotating motion during assembly to ensure good coverage.
5. **For Press Fitted Assemblies**, apply adhesive thoroughly to both bond surfaces and assemble at high press on rates.
6. **For Shrink Fitted Assemblies** the adhesive should be coated onto the pin, the collar should then be heated to

Henkel Americas
+860.571.5100

Henkel Europe
+49.89.320800.1800

Henkel Asia Pacific
+86.21.2891.8863

For the most direct access to local sales and technical support visit: www.henkel.com/industrial

create sufficient clearance for free assembly.

7. Parts should not be disturbed until sufficient handling strength is achieved.

For Disassembly

1. Apply localized heat to the assembly to approximately 250 °C. Disassemble while hot.

For Cleanup

1. Cured product can be removed by soaking in a Loctite® solvent, e.g. Loctite® 7200 and mechanical removal with a soft scraper. Complete the cleaning process by wiping with a soft cloth dampened with Loctite® Cleaner, e.g. Loctite® 7063 or Loctite® ODC-free cleaner.

Loctite Material Specification^LMS

LMS dated August 20, 1997. Test reports for each batch are available for the indicated properties. LMS test reports include selected QC test parameters considered appropriate to specifications for customer use. Additionally, comprehensive controls are in place to assure product quality and consistency. Special customer specification requirements may be coordinated through Henkel Quality.

Storage

Store product in the unopened container in a dry location. Storage information may be indicated on the product container labeling.
Optimal Storage: 8 °C to 21 °C. Storage below 8 °C or greater than 28 °C can adversely affect product properties. Material removed from containers may be contaminated during use. Do not return product to the original container. Henkel Corporation cannot assume responsibility for product which has been contaminated or stored under conditions other than those previously indicated. If additional information is required, please contact your local Technical Service Center or Customer Service Representative.

Conversions

(°C x 1.8) + 32 = °F
kV/mm x 25.4 = V/mil
mm / 25.4 = inches
µm / 25.4 = mil
N x 0.225 = lb
N/mm x 5.71 = lb/in
N/mm² x 145 = psi
MPa x 145 = psi
N·m x 8.851 = lb·in
N·m x 0.738 = lb·ft
N·mm x 0.142 = oz·in
mPa·s = cP

Note

The data contained herein are furnished for information only and are believed to be reliable. We cannot assume responsibility for the results obtained by others over whose methods we have no control. It is the user's responsibility to determine suitability for the user's purpose of any production methods mentioned herein and to adopt such precautions as may be advisable for the protection of property and of persons against any hazards that may be involved in the handling and use thereof. In light of the foregoing, **Henkel Corporation specifically disclaims all warranties expressed or implied, including warranties of merchantability or fitness for a particular purpose, arising from sale or use of Henkel Corporation's products. Henkel Corporation specifically disclaims any liability for consequential or incidental damages of any kind, including lost profits.** The discussion herein of various processes or compositions is not to be interpreted as representation that they are free from domination of patents owned by others or as a license under any Henkel Corporation patents that may cover such processes or compositions. We recommend that each prospective user test his proposed application before repetitive use, using this data as a guide. This product may be covered by one or more United States or foreign patents or patent applications.

Trademark usage

Except as otherwise noted, all trademarks in this document are trademarks of Henkel Corporation in the U.S. and elsewhere. ® denotes a trademark registered in the U.S. Patent and Trademark Office.

Reference 0.4

Henkel Americas
+860.571.5100

Henkel Europe
+49.89.320800.1800

Henkel Asia Pacific
+86.21.2891.8863

For the most direct access to local sales and technical support visit: www.henkel.com/industrial

HUNTSMAN

Enriching lives through innovation

Advanced Materials

Araldite® 2029

Structural Adhesives

Araldite® 2029
Two component gap filling polyurethane adhesive

Key properties	
	• **Gap filling**
	• **Medium open time**
	• **High strength on metal**
	• **Adhesion to copper and brass**

Description

Araldite 2029 is a cold curing polyurethane adhesive, consisting of a grey resin component and a beige-coloured hardener component. High strength on metal. Rigid adhesive for structural application.

Product data

Property	Component A (resin)	Component B (hardener)	Mixed Adhesive
Colour (visual)	Grey	Beige	Grey paste
Specific gravity	1.44	1.19	1.32
Viscosity at 25°C (Pas)	60	60	-
Pot Life (100 gm at 25°C)	-	-	40 minutes

Processing

Pretreatment

The strength and durability of a bonded joint are dependent on proper treatment of the surfaces to be bonded.

At the very least, joint surfaces should be cleaned with a good degreasing agent such as acetone, iso-propanol (for plastics) or other proprietary degreasing agents in order to remove all traces of oil, grease and dirt.

Low grade alcohol, gasoline (petrol) or paint thinners should never be used.

The strongest and most durable joints are obtained by either mechanically abrading or chemically etching ("pickling") the degreased surfaces. Abrading should be followed by a second degreasing treatment

Mix ratio	Parts by weight	Parts by volume
Component A (resin)	100	100
Component B (hardener)	82	100

Application of adhesive

The resin/hardener mix may be applied manually or robotically to the pretreated and dry joint surfaces. Huntsman's technical support group can assist the user in the selection of an suitable application method as well as suggest a variety of reputable companies that manufacture and service adhesive dispensing equipment.

A layer of adhesive 0.05 to 0.10 mm thick will normally impart the greatest lap shear strength to the joint. Huntsman stresses that proper adhesive joint design is also critical for a durable bond. The joint components should be assembled and secured in a fixed position as soon as the adhesive has been applied.

For more detailed explanations regarding surface preparation and pretreatment, adhesive joint design, and the dual syringe dispensing system, visit www.araldite2000plus.com.

Equipment maintenance

All tools should be cleaned with hot water and soap before adhesives residues have had time to cure. The removal of cured residues is a difficult and time-consuming operation.

If solvents such as acetone are used for cleaning, operatives should take the appropriate precautions and, in addition, avoid skin and eye contact.

Times to minimum shear strength (laboratory conditions: 40-60% RH)

Temperature	°C	10	15	23	40	60	100
Cure time to reach	hours	9	6	4			
LSS > 1MPa	minutes				70	25	< 5
Cure time to reach	hours	30	16	8	4	1	
LSS > 10MPa	minutes						10

LSS = Lap shear strength.

Typical cured properties

Unless otherwise stated, the figures given below were all determined by testing standard specimens made by lap-jointing 114 x 25 x 1.6 mm strips of aluminium alloy. The joint area was 12.5 x 25 mm in each case.

The figures were determined with typical production batches using standard testing methods. They are provided solely as technical information and do not constitute a product specification.

Note: The data in this edition is based on recent retesting of the product.

Average lap shear strengths of typical metal-to-metal joints (ISO 4587)

Cured for 16 hours at 40°C and tested at 23°C
Pretreatment - Sand blasting
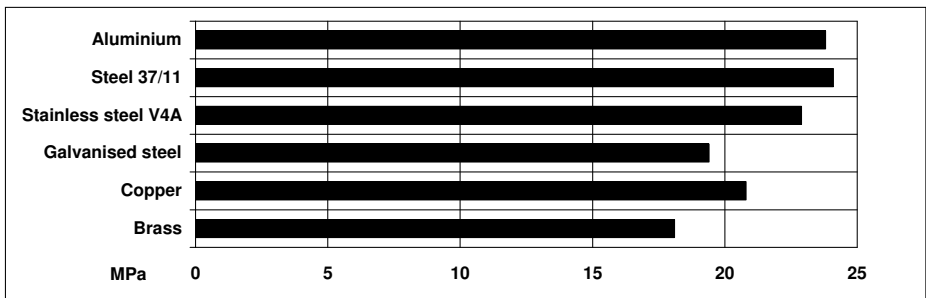
Average lap shear strengths of typical plastic-to-plastic joints (ISO 4587)

Cured for 16 hour at 40°C and tested at 23°C. Pretreatment - Lightly abrade and alcohol degrease.

Material	MPa (approximate)
CFRP	27
EP-GRP	24.5
UP-GRP	11
SMC	6
ABS	5.5
PA 6.6	4.5
PC	6
PMMA	4.5
PVC	5
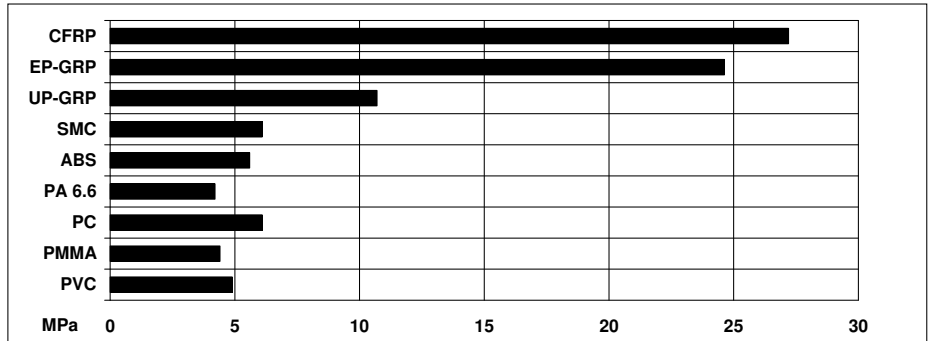
Lap shear strength versus temperature (ISO 4587) (typical average values)
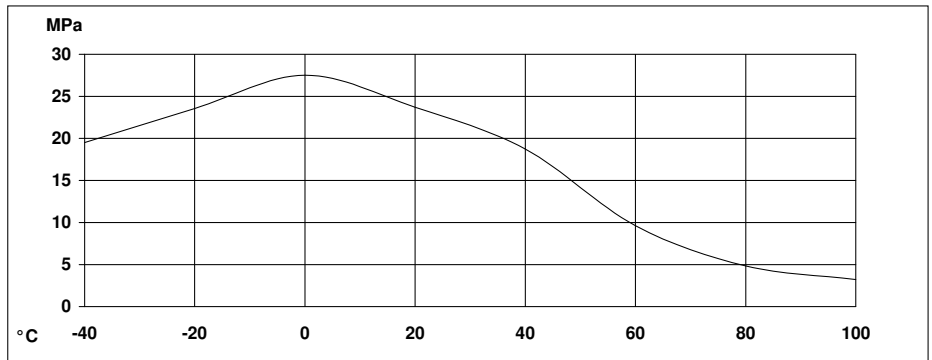
Cure: 16 hours at 40°C

Roller peel test (ISO 4578)

Cured: 16 hours at 40°C

3.1 N/mm

Glass transition temperature

Cure: 16 hours at 40°C

28°C by DSC

Lap shear strength versus immersion in various media (typical average values)

Unless otherwise stated, L.S.S. was determined after immersion for 30,60 and 90 days at 23°C

	□ 30 days	▨ 60 days	■ 90 days	Cure: 16 hours at 40°C

As-made value
IMS
Fuel (unleaded)
Ethyl acetate
Acetic acid, 10%
Xylene
Lubricating oil
Paraffin
Water at 23°C
Water at 60°C
Water at 90°C

MPa   0   5   10   15   20   25   30
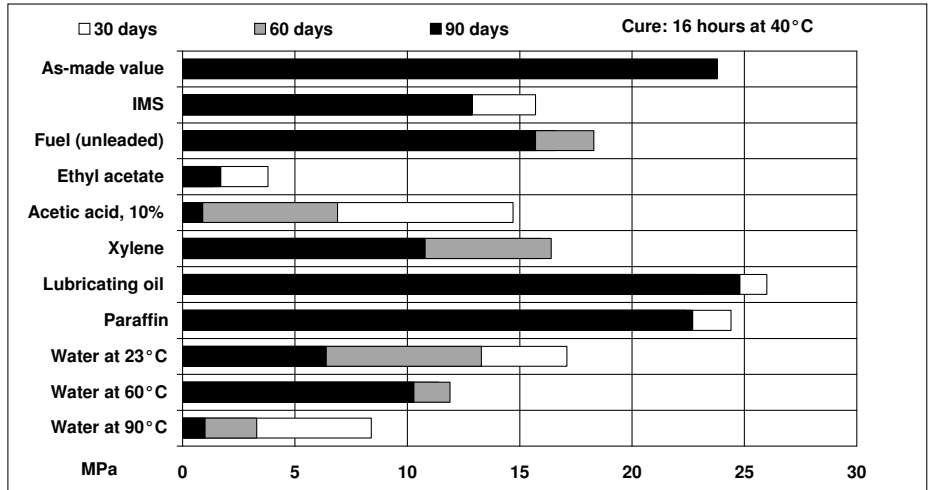
Lap shear strength versus tropical weathering

(40/92, DIN 50017; typical average values)
Cure: 16 hours at 40°C   Test: at 23°C

As made value
After 30 days
After 60 days
After 90 days

MPa   0   5   10   15   20   25
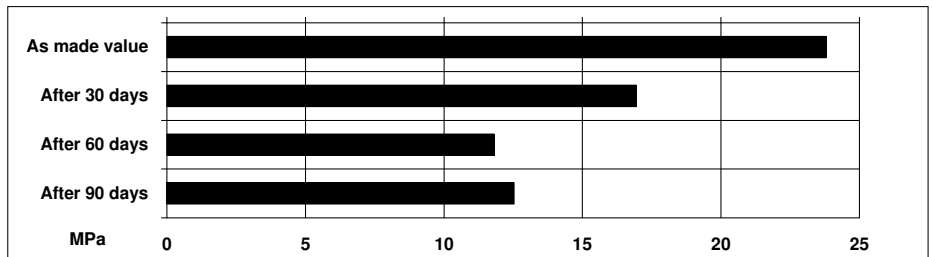
Lap shear strength versus heat ageing

Cure: 16 hours at 40°C

	MPa
As-made value	
30 days/ 70°C	
60 days/ 70°C	
90 days/ 70°C	

(Bar chart — horizontal bars, x-axis labeled MPa with values 0, 5, 10, 15, 20, 25, 30, 35)
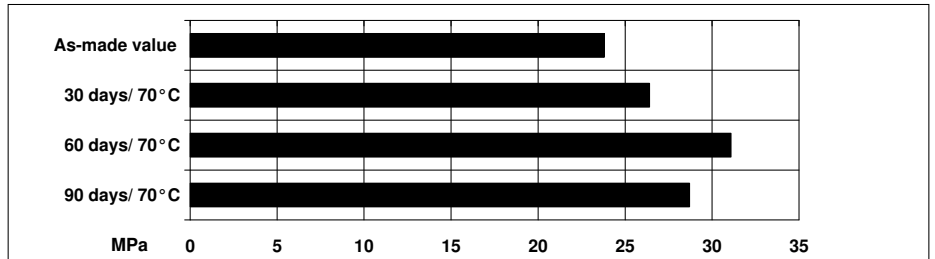
Thermal cycling

100 cycles of 6 hour duration from -30°C to 70°C: 27.8 MPa

Tensile strength at 23°C (ISO 527)   20 MPa
E- modulus   576 MPa
 Elongation at break   39 %

Storage

Araldite 2029 may be stored for up to 15 months at 15 – 25 ℃, provided the components are stored in sealed containers. The expiry date is indicated on the label.

Handling precautions

Caution

Our products are generally quite harmless to handle provided that certain precautions normally taken when handling chemicals are observed. The uncured materials must not, for instance, be allowed to come into contact with foodstuffs or food utensils, and measures should be taken to prevent the uncured materials from coming in contact with the skin, since people with particularly sensitive skin may be affected. The wearing of impervious rubber or plastic gloves will normally be necessary; likewise the use of eye protection. The skin should be thoroughly cleansed at the end of each working period by washing with soap and warm water. The use of solvents is to be avoided. Disposable paper - not cloth towels - should be used to dry the skin. Adequate ventilation of the working area is recommended. These precautions are described in greater detail in the Material Safety Data sheets for the individual products and should be referred to for fuller information.

Huntsman Advanced Materials

All recommendations for the use of our products, whether given by us in writing, verbally, or to be implied from the results of tests carried out by us, are based on the current state of our knowledge. Notwithstanding any such recommendations the Buyer shall remain responsible for satisfying himself that the products as supplied by us are suitable for his intended process or purpose. Since we cannot control the application, use or processing of the products, we cannot accept responsibility therefor. The Buyer shall ensure that the intended use of the products will not infringe any third party's intellectual property rights. We warrant that our products are free from defects in accordance with and subject to our general conditions of supply.